Title

Anisotropy and Disorder in Fractionalized Phases

Author

Aldape, Erik E

Publication Date

2023

Anisotropy and Disorder in Fractionalized Phases

by

Erik E Aldape

A dissertation submitted in partial satisfaction of the

requirements for the degree of

Doctor of Philosophy

in

Physics

in the

Graduate Division

of the

University of California, Berkeley

Committee in charge:

Professor Ehud Altman, Chair
Professor Michael Zaletel
Professor Lin Lin

Fall 2023

Anisotropy and Disorder in Fractionalized Phases

Abstract

Anisotropy and Disorder in Fractionalized Phases

by

Erik E Aldape

Doctor of Philosophy in Physics

University of California, Berkeley

Professor Ehud Altman, Chair

In this dissertation we will describe aspects of the interplay of anisotropy and disorder with fractionalized phases of matter through three studies.

The first study concerns a material, α-RuCl$_3$, which has been suggested to be proximate to a fractionalized phase called the Kitaev spin liquid. Despite the presence of traditional magnetic order at low temperatures, ab-initio predictions, and an observed continuum of magnetic excitations at high energies has led to excitement that the material is close to the spin liquid phase. In this study, we describe the magnetic excitations of α-RuCl$_3$ as observed by time-domain terahertz spectroscopy. In the presence of a small (1.5T) magnetic field, a discontinuity in the spectra of magnetic excitations as well as a continuum of magnetic absorption is observed. These observations are suggestive of a field induced transition or proximity to the Kitaev spin liquid. However, with the assumption of random bond anisotropy, we show that a conventional magnetic order is sufficient to explain all observed features. While we find that the experiment can be qualitatively fit to a Hamiltonian with large Kitaev coupling, all aspects of the experiment are shown to be well described by non-fractionalized excitations.

In the second study we consider the impact of lattice vacancies in the Kitaev spin liquid, which represents an expected form of disorder in any physical realization of the phase. In Kitaev's exactly solvable honeycomb model, it has been shown that introducing a lattice vacancy binds an emergent Z_2 flux. This offers a feasible route to creating and trapping this fractionalized excitation. However, it is unclear if this would hold generally for Kitaev spin liquids or only for Kitaev's integrable model. To address this, we introduce a universal low-energy effective theory for the spin liquid with vacancies and Z_2 fluxes. Using this low-energy theory in the gapless phase we find that the binding energy can be attributed to the suppression of a scattering resonance caused by the vacancy. In the non-abelian phase, where Z_2 fluxes are Ising anyons, we find that the binding energy has a topological origin. Identifying the doubled spin liquid as a quantum Hall state allows us to argue that spectral flow as flux is threaded through the vacancy induces the binding energy. Our results show that lattice vacancies offer a robust method of creating and trapping Ising anyons in realistic instances of the Kitaev spin liquid. Additionally, this finding indicates that in the presence of vacancy disorder, the Kitaev spin liquid should be expected to have a ground state with Z_2 fluxes pinned to the vacancies.

In the final chapter we introduce exactly solvable models of the phase transition between a Fermi Liquid and a fractionalized Fermi Liquid (FL*) defined by the emergence of a $U(1)$ gauge field. We compare the cases where the interactions of this model are spatially disordered or translationally invariant. Unlike previous attempts to analytically describe this phase transition, the approach that we introduce allows for the description of strongly coupled fixed points. In particular, we find that it can describe the ubiquitous linear in temperature strange metal resistivity observed near many metallic critical points. For spatially disordered couplings this strange metal phenomenology only appears if the spin liquid deconfines anisotropically into two-dimensional planes of the three-dimensional material. In the limit of strong damping of the critical boson, the model describes a Planckian strange metal in which quasiparticle lifetimes are set only by fundamental constants and the temperature.

To Mariela,
whose love gifts reason and strength to do things that are challenging.

Contents

List of Figures

Acknowledgments

This dissertation is only made possible by the tremendous amount of support that I have received over the years.

This research started on an end-of-semester afternoon in Ehud Altman's office. Ehud spent the afternoon showing me the solution to the Kitaev Honeycomb model and then next convincing me that fractionalization had occurred. By the end of the discussion, I was sold on the idea and understanding the physics of fractionalization became my goal. In this chat, and as an advisor, he was patient, and made complex concepts simple. His physical intuition was a useful guide as I navigated new territories. I am indebted to him for showing me how to think, communicate and write like a physicist.

I am also indebted to members of our research group who have provided academic support and friendship. I would like to thank Yimu Bao, Sam Garratt, Jaewon Kim, Aavishkar Patel, Thomas Scaffidi and Zach Weinstein. Many of whom have kindly reviewed this text. In particular, Aavishkar Patel provided much guidance as we developed the work that is described in Chapter Four of this text. We found ways to work around the pandemic and create something I am proud of.

My first experience of physics research was with Uroš Seljak and Florian Beutler at Lawrence Berkeley National Laboratories, and I am grateful for the opportunity. I credit this experience with my decision to attend graduate school for physics.

I send my thanks to the Berkeley Physics student services team who keep the department running smoothly. From Claudia Trujillo who helped me chart out how to switch from psychology to physics as an undergraduate, to Anne Takizawa welcoming me to the physics department as a graduate student and Joelle Miles who advocated for me throughout the later stage of my graduate studies.

I would like to thank Charles Wohl and Ammar Hussain for teaching me how to be a quantum mechanic [170].

At my core, I am grateful to my family. To my parents Carol and Jess Aldape whose love and support know no bounds. Their sacrifices have allowed me to pursue my dreams. I was fortunate to attend university in driving distance of their home, where visits with them and my brother Samuel Aldape provided a restorative and centering constant in my life.

Fundamentally, I am filled with gratitude for my wife Mariela Aldape, for taking this journey with me. No challenge I take on now I do alone. Every step I took towards finishing this work was aided by her constant love and encouragement. This work was written hand in hand with her.

Co-Authored Materials

The following co-authored works of the author will appear in this dissertation:

Chapter Two: **L. Wu**, **A. Little**, **E. E. Aldape**, D. Rees, E. Thewalt, P. Lampen-Kelley, A. Banerjee, C. A. Bridges, J.-Q. Yan, D. Boone, S. Patankar, D. Goldhaber-Gordon, D. Mandrus, S. E. Nagler, E. Altman, and J. Orenstein "Field evolution of magnons in $\alpha-$RuCl$_3$ by high-resolution polarized terahertz spectroscopy". In: Physical Review B 98.9 (2018), p. 094425[172]

Chapter Three: **E. E. Aldape**, **E. Altman** "A Universal Mechanism for the Binding of Ising Anyons to Lattice Vacancies in a Non-Abelian Spin Liquid". In Preparation.

Chapter Four: **E. E. Aldape**, **T. Cookmeyer**, A. Patel and E. Altman "Solvable theory of a strange metal at the breakdown of a heavy Fermi liquid". In: Phys. Rev. B 105 (23 June 2022), p. 235111 [4]

Chapter 1

Introduction

Of the bizarre quantum phenomena that have been discovered in the last century, fractionalization may be the strangest and most beautiful. In a striking realization of Anderson's vision that "more is different" [6], when many degrees of freedom are assembled, the quantum numbers of their collective excitations may be fractions of the originals. For instance, in the fractional quantum Hall effect, quasiparticles have been observed that carry one-third of the electron's charge [154, 84, 120]. A further surprise is that these fractionalized excitations can have different exchange statistics than the elementary degrees of freedom from which they are formed [12, 162, 105, 145]. Indeed, they need not even be bosons or fermions! In many cases fractionalization can be described in terms of deconfinement of an emergent gauge field and therefore defines robust phases of matter we will call fractionalized phases [52, 138, 78, 16, 48]. Fractionalized phases of matter offer an opportunity to study effective field theories with entirely different forces and particle content from those provided by nature at the microscopic level.

An inescapable feature in many materials in which fractionalized phases may arise is the presence of random impurities. Therefore, to understand the properties of fractionalized phases in real materials it is important to understand how disorder impacts this physics. For example, theoretical study of the response of a polyacetylene molecule to a doped static charge lead to the discovery of spin-charge separation in this system [142, 141, 147, 66]. In this dissertation we will explore the impact of the natural imperfections disorder and anisotropy in several fractionalized phases of matter.

The rest of this chapter is dedicated to reviewing the fractionalized phases considered in this dissertation. We will first give a brief general introduction to spin liquids, which are fractionalized phases of quantum magnets. Then we provide a review of a class of exactly solvable models known as Kitaev spin liquids, considered in chapters two and three of the thesis. Spin liquids will be reviewed in general briefly before a detailed review of the Kitaev spin liquid will be given [78]. The Kitaev spin liquid will be the focus of chapters two and three. Next, we will give some background on the physics of heavy fermion systems. We review the standard theory for emergence of the large mass in a Kondo lattice model and the possible transition to a fractionalized metallic phase with a light mass. This transition between a Fermi liquid and a fractionalized Fermi liquid (FL*) will be the focus of Chapter Four.

1.1 Spin Liquids Review

Many familiar spin models, like the two-dimensional Ising model, find a classical magnetic order at sufficiently low temperatures. That is, the ground state is well-approximated by a product state with each spin direction fixed. Excitations of these systems are simply flips of the spins relative to this classical order. These excitations are not fractionalized because the spin flip operators are the elementary degrees of freedom of the system. On the other hand, the nature of the excitations of a magnetic system without a classical magnetic order in its ground state are much less obvious. We can think of such a system as being “melted” (not a technical term) with quantum fluctuations. Entanglement is a necessary ingredient here as if the system could be written as a product state, the spins’ directions would be well-defined. We will show several examples where this leads to excitations that are fractionalized. We will define a spin liquid by when a magnetic systems effective theory can be described as a deconfined phase of an emergent gauge field.

To understand why the ground state of a magnetic system might not find a classical order, an illustrative example of quantum effects is provided by a simple model of two spin-1/2 moments. If the Hamiltonian of the system is simply a magnetic field along the z-axis, $H = -h(S_1^z + S_2^z)$, the two will align with the field and the wavefunction is described by $\psi = |+z\rangle|+z\rangle$. This state is classical as each spin has a well-defined direction. Compare this to the case where the Hamiltonian is instead the Heisenberg interaction $H = JS_1 \cdot S_2 = \frac{J}{2}((S_1+S_2)^2 - S_1^2 - S_2^2)$. This interaction is antiferromagnetic as energies of anti-parallel spins are lower than parallel ones. For classical configurations where the spins are in definite directions $\hat{n}_1$ and $\hat{n}_2$, the ground state energy is minimized when they point in opposite directions and the energy is given by $-J/4$. There are two classical spin configurations which minimize the energy, $|+z\rangle|-z\rangle$ and $|-z\rangle|+z\rangle$. If we now allow quantum effects, we find that true ground state is given by a superposition of these two classical solutions. Specifically, the ground state is the spin-0 singlet, $\psi = \frac{1}{\sqrt{2}}(|+z\rangle|-z\rangle - |-z\rangle|+z\rangle$. The expectation value of either spin vanishes, similar to our expectation for a spin liquid. By allowing superpositions of classical configurations the spins have become entangled, and the energy has been reduced to $-3J/4$. Building on this intuition we should look for spin liquids in systems that have an extensive classical ground state degeneracy.

To find a system with extensive classical ground state degeneracy we can look for interactions between spins which cannot be simultaneously minimized classically. This frustration can come from the interactions not being compatible on-site - the Kitaev honeycomb model reviewed later provides an example of this [78]. Additionally, it is possible that the geometry of the lattice is incompatible with these minimization attempts. The effect of this is evident when you compare the models of spin-1/2 moments on the square and triangular lattice when they couple to nearest neighbors via the anti-ferromagnetic Heisenberg interaction (see

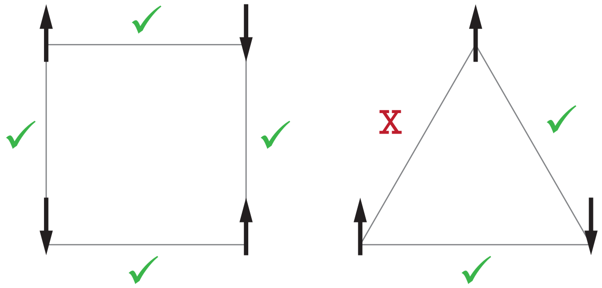

Figure 1.1: On the square lattice spins can be arranged such that all neighbors are antiparallel. On the triangular lattice this isn't possible and leads to a frustration of classical magnetic order.

Fig. 1.2). As demonstrated in the previous paragraph, the classical minimum energy occurs for anti-parallel spins. On the square lattice we see that we can choose spin assignments for each lattice site such that all bonds correspond to interactions which are classically minimized. Once we have chosen the first spin direction, all the rest are fixed, so the classical degeneracy of the ground state is two. On the triangular lattice, the story is different. There is no way to minimize each bond even over just a single triangle. For every two triangles there is at least one bond that is not satisfied. This suggests that the number of classically degenerate ground states for this system is proportional to the system size and therefore we anticipate the system might host a spin liquid.

Fifty years ago, these consideration and the absence of antiferromagnetism in experimental realizations of the triangular lattice antiferromagnet led Anderson to introduce the concept of the spin liquid [9, 118]. Anderson argued that the ground state energy of the triangular lattice Heisenberg antiferromagnet could be minimized by pairing neighboring spins into singlets and then forming a superposition over different ways that the spins could be paired. This wavefunction was called the resonating valence bond state (RVB). In Fig. 1.1(a) one possible covering of the lattice with singlets is shown. As there is no magnetic order in this state, the excitations can't be simple spin flips (spin waves). Instead, an excitation can be generated by imposing the condition that two sites are not coupled into any singlets. From our arguments earlier on the two-spin case, we expect that excitation will cost an energy of order J, the Heisenberg coupling constant. After creating this defect we are left with two decoupled spin-1/2 moments (see Fig. 1.1(b)). Therefore, in the RVB state, instead of the spin-1 spin waves like in a classical magnet, the excitations fractionalize into spin-1/2 quasiparticles. The exchange statistic of these excitations was measured numerically by adiabatically exchanging them and they were found to be fermions [80]. While it was later found that the RVB state wasn't the correct ground state of this model [67], the hypothetical wavefunction would prove to be an insightful mistake (and models would be found that realized it [102]). In particular, the RVB state demonstrates how entanglement in spin systems can lead to the appearance of

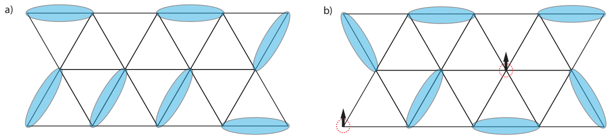

Figure 1.2: (a) One possible dimer covering of the triangular lattice. Each ellipse represents a singlet paired between neighboring spins. The RVB wavefunction is a superposition over different dimer coverings. (b) A dimer covering with two sites left unpaired. These defects carry spin-1/2.

fractionalized excitations with exchange statistics different from their underlying degrees of freedom.

The intuition provided from the RVB state, that the spins fractionalize into fermions, can be utilized by explicitly rewriting the spin operators of a model with a fermionic representation [2, 13]. While such a substitution is always formally valid, a spin liquid occurs when these fermions are deconfined into independent excitations. These techniques are called parton methods and will be used extensively in this dissertation. One such method replaces a spin-1/2 moment S, with fermion creation and annihilation operators $c_\alpha^\dagger, c_\alpha$ [1]:

$$\vec{S} = \sum_{\alpha,\beta=1,2} c_\alpha^\dagger \frac{\vec{\sigma}_{\alpha\beta}}{2} c_\beta, \quad \langle c_\alpha^\dagger c_\alpha \rangle = 1. \tag{1.1}$$

The second equation is a constraint which must be satisfied to remain in the same Hilbert space as the original spin. Without the constraint each two-dimensional spin would be replaced with a four-dimensional Hilbert space. An advantage of this parton method is that it makes explicit the origin of emergent gauge fields. Fundamentally, a gauge symmetry informs us that the presented degrees of freedom overcount the physical ones. Therefore, given a Hamiltonian with effective excitations described unconstrained c fermion, a gauge symmetry could restore the correct Hilbert space by enforcing the constraint Eq. (1.1). This gauge symmetry is explicit as spin S doesn't physically change under an $SU(2)$ rotation of the fermions $c_\alpha \to U_{\alpha\beta} c_\beta$. As this applies to each spin individually, it is a local symmetry (gauge symmetry). However, in any effective model with these degrees of freedom this reparametrization symmetry can be broken to any subgroup of $SU(2)$ such as $U(1)$ and Z_2. This leads to the definition of a quantum spin liquid we will assume in this text as a magnetic system in which such a fractionalization occurs, and an emergent gauge field deconfines. In Chapters Two and Three, we will consider a spin liquid with an emergent Z_2 gauge field and in the fourth we will consider a fractionalized phase with an emergent $U(1)$ gauge field.

The definition that a gauge field becomes deconfined in a spin liquid is a theoretical notion which can be challenging to identify in practice. In gapped phases, this corresponds to a ground state degeneracy known as topological order [160]. In the appendix, we cover an example of how this ground state degeneracy can be argued from the anyonic content of the fractionalized excitations of a particular solvable model (the Toric code) [77]. This ground state degeneracy can be detected in simulation by a universal contribution to the entanglement entropy of the ground state [79]. Recent simulation of spin liquids on analog quantum computers have measured loop operators of spins whose condensation can be shown to imply the deconfinement of a gauge field [137, 158, 49]. However, neither entanglement entropy, nor string operators, are experimentally accessible quantities of material candidates for spin liquids. For material candidates we must relate predictions of a spin liquid's properties to quantities which experiment can report on. Kitaev's solvable honeycomb spin liquid model has provided instructive on this front, and we will now go over this model, and its predictions in detail.

1.1.1 Kitaev Spin Liquids

In this section we will review Kitaev's honeycomb spin liquid model and the associated phases called Kitaev spin liquids. Kitaev's honeycomb model provides a solvable model in which spin-1/2 moments fractionalize into propagating Majorana fermions and static, gapped Z_2 fluxes [78]. The Z_2 fluxes are the excitations of an emergent Z_2 gauge field and act as sources of π flux for the fermions. One strength of the model is that it depends on several parameters which as they are varied allow it to realize several distinct phases of spin liquids. Additionally, the model retains its solubility under certain types of disorder which has made it a useful testbed for understanding how spin liquids interact with disorder.

Kitaev Honeycomb Model and Solution

In the Kitaev honeycomb model neighboring spin-1/2 moments on the vertices of a honeycomb lattice couple via bond-dependent Ising interactions as shown in Fig. 1.3:

$$H = -\sum_{<j,k>_\gamma} J^\gamma \sigma_j^\gamma \sigma_k^\gamma \quad \gamma \in \{x, y, z\}. \tag{1.2}$$

Along one direction a spin is coupled by its z-component, on the other x and so on. Note that the terms all serve to frustrate a possible classical magnetic order. At best, a classical order could only minimize the interaction energy on a third of the bonds. Therefore, according to the arguments of the previous section we expect that this will lead to a large classical degeneracy and possibly a spin liquid state. Remarkably, this model can be solved, and the spin liquid nature of its ground state can be shown directly.

This model can be solved with parton methods in a similar spirit to the fermionic spin representation presented earlier (Eq. (1.1)). For every spin, you introduce four Majorana fermions c, and $b^{x/y/z}$. For every two Majorana fermions, you can create one complex fermionic mode (e.g. $a = c_1 + ic_2$) that can be occupied or not. Therefore, four Majorana fermions create a four-dimensional Hilbert space. This is too large to represent the spins, so a local Z_2 constraint must be enforced to halve the dimension. The spin operators are given by the

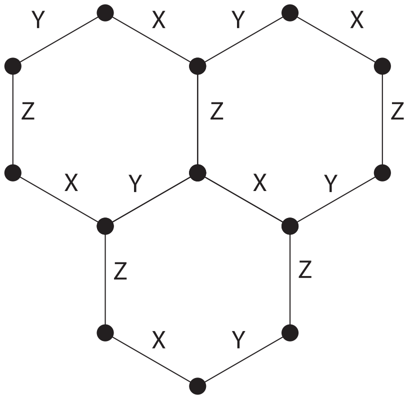

Figure 1.3: In the Kitaev honeycomb spin liquid model, spins are assigned to vertices of the honeycomb lattice and are coupled with bond dependent anisotropic interactions.

product:

$$\sigma_j^\gamma = ib_j^\gamma c_j, \quad D_j\psi = b_j^x b_j^y b_j^z c_j \psi = \psi, \tag{1.3}$$

and the constraint is that the operator D must act trivially on any physical state ψ. As $D^2 = 1$, D is Z_2 valued, and this reduces the dimensionality of the Hilbert space by half. As emphasized in the previous section, a Z_2 gauge field appearing in the effective description of excitations directly corresponds to this constraint.

Substituting the Majorana form of the spin operators into the Hamiltonian reveals it to be a free fermion hopping model for the c Majorana coupled to a frozen Z_2 gauge field. The Kitaev interaction over an x-bond rewritten in terms of fermions is:

$$\sigma_j^x \sigma_k^x = (ib_j^x c_j)(ib_k^x c_k) = -i(ib_j^x b_k^x)c_j c_k = -iu_{jk}c_j c_k, \quad u_{jk} \equiv ib_j^x b_k^x. \tag{1.4}$$

We have defined an operator u_{jk} on the bond between j and k. The other terms work out the same with $x \to \gamma$. The model is solvable because the the bond variables u_{jk} are conserved quantities. To see that they commute with the Hamiltonian, notice all terms of the Hamiltonian are quartic in Majorana and therefore commuting the u_{jk} through them yields a sign $(-1)^8 = 1$ (or $(-1)^6 = 1$ in the special case where the term considered is the same bond as the u_{jk} lives on). They are Z_2 valued because $u_{jk}^2 = (b_j^x)^2(b_k^x)^2 = 1$. The bond variables u_{jk} aren't themselves gauge invariant as $D_j u_{jk} = -u_{jk}D_j$, however the product of u_{jk} over any closed loop of the lattice is gauge invariant. These loop products of the Z_2 bond variables are the physical degrees of freedom of the Z_2 gauge field. The minimal loop wraps a single plaquette, $W_p = \prod_{\langle jk\rangle \in p} u_{jk}$, and when this has eigenvalue (-1) we will say that a Z_2 flux is present in that plaquette. Because u_{ij} corresponds to the hopping phase of a free Majorana fermion, when encircling a Z_2 flux the wavefunction acquires a π phase shift. Once these conserved quantities are fixed, what is left is the free Majorana Hamiltonian:

$$H = \frac{i}{4}\sum_{jk} A_{jk}c_j c_k, \quad A_{jk} = 2J^{\gamma_{jk}}u_{jk}. \tag{1.5}$$

Solving a free Majorana fermion Hamiltonian is similar to that of the more familiar complex fermion case. In the complex case, to solve the system, one simply diagonalizes the hopping matrix A to obtain the single particle energies and creation and annihilation operators of the energy eigenstates. This is possible because any unitary rotation of complex fermion creation and annihilation operators leads to creation and annihilation operators in the new basis. The ground state of the Hamiltonian is then given by the state which has all negative energy modes occupied. The goal of diagonalizing a free Majorana Hamiltonian is the same, to find the complex fermionic energy eigenstates. To form a complex fermionic mode, the Majoranas must be paired. This amounts to finding an orthogonal rotation such that in the new basis of Majorana $\tilde{c}$, the Hamiltonian takes the form:

$$\frac{i}{2}\sum_k \epsilon_k \tilde{c}_k \tilde{c}'_k = \sum_k \epsilon_k (a_k^\dagger a_k - 1/2), \tag{1.6}$$

where the sum runs over positive ϵ_k and $a_k = \frac{1}{2}(\tilde{c}_k + i\tilde{c}'_k)$ is the annihilation operator for the complex fermion energy eigenstate [1]. Therefore, as in the complex Fermion case, free Majorana Hamiltonians can be solved by a diagonalization of the matrix A. This can be accomplished on infinite lattices with translational symmetries or finite lattices (up to large system sizes).

Any solution of the Majorana Hamiltonian Eq.(1.5) requires that we must first fix the background Z_2 field's u_{jk} variables. Fortunately, Lieb's theorem guarantees that when the Kitaev couplings are translationally invariant, the ground state energy of the fermions is minimized when the vacuum is flux free [90, 91]. This sets $W_P = +1$ and fixes the choice of u_{jk} up to gauge equivalent configurations. One choice of a flux free pattern is given by partitioning the lattice into A and B sublattices and setting $u_{jk} = 1$ if j is in the A sublattice. The stability of the flux free state can be tested by introducing a Z_2 flux in this pattern and then calculating the ground state energy difference. As mentioned previously, on a finite lattice this can be calculated by direct diagonalization. By extrapolating to infinite-size lattices, Kitaev found that each isolated Z_2 flux raised the ground state by $\Delta E \approx .015J$ [78]. Given that the Z_2 fluxes are gapped, the flux free background is stable and even in the presence of perturbations, integrating them out should only yield short range interactions for the fermions.

In the absence of Z_2 flux, the model is translationally invariant with respect to the two-site unit cell of the honeycomb lattice and therefore can be solved on infinite lattices [78]. We can

---

[1] A useful trick for calculating the eigenvalues ϵ_k is directly diagonalizing the matrix A will always yield the correct energies even without an orthogonal matrix. The only downside with this technique is you don't know the basis to rotate the Majorana without finding the orthogonal matrices that put the Hamiltonian in the form Eq. (1.6).

take a Fourier transform with respect to these translations by forming $a_\lambda = \frac{1}{\sqrt{N}} \sum_r e^{-iq\cdot r} c_{r,\lambda}$ where N is the total number of vertices and we have introduced a sublattice index $\lambda = A/B$. After the Fourier transform the Hamiltonian decouples at each momentum q:

$$H = \frac{i}{2} \sum_{q,\mu\lambda} A_{\mu\lambda}(q) a^\dagger_{q,\mu} a_{q,\lambda}, \quad iA(q) = \begin{bmatrix} 0 & if(q) \\ -if(q)^* & 0 \end{bmatrix}, \tag{1.7}$$

where $f(q)$ is given by:

$$f(q) = 2(J^x e^{iq\cdot n_1} + J^y e^{iq\cdot n_2} + J^z). \tag{1.8}$$

Here the λ, μ indices correspond to sublattice position, and n_1 and n_2 are the unit cell translations $n_{1/2} = (\pm 1/2, \sqrt{3}/2)$ (setting our length scale of unit cell translations to 1). Diagonalizing this Hamiltonian yields the spectra:

$$\epsilon(q) = \pm |f(q)|. \tag{1.9}$$

The function $f(q)$ has zeros if none of the following inequalities holds:

$$|J^i| > |J^j| + |J^k|. \tag{1.10}$$

If one of these inequalities holds, one coupling is larger than the others and the fermions are gapped. In the anisotropic limit where one of the couplings becomes much larger than the others the system can be described by the Toric code on the square lattice (see appendix for details of the Toric code) [77]. For nearly isotropic couplings, the model then is gapless. Therefore, by tuning the anisotropy of the model it can recognize a stable gapless phase, as well as a gapped phase.

Most of our attention in this dissertation will be near the isotropic point in the gapless phase, and we will make use of its continuum limit low-energy theory. At the isotropic point defined by $J = J^\alpha$, the zero-crossings occur at momenta $k_{K/K'} = \pm(4\pi/3)\hat{x}$. These two crossings are called valleys which we will label with ±. Linearizing the hopping matrix $A(q)$ in momenta near the valley momenta, we get the following:

$$\frac{i}{2} A(K_\pm + p) = v_f(\sigma^x p^y \pm \sigma^y p^x) + \mathcal{O}(p^2) \quad v_F = (3)^{1/2} J/2. \tag{1.11}$$

Therefore, at low energies the fermions are described by two real Dirac fermions. The continuum limit low-energy theory in the absence of Z_2 flux is thus described by Hamiltonian:

$$H = \int \frac{d^2p}{(2\pi)^2} (\psi_K(p)^\dagger (\vec{\sigma} \cdot \vec{p}) \psi_K(p) + \psi_{K'}(p)^\dagger (\vec{\sigma}^* \cdot \vec{p}) \psi_{K'}), \tag{1.12}$$

where $\psi_{K/K'}(p)$ are fermionic annihilation operators with momenta (p) relative to the valley points and the Fermi velocity (v_F) has been set to 1. The Dirac fermion low-energy theory of the gapless Kitaev spin liquid phase will be the starting point of our analysis in chapter Three. Familiar from the low-energy theory of graphene, the Dirac fermion's gaplessness is protected by time-reversal symmetry and inversion symmetry. However, unlike graphene, the real space fermion operators are Majorana fermions and therefore particle-hole symmetry cannot be broken by creating a trivial inversion symmetry breaking mass [78]. Therefore, only perturbations which break time-reversal symmetry can open a gap in this low-energy theory.

When time-reversal symmetry is broken in the gapless Kitaev spin liquid, the Dirac fermions acquire a topological gap and the model enters a non-abelian spin liquid phase [78]. One way to break time-reversal symmetry is to apply a uniform magnetic field to the system $\delta H = -\mu \sum_i \vec{h} \cdot \vec{\sigma}$. For weak fields, $|H| \ll J$, this addition can be treated in perturbation theory. This is because applying a spin operator to the ground state must create a pair of Z_2 fluxes which are gapped with an energy cost proportional to the Kitaev coupling J. The leading non-constant contribution from perturbation theory of this operator comes at third order. It has a strength of $\kappa = \frac{6h_x h_y h_z}{(\Delta E)^2} \propto \frac{h_x h_y h_z}{J^2}$, where ΔE is the energy of creating two adjacent fluxes. In the fermion description, these terms are given by imaginary second-neighbor hoppings ($i u_{ij} u_{jk} c_i c_k$) and a local quartic interaction. The exact ground state can still be found by diagonalizing Eq. (1.5) if only the second-neighbor hoppings are retained. This is because the model is simply a Majorana version of the Haldane model [57]. However, the precise nature of time-reversal symmetry breaking is irrelevant for the low-energy theory which is always only modified by the inclusion of a mass with opposite sign in the valleys (for the convention of the Dirac Hamiltonians Eq.(1.12)) [78].

Physical Properties of Kitaev Spin Liquids

Now that we have reviewed the solution of the Kitaev honeycomb model, we aim to relate the distinct phases of the spin liquid to experimentally accessible predictions. An example of a commonly accessible experimental quantity is the the expectation values of the spins in Kitaev spin liquid candidates. Measuring this in experiments on materials this is possible with elastic neutron scattering (yielding a Fourier transform of the spin texture) [17]. For analog quantum simulations of the phase on Rydberg atoms measuring the spins could be locally accomplished with fluorescent imaging [137]. With inelastic scattering experiments like like neutron scattering [17, 18, 19] or time-domain Terahertz spectroscopy [94, 172] the imaginary part of the magnetic susceptibility is measured. By the fluctuation-dissipation theorem this allows experimental access to spin-spin correlation functions [97]. Additionally, heat transport can be measured with thermometry [72, 71, 44]. All of these probes can be related to properties of the Kitaev spin liquid which can distinguish it from other phases.

Many physical properties of the Kitaev spin liquid follow from the absence of Z_2 fluxes in the ground state ($W_P = +1$) and the fact that each spin operator σ^γ anticommutes with two adjacent plaquette operators. Rewriting the flux operator with spins, $W_P = \sigma_1^z \sigma_2^x \sigma_3^y \sigma_4^z \sigma_5^x \sigma_6^y$ (labeling the spins clockwise starting from the topmost of a plaquette), we find that for any site, two types of Pauli operators will anticommute with W_P. That is, any spin operator acting on the ground state creates two Z_2 fluxes (defined by $W_P = -1$) and must result in a state orthogonal to the ground state. Therefore $\langle \vec{S} \rangle = 0$, and as in the initial vision of a spin liquid presented in this chapter, the Kitaev spin liquid possesses no magnetic order.

The conservation of Z_2 fluxes in the Kitaev spin liquid also implies distinct features of the spin-spin correlation functions in the ground state. First, these correlation functions are highly local. For the two-spin correlation functions, the only non-vanishing terms are given by those with spins on-site or across a nearest neighbor bond to preserve $W_P = +1$ [78]. Second, the fractionalization of the spin operators into Z_2 gauge field degrees of freedom (fluxes) and Majorana fermions will be manifest as the two-spin function will have the character of a multi-particle correlation function. That is, unlike the sharp response that the dynamical structure factor (Fourier transformed spin-spin correlation function) has in magnetically ordered phases [153], where it captures the sharp dispersion of a single spin flip. In the Kitaev spin liquid, the dynamical structure factor captures the continuum response of all possible pairs of fluxes and Majorana fermions at a fixed momentum. Because the Z_2 fluxes have no dispersion, they act like momentum sinks for this pair and the dynamical structure factor won't reveal a changing dispersion as total momentum is changed. The exact dynamical structure factor has been calculated [81] and can be compared to experimental realizations [17].

In the non-abelian phase of the Kitaev spin liquid there are additional robust features which can be used to confirm the phase. Many of these features can be argued straightforwardly by considering two uncoupled layers of the spin liquid. By doing this we can identify the doubled Kitaev spin liquid as a quantum Hall state and utilize this state's topologically protected properties [85] to imply properties about the individual spin liquid layers. This is made possible because for free Majorana Hamiltonians like Eq. (1.5), if two identical copies are added together the resulting Hamiltonian has an identical hopping matrix (up to a constant multiple). The Majorana fermions are replaced with complex fermions $a = c_1 + ic_2$ built from the two layers. Complex Dirac fermions which are gapped by the breaking of time-reversal symmetry give rise to a quantized Hall conductivity [57], this implies several features for the real fermion case relevant to spin liquids. While there is no charge current for real fermions, as fermion number isn't conserved, there can be energy transport. Due to the existence of complex gapless chiral edge modes in the quantum Hall effect state, there must be real gapless chiral edge modes in each layer. These will carry an energy current leading to a quantized thermal Hall conductivity $\kappa_{xy}/T = \frac{\pi^2 k_b^2}{6h}$, which is exactly one-half of the thermal conductivity of the $\nu = 1$ quantum Hall effect state [78, 29]. A measurement of this exactly quantized result would be a smoking gun signal of the non-abelian Kitaev spin liquid.

Another implication of the quantized Hall conductivity of the doubled non-abelian Kitaev spin liquid is that all Z_2 fluxes should carry unpaired Majorana zero modes. This is the hallmark of the Ising anyon, which can fuse to the vacuum or a fermion [78], and this nontrivial fusion is why this phase is called the non-abelian Kitaev spin liquid. This can be argued by adiabatically threading a Z_2 flux (one half a flux quantum in the language of the quantum Hall state) in the doubled system. The quantized Hall-conductivity implies that the flux then carries an excess $+1/2$ charge [85]. However, switching the layers corresponds to a charge conjugation symmetry which would create a $-1/2$ excess charge Z_2 flux state with the same energy. The operator which takes you from one state to the other must correspond to a zero-energy charge 1 complex fermionic mode. This complex zero-energy mode implies the existence of an unpaired Majorana zero mode associated with the Z_2 flux in each layer. So long as these Z_2 fluxes are kept well-separated, their bound modes should have energy zero up to exponentially small corrections in the distance between them. This makes them of interest for quantum computation as any form of local error can only change the wavefunction in the ground state subspace with rate exponentially suppressed in the distance between the Z_2 fluxes [78, 106]. Detection of this zero mode could be accomplished with thermal interferometry if the Z_2 fluxes could be reliably created and trapped [159].

Experimental evidence to date has rejected several material candidates and remains inconclusive for others. Fortunately, the Kitaev interaction (Eq.(1.2)) has been shown to be a natural consequence of strong spin-orbit coupling in certain insulators [65, 168]. A prescription was given to find heavy 4d and 5d transition-metal based insulators which were expected to have large effective Kitaev couplings. From this several material candidates have been explored such as Li_2RhO_3, $\alpha-RuCl_3$ and Na_2IrO_3 [168]. However, all of the candidates exhibit magnetic order at sufficiently low temperature, therefore without modification they aren't in the Kitaev spin liquid phase. Excitement was generated by neutron scattering experiments for $\alpha-RuCl_3$ which demonstrated a continuum of magnetic excitations which persisted above the magnetic ordering temperature [19]. It was suggested that this continuum represented the fractionalization of a spin flip operator into a pair of fluxes and a Majorana fermion [81]. $\alpha-RuCl_3$'s magnetic ordering was shown to be suppressed with applied magnetic field [18]. For a tilted out of plane magnetic field there exist claims of observation of the quantized thermal Hall conductivity of the non-abelian Z_2 spin liquid [71, 175], however other groups have not reproduced the same result [44]. Therefore, the status of $\alpha-RuCl_3$ as a spin liquid in applied field is not definite, nor is even the effective model that describes it at low-fields. In Chapter Two we describe an effective model of α-$RuCl_3$ to consider whether certain experimental signatures are related to fractionalization or if they have more conventional explanations.

In realistic models of materials, we must include the possible anisotropy and disorder present in them. We can then ask what properties of the perfect and clean material persist or how do they change? The Kitaev model offers a unique opportunity for this because the couplings J can be different on each bond and the model is still solvable on finite lattices. Lattice vacancies are a naturally occurring form of disorder which is defined by removing a spin from the material. This can be simply included in the Kitaev model by turning off all couplings to an individual site. In this case Lieb's theorem no longer guarantees a flux free background in the ground state [91, 90]. Within the Kitaev honeycomb model, it was shown numerically that when a lattice vacancy was created a Z_2 flux was energetically favorable to be placed through the vacancy [163, 164, 70]. If this was a robust feature of the Kitaev spin liquid it could be utilized to create and trap Ising anyons. Inteferometry experiments could then be utilized to confirm the phase imparted on fermions from the Z_2 flux which would be direct evidence that the material was a spin liquid. In Chapter Three we will consider the energetics of lattice vacancies binding Z_2 fluxes from a perspective which only depends on the universal properties of the spin liquid phases to confirm that this isn't only a feature of Kitaev's integrable model, but instead extends to generic Kitaev spin liquids.

1.2 Heavy Fermion Materials and Fractionalized Fermi Liquids (FL*) Review

In this section we will review the heavy fermion systems, which are the topic of Chapter 4. First, we explain the standard theory for emergence of a large effective mass in these materials through condensation of a valence fluctuation in a microscopic Kondo lattice model. Then, we discuss the possibility for establishment of a fractionalized metallic phase on the other side of the condensation transition. Unlike the Kitaev spin liquid section, which started with an exactly solvable model to describe a hypothetical material, in this section we will be confronted with the task of explaining real experimental observations. Developing a solvable model of the phenomenon reviewed in this section will be the target of Chapter Four.

A curious observation that started the heavy fermion material story was that the specific heat capacity and electrical resistivity of $CeAl_3$ is several orders of magnitude larger than of typical metals [11]. To interpret these results we can turn to Landau's paradigm of Fermi liquids [83]. In a Fermi liquid, despite potentially strong (bare) interactions, near the Fermi surface (or the boundary between occupied and unoccupied fermionic levels) interactions become effectively weak due to a lack of available phase space for scattered states. Therefore, for experimentally accessible quantities at low-temperatures, the physics is described by classical quasiparticles with a renormalized mass m^* and a long lifetime $1/\tau \sim T^2$. By utilizing these quasiparticles, it can be shown that the specific heat, $C_V/T = \gamma \propto m^*$, and the electrical resistivity, $\rho = \rho_0 + AT^2$ (with $A \propto (m^*)^2$), follow a common form in Fermi liquids. From this the large specific heat and electrical resistivity in $CeAl_3$ could be understood if the effective mass was increased nearly three orders of magnitude compared to typical values [11]. Over the years many more metals were found with similarly enhanced effective mass and these heavy fermion materials would become some of the most robust evidence of Landau's Fermi liquid theory's predictions [68].

A common factor in these heavy fermion materials was the presence of rare earth or actinide ions with tightly bound d and f orbitals [35]. A reasonable expectation is that a lattice of such ions creates a very weakly dispersing band of electrons that when hybridized with the other conduction bands will create a Fermi surface with large effective mass (see Fig. 1.4). In the limit of complete immobility for electrons in the d and f orbitals, we can model these degrees of freedom as just spins. Following this reasoning, Doniach suggested that the Kondo lattice model described heavy fermion metals [45, 73]. In the Kondo lattice model, spins arranged on a lattice couple to the spin moments of the conduction electrons:

$$H = \sum_{k,\alpha} \epsilon_{c,k} c^\dagger_{k,\alpha} c_{k,\alpha} + J_K \sum_{r,\alpha,\beta} (\vec{S}_r \cdot c^\dagger_{r,\alpha} \vec{\sigma}_{\alpha\beta} c_{r,\beta}). \tag{1.13}$$

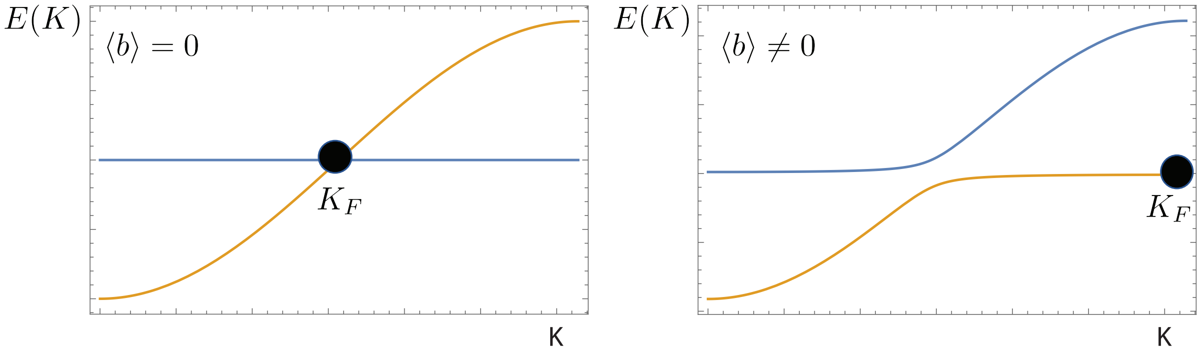

Figure 1.4: Schematic picture of the formation of a heavy fermion metal. Left: The blue band is the localized f fermions and the orange band corresponds to the conduction electrons c. If no singlets have formed they are uncoupled. Right: When the two bands hybridize the Fermi surface of the conduction fermions grows and the effective mass near the Fermi surface greatly increases.

This model isn't directly solvable, so approximations are necessary to understand how it leads to the formation of a heavy fermion material.

To understand the formation of the heavy fermion material from the Kondo lattice model, we can briefly consider the simpler problem of a single spin-1/2 impurity coupled to a Fermi liquid [134]. As described in previous sections, a coupling $J_K \vec{S} \cdot \vec{\sigma}$ is minimized for spin singlets. However, we expect that the dispersion of the conduction fermions competes with this localizing effect. Kondo explored this problem to understand a minimum in electrical resistivity at low temperatures [82]. Both Kondo and Anderson concluded that this was caused by a logarithmic growth of the effective Kondo coupling as the temperature lowered using perturbative arguments [5]. From this logarithmic growth, $J_K(T)$ grows to order unity and outside the validity of perturbation theory when the temperature is less than the Kondo temperature, $T_K \sim \Lambda \exp^{-1/(2\nu J_K(0))}$ (where Λ is the bandwidth of the conduction fermions and ν is the density of states at the Fermi surface) [5]. The fact that J_K continues to grow beyond the perturbative regime was confirmed by nonperturbative renormalization group calculations later in an early success of Wilson's program [165]. As J_K becomes large, the spin impurity will form a singlet with the adjacent conduction fermion site to minimize the interaction energy (as discussed in the spin liquid review). In the strong coupling limit, the model can be taken to be non-interacting by ignoring the impurity and placing an on-site potential $Vc^{\dagger}_{0,\alpha} c_{0,\alpha}$ which removes the singlet bound conduction electron as $V \to \infty$. This equivalent perspective suggests that the low-temperature physics is described by a Fermi liquid scattering off the screened impurity [107]. Following this line of reasoning, Noziére showed that the resulting Fermi liquid would have a scattering resonance due to the impurity spin. For energies near this resonance the quasiparticles would have a large effective mass set by the inverse of T_K, corresponding to a mixing of the localized spin and the conduction electrons. We imagine then that as the number of impurity spins grows that the resonances would form a section of the Fermi surface and the system would become a heavy fermion material.

Using parton techniques with the Kondo lattice model ((Eq. (1.13)) it can be argued that this screening of spins leads to a heavy fermion material [125, 14, 138, 139, 132]. As in the spin liquid sections, we begin our study of the possible fractionalizations with a parton technique and decompose the spin into fermions subject to a constraint:

$$\vec{S}_r = \sum_{\alpha,\beta} f^\dagger_{r,\alpha} \frac{\vec{\sigma}_{\alpha\beta}}{2} f_{r,\beta}, \quad n_{f,r} = 1. \tag{1.14}$$

This single occupancy constraint can be enforced by introducing a Lagrange multiplier field into the Hamiltonian:

$$\delta H = \sum_r i\lambda_r (n_{f,r} - 1). \tag{1.15}$$

λ_r is a complex valued field and we have multiplied by i for convention. With this substitution the Kondo interaction becomes a quartic fermion interaction:

$$-J_K \sum_{r,\alpha,\beta} (f^\dagger_{r,\alpha} c_{r,\alpha} c^\dagger_{r,\beta} f_{r,\beta} + \frac{1}{2} f^\dagger_{r,\alpha} f_{r,\alpha} c^\dagger_{r,\beta} c_{r,\beta}). \tag{1.16}$$

Due to the single occupancy constraint of the f fermions, the second term is just a shift of chemical potential for the c fermions and can be absorbed into the definition of the dispersion $\epsilon_{c,k}$. This quartic term can be decoupled by introducing a bosonic field b_r via a Hubbard-Stratonovich transformation [125, 14, 138, 139, 132]:

$$-J_K \sum_{r,\alpha,\beta} f^\dagger_{r,\alpha} c_{r,\alpha} c^\dagger_{r,\beta} f_{r,\beta} \to -\sum_{r,\alpha} (b_r f^\dagger_{r,\alpha} c_{r,\alpha} + H.c.) + \sum_r \frac{b^\dagger_r b_r}{J_K}. \tag{1.17}$$

Collecting terms, the Hamiltonian is given by:

$$H = \sum_{k,\alpha} \epsilon_{c,k} c^\dagger_{k,\alpha} c_{k,\alpha} + \sum_r i\lambda_r (n_{f,r} - 1) - \sum_{r,\alpha} (b_r f^\dagger_{r,\alpha} c_{r,\alpha} + H.c.) + \sum_r \frac{b^\dagger_r b_r}{J_K}. \tag{1.18}$$

In the parton description it becomes clear that the formation of a heavy fermion material corresponds to the condensation of the boson b. If b condenses, then the conduction fermion c mixes with the dispersionless f fermions and becomes heavy. Additionally, when b is condensed the f fermions will become part of the c Fermi surface - a fact which was anticipated from the single spin case. Therefore, in the heavy fermion material phase we expect a Fermi liquid phase with Fermi volume that includes both the conduction fermions and the spins. By Luttinger's theorem, this must be the case [96, 108].

At this point, all manipulations of the Kondo lattice model have been exact, however, to demonstrate that this condensation occurs we must utilize approximations. Anticipating the condensation of b, we can perform a mean-field analysis treating the boson $b_r = b_0$ and the lagrange multiplier field $\lambda_r = \lambda_0$ as constants. The Hamiltonian (Eq. (1.18)) then becomes described by free fermions. The self-consistent mean-field equations are:

$$b_0 = \frac{J_K}{V} \sum_{k,\sigma} \langle c^\dagger_{k\sigma} f_{k\sigma} \rangle \,, \quad 1 = \frac{1}{V} \sum_{k} \langle f^\dagger_{k\sigma} f_{k\sigma} \rangle \,. \tag{1.19}$$

Here V is the number of lattice sites. Notice that at the mean-field level, b is the hybridization of c and f, and the second equation says that $n_{fr} = 1$ is satisfied on average. From these equations it was shown that for any J_K, a condensation of b_0 occurs for temperatures lower than the Kondo temperature T_K that appeared in the single spin problem [41]. Therefore, at least in the mean-field approximation a heavy fermion material is established as the ground state of the Kondo lattice model.

These mean-field solutions can be justified in a large-N limit of the number of spin components [36, 34, 125, 14]. This is accomplished by promoting the $SU(2)$ indices of the fermions $\alpha = 1, 2$ to N $SU(N)$ components. With this substitution and a rescaling of the Kondo coupling, $\frac{J_K}{\sqrt{N}}(b_r f^\dagger_{r,\alpha} c_{r,\alpha} + H.c.)$, the action becomes extensive in N. As the action is proportional to N, path integrals will be dominated by their saddle-point solutions in the large-N limit - namely the solutions of the mean-field equations in the previous paragraphs. Therefore, finding the saddle point solutions amounts to an exact solution in this limit. In this large-N limit, due to the asymmetry of the limit between the number of bosons and fermions, the self-energy for fermions which comes from scattering from the single species of bosons is suppressed $1/N$ and vanishes. Thus, within the large-N limit, the formation of a heavy fermion material was shown - however, it was at the cost of removing the possibility of any strongly coupled physics (precluding non-Fermi liquid behavior).

If heavy fermion materials couldn't be driven to phase transitions and their physics was always well described by weakly coupled fermions, then the role of a theorist would be finished. However, heavy fermion materials have been observed to undergo phase transitions by application of magnetic fields, pressure and charge doping to metallic phases with smaller Fermi surfaces corresponding to the charge density of the conduction band alone [143, 109, 51, 98]. Luttinger's theorem tells us that the charge density is always given by the Fermi volume [96, 108]. As this charge density is measured per unit cell, the breaking of translational symmetry during a phase transition naturally results in a discontinuity of the Fermi volume with respect to the new Brillouin zone [143]. However, recent experimental evidence has shown that the heavy fermion material CeCoIn_5 can be tuned to a small Fermi surface phase without breaking translational symmetry [98]. The Hall coefficient $R_H = \frac{E_y}{j_x B_z} = \frac{\rho_{xy}}{\mu_0 H}$ at high-fields is a measure of the charge carrier density n. In this limit, $R_H = \frac{1}{en}$. Tracking the Hall-coefficient while doping revealed that the number of charge carrier density suddenly shifted (see Fig. 1.5). The implication is that the assumptions of Luttinger's theorem cannot

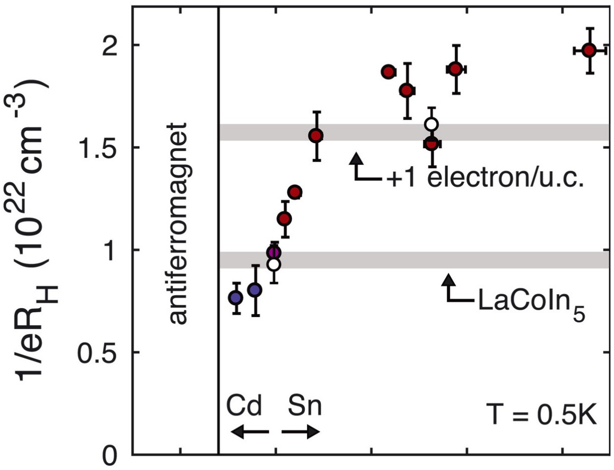

Figure 1.5: Inverse Hall coefficient measurement of CeCoIn$_5$ as a function of doping. Tin doping leads to a sudden increase in charge carrier density. This image is reproduced from [98].

be true on both sides of the phase transition, namely that both phases cannot simply be Fermi liquids.

The phase transition observed in CeCoIn$_5$ can be understood if an emergent $U(1)$ gauge field becomes deconfined when entering the small Fermi surface phase [138]. The origin of the $U(1)$ gauge field can be seen in our parton analysis by the constraint $n_{fr} = 1$, as emphasized in the previous section. The model obeys a $U(1)$ gauge symmetry where λ is the time-component of the emergent gauge field. The gauge symmetry is manifest in the lagrangian term $f_{r,\alpha}(\partial_\tau + i\lambda_r)f_{r,\alpha}$, where the gauge symmetry acts by transforming $f_{r,\alpha} \to e^{i\theta_r(\tau)} f_{r,\alpha}$ and $\lambda_r \to \lambda_r - \partial_\tau \theta_r(\tau)$. As b is related to f by $b \sim c^\dagger f$ they both have charge $+1$ under this gauge symmetry. Therefore, the ground states of the system represent phases of an emergent $U(1)$ gauge theory coupled to matter fields [138, 139, 52]. In the heavy fermion material phase, b, charged under this emergent $U(1)$ symmetry, is condensed and therefore this emergent gauge field is in the Higgs (or confined) phase. If the Hamiltonian is perturbed such that the ground state has $\langle b \rangle = 0$, then the $U(1)$ gauge field is deconfined, the Fermi surface of the c fermion will shrink by excluding the f fermions and no local symmetry is broken.

This $U(1)$ deconfinement transition can be accommodated in the mean-field picture that we have reviewed with a natural modification. The spin moments will generally interact with each other via the Ruderman-Kittel-Kasuya-Yosida interaction (RKKY) which leads to antiferromagnetism [128, 73, 176]. A simple model of the impact of this antiferromagnetic interaction is provided by introducing nearest-neighbor Heisenberg interactions $J_H \sum_{\langle rr' \rangle} \vec{S}_r \cdot \vec{S}_{r'}$. Including this in the parton mean-field formalism only modifies the Hamiltonian by introducing a dispersion $\epsilon_f(k)$ for the f fermions. For finite J_H couplings, this change is sufficient to uncondense b and deconfine the $U(1)$ gauge field [138, 139].

We therefore have learned quite a bit about the phase transition under which the Fermi surface suddenly changes volume without breaking symmetry from this mean-field theory, or equivalently this large N limit. As mentioned previously, these approximations came at the cost of vanishing fermion self-energies. This is at odds with experimental observations of electrical resistivity at finite temperatures above the critical point, where linear in temperature resistivity, unlike the robust T^2 prediction of Fermi liquid theory is obtained [98]. This non-Fermi liquid “strange metal” behavior originally observed in the normal state in high T_c superconductors [150, 40] has now been observed near many metallic critical points [144, 146, 98, 152, 109]. Therefore, it is expected that the this phenomenon is then connected to fermions coupling to critical fluctuations [32, 21, 139, 115]. A fascinating aspect of the strange metal phenomenology is that there is growing evidence of an lower bound on the transport timescale $\tau \sim \frac{\hbar}{k_B T}$ which has been dubbed the “Planckian time”. This timescale is determined only by fundamental constants and the temperature [27, 152, 60, 28, 89, 130]. In Chapter Four we will develop a new large N approach to this problem that can describe this strongly coupled physics.

Chapter 2

Magnetic Field Evolution of Magnons in Kitaev Material α-RuCl$_3$

2.1 Introduction

While the Kitaev model's anisotropic bond-dependent couplings may seem unphysical, it has been shown that the Kitaev interaction is a natural outcome of strong spin orbit coupling in a number of transition metal insulators [65, 168]. In this chapter we describe and explain an experiment on such a material, α-RuCl$_3$, that has been suggested to be proximate to the Kitaev spin liquid state [19, 17, 18, 133]. The experiment was performed by Joseph Orenstein's group and led by Liang Wu and Arielle Little and and we provided the theoretical modeling and analysis of the results [171].

Similar to the Kitaev honeycomb model, in α-RuCl$_3$, effective spin 1/2 moments live on the honeycomb lattice and interact primarily with their in-plane neighbors [168]. Unlike the Kitaev spin liquid, α-RuCl$_3$ is found to be magnetically ordered below $7K$ [135]. Below this temperature the spins align ferromagnetically on zigzag lines through the honeycomb lattice and adjacent ferromagnetic lines are anti-aligned (see Fig. 2.1). As there are three ways to pass orient a zigzag line through the honeycomb lattice, there are three C_3 rotation-related zigzag orders. In the absence of C_3 symmetry breaking, these magnetic orders represent degenerate ground states. We find that this degeneracy leads to large experimental differences when even small amounts of disorder are introduced.

Ever since it was realized that spin-orbit coupling can lead to the Kitaev interaction in transition metal compounds like the iridates and α-RuCl$_3$, there has been a hunt for materials in the phase [65, 30, 168]. Unfortunately, unlike the Kitaev model, all known material candidates magnetically order at low temperatures [95, 31, 33, 23, 151, 135]. The question that remains is, are these materials proximate to the Kitaev spin liquid phase, and if so, can they be pushed into those phases by some accessible means?

In α-RuCl$_3$ probes of the magnetic excitations have yielded suggestive evidence of a closeness to the Kitaev spin liquid. The results of inelastic neutron scattering [19, 17, 18] and

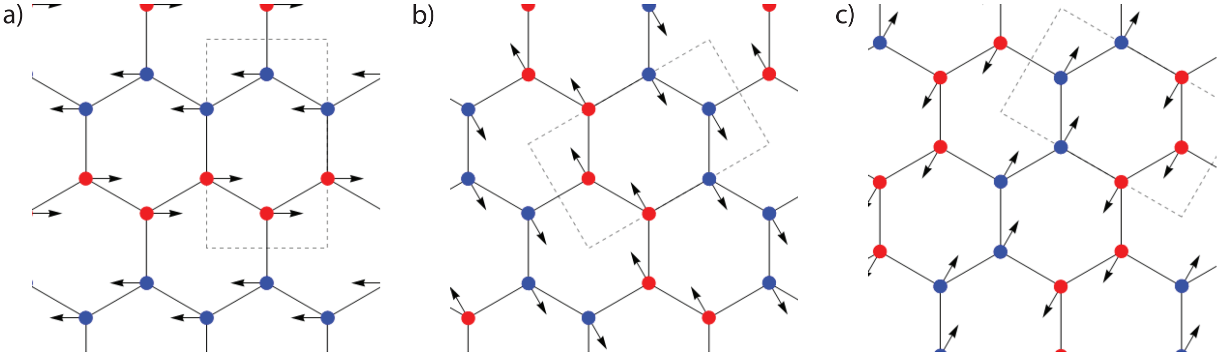

Figure 2.1: The three possible zigzag magnetic orders. The four-site unit cell is shown by gray dotted lines. (a) Q=Y (b) Q=M (c) Q=M’

Raman spectroscopy [133] have shown a broad continuum of scattering at high energies and $Q = 0$ (zero momenta transferred). This is seen in addition to sharper magnon excitations. It was suggested that this continuum scattering is related to the continuum scattering expected from Kitaev spin liquid where a spin fractionalizes into majorana fermions and a Z_2 magnetic flux [81, 17, 18]. However, other authors have suggested that such a continuum corresponds to anharmonic behavior expected due to a frustrated classical order and is not a strong indicator of proximity to the Kitaev spin liquid [166].

Further excitement was generated by indications of a field-induced transition into a magnetically disordered state [136, 15, 178, 86, 18], as well as reports of a quantized thermal Hall conductivity in this regime [71, 175]. However, THz spectroscopy experiments have shown that the spectral weight of the continuum excitations doesn’t grow as a function of magnetic field up until the critical field which suggests the nature of excitations in the adjacent phase aren’t related to this scattering feature [94].

In this chapter we report and explain a measurement of the magnetic excitation spectrum in α-RuCl$_3$ via time-domain THz spectroscopy (TDTS). With this technique the zero-momenta spin-spin correlation function is accessed via measurement of the magnetic susceptibility. We find that all features observed can be described with calculations based on linear spin wave theory (LSWT), provided we assume the presence of a random C_3 breaking anisotropy which generates a multidomain structure of the magnetic order. Additionally, we find that broad continuum excitations can be explained with contributions from two-magnon states.

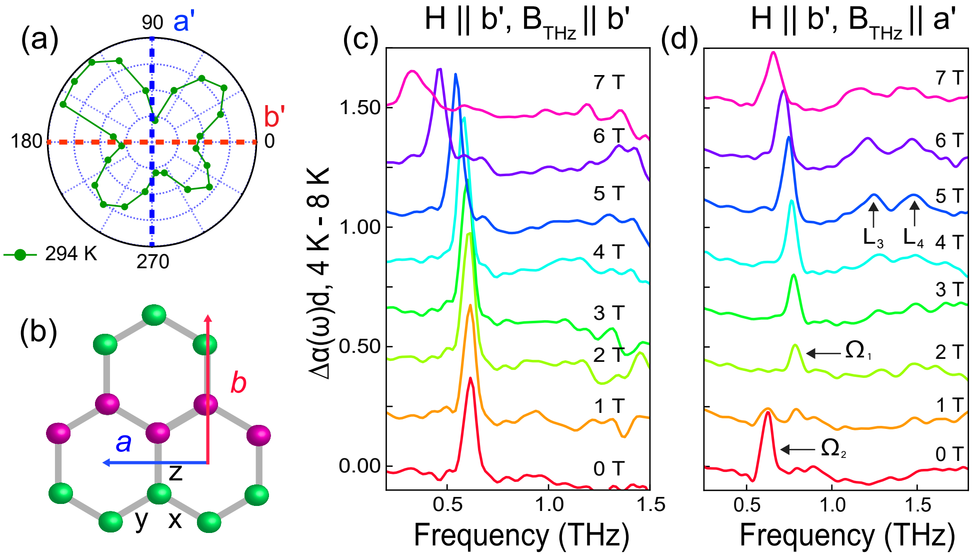

Figure 2.2: (a) Transmitted THz electric field amplitude at T = 294 K as a function of sample angle. Blue and red lines represent the minimum transmission axes at a' and b' [94] (b) Schematic of honeycomb structure showing a and b monoclinic axes relative to Ru-Ru bonds. Color of atoms illustrates zigzag order. Bond labels x, y, and z denote the component of the spin interacting along a given bond in the Kitaev model. (c) Magnon absorption as a function of frequency for $H \parallel b' \parallel B_{THz}$ and $H \parallel b' \perp B_{THz}$ respectively. The magnon contribution is extracted from the total THz absorption by subtracting a reference at T = 8 K, above T_N, from a T = 4 K spectrum at each field. Traces are offset for clarity.

2.2 Experimental Details

In this experiment, THz pulses are passed through α-RuCl$_3$ and the time delay for a return echo, paired with the frequency resolved absorption rate allows for a determination of the imaginary part of the magnetic susceptibility [94]. By measuring the transmission coefficient of these pulses $t(\omega)$ we access the absorption coefficient $\alpha(\omega)$ by the following relationship:

$$t(\omega) \approx \frac{4n}{(n+1)^2} e^{-\alpha(\omega)d}, \tag{2.1}$$

where n is the index of refraction of the material, and d is the length of the sample. $\alpha(\omega)$ has magnetic and dielectric contributions. To isolate the contribution which comes from magnetic dipole coupling it is useful to consider the differential absorption $\Delta\alpha(\omega)$ where the absorption from $T = 8k > T_N$ (the ordering temperature) is subtracted [94]. The imaginary part of the dynamic magnetic susceptibility can then be calculated:

$$\chi''(\omega) = \frac{4\Delta\alpha(\omega)d}{\omega T_{rt}}, \tag{2.2}$$

where here T_{rt} is the time of a THz pulse to travel through the system and then make a return echo. The THz pulses are linearly polarized before entering the sample. A DC magnetic field is applied to the sample in parallel and perpendicular in-plane directions between $0 - 7$T.

Directions for polarization of THz spectroscopy and orientation of DC field were guided by first finding the axes of the honeycomb layers. THz electric field amplitude was measured when rotated between crossed linear polarizers, as shown in Fig. 2.2. A pure honeycomb lattice has C_3 rotational symmetry, which would manifest in such a plot by zeros of transmitted intensity along the honeycomb's a or b axes. As this is not observed in experiment, C_3 symmetry must be broken. One possible explanation, which we promote, and micro-Laue diffraction confirms, is the presence of an elongation of one of the three bond directions and the presence of several patches of different bond anisotropy. As there are clear minima nodes in the plot, one of the three possible lattice distortions is the dominant anisotropy and can be identified as effective axes for the system a' and b'. With the dominant axes of the system charted the TDTS could be done with applied external field along directions referencing the underlying honeycomb lattice.

Now we can summarize the main experimental findings. In Fig. 2.2(c) and (d) the differential absorption coefficient shown for TDTS with applied external fields $H \parallel b'$ with THz pulses polarized along the b' and a' axes respectively. At $H = 0$T, two well-defined magnon peaks appear in the different polarizations. In the parallel polarization (Fig. 2.2(c)), the magnon peak continuously evolves as the field is increased. In the perpendicular channel (Fig. 2.2(d)), there is a discontinuity in the magnon evolution near 1.5T. At high fields ($\sim$ 5T), two higher energy broad excitations labeled L_3 and L_4 appear in the perpendicular channel.

2.3 Theoretical Description

Starting with a family of Hamiltonians suggested by ab-initio studies [167] we will demonstrate a set of parameters which lead to the phenomenon observed. We will start by finding the classical magnetic order of the model. Then we will perform a semiclassical expansion about this order known as linear spin wave theory (LSWT) to find the magnetic excitations. From this, we can compare predictions of the absorption to the TDTS experiment. We will show that to explain the discontinuous evolution of the magnon absorption it will be necessary to assume the existence of patches with differing anisotropy. Finally, we will show that the next leading order in this semiclassical expansion which involves pairs of spin wave excitations is sufficient to explain the continuum features.

2.3.1 Linear Spin Wave Theory

The starting point for the LSWT calculations is the effective spin Hamiltonian,

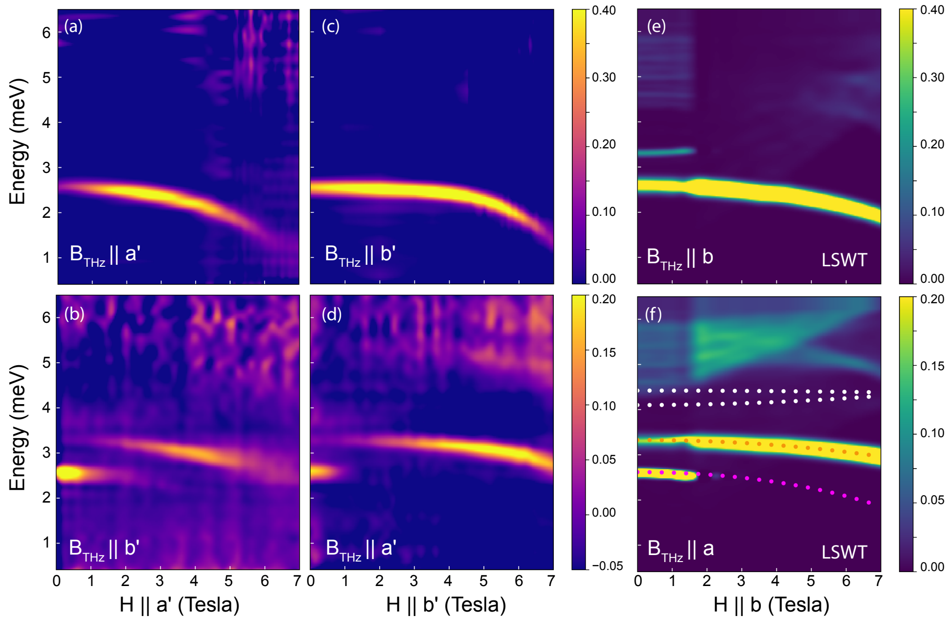

Figure 2.3: Magnon energies and absorption strengths at $Q = 0$ as a function of external in-plane magnetic field, H. Experimental data is in panels (a)-(d). Magnon absorption was extracted by subtracting the 8 K spectra from the 4 K spectra at each value of H. Spectra were taken in 0.2 T steps from 0 - 5 T and in 0.1 T steps from 5 - 7 T; intermediate field values are interpolated. The mode dispersion is shown for four configurations of H and the THz probe field, B_{THz} relative to a' and b': (a) and (c) show $H \parallel B_{THz}$ along the a' and b' directions respectively, while (b) and (d) show $H \perp B_{THz}$. Note the difference of color scales: absorption in the parallel configuration is roughly twice as strong. Panels (e) and (f) show LSWT calculations for absorption in $H \parallel b$ with the probe field parallel and perpendicular, respectively. Solid dots overlaid on (f) represent mode energies predicted by LSWT. The orange and pink dots coincide with observed Ω_1 and Ω_2. Two higher energy modes (white dots) are forbidden by selection rules and do not contribute to THz absorption. Intensity in the region 4 - 6 meV results from 2-magnon absorption and is consistent with observed features L_3 and L_4.

$$\begin{aligned} H_S = &\sum_{<ij>} \left[J_1 S_i \cdot S_j + \Gamma(S_i^{\alpha_{ij}} S_j^{\beta_{ij}} + S_i^{\beta_{ij}} S_j^{\alpha_{ij}}) + K S_i^{\gamma_{ij}} S_j^{\gamma_{ij}} \right] \\ &+ \sum_{<ij>_3} J_3 S_i \cdot S_j - \mu_B g \sum_i H \cdot S_i \end{aligned} \tag{2.3}$$

where $\langle ij \rangle$ and $\langle ij \rangle_3$ denote summation over nearest neighbor and third neighbor bonds, respectively [124, 167, 173, 156, 166]. K is the Kitaev interaction, Γ is the symmetric off-diagonal term and J, J_3 are the nearest-neighbor and third neighbor Heisenberg couplings, respectively. The γ_{ij} are bond labels (x, y, or z) as shown in Fig. 2.2(b) and α_{ij}, β_{ij} are the two remaining directions for each bond. Note that the magnetic field is expressed in spin-space components, for example, $H \parallel a$ is expressed as $H = H\,(1, 1, -2)/\sqrt{6}$ and $H \parallel b$ is $H = H\,(1, -1, 0)/\sqrt{2}$.

The parameters in Eq. (2.3) lead to a classical ground state with the observed zigzag antiferromagnetic order, pictured in Fig 2.1. We obtain the collective modes by expanding the Hamiltonian to quadratic order in the fluctuations about the ordered magnetic moment [62, 153, 38]. The spin wave theory is reliable when quantum (or thermal) fluctuations are small compared to the ordered moment, in which case the normal modes are non-interacting magnons. We obtain the theoretical THz absorption by computing the linear response of the magnons to an oscillating magnetic field. Beginning from the Hamiltonian in Eq. (2.3) of the main text, our spin wave approximation represents the dilute limit of magnon fluctuations above a classical spin configuration. Such an approximation is accomplished by rewriting the local longitudinal spin component as polarized minus a number operator. Consistency of the commutation relations of the spin variables and new bosonic variables fixes the rest of the dictionary:

$$S_i^z = S_0 - N_i = S_0 - a_i^\dagger a_i \tag{2.4}$$

$$S_i^- - = (2S_0)^{1/2} a_i^\dagger (1 - a_i^\dagger a_i/(2S_0))^{1/2} \approx (2S_0)^{1/2} a_i^\dagger \tag{2.5}$$

$$S_i^+ = (2S_0)^{1/2} (1 - a_i^\dagger a_i/(2S_0))^{1/2} a_i \approx (2S_0)^{1/2} a_i. \tag{2.6}$$

Here S_0 is the spin magnitude and the approximation in these equations are assumed in LSWT. These redefinitions are necessarily local when the magnetic order is not ferromagnetic. This technique is detailed in the more general case of incommensurate structures by Toth et al. [153]. The classical spin configuration is obtained by assuming a given zigzag order and minimizing the presented Hamiltonian. We then expand the Hamiltonian in our bosonic operators about this classical configuration. The accuracy of this approximation requires that the spin deviation remains small on the spin size.

Making these substitutions yields a bosonic theory with interactions, which we neglect, resulting in a quadratic theory. The quadratic Hamiltonian is not number conserving and can be solved with a Bogoliubov transformation using the technique of Colpa et al. [38]. The zero-point quantum fluctuations of the spins are captured in this approach and lead to reduction of the magnetic moment compared to its classical value. This reduction of static moment is the correction that we include when calculating the theoretical DC magnetic susceptibility (see Fig. 2.5) and it is important in not overestimating this quantity.

The dynamic structure factor is given by the two-spin correlation function which can be calculated with free field correlators in the bosonic language. This is related to absorption with linear response theory.

$$\begin{aligned}\int_{-\infty}^{\infty} e^{i\omega t}\sum_{i,j}(< S_i^{\mu}(t)S_j^{\nu} > + < S_i^{\nu}S_j^{\mu}(t) >) \\ \propto \coth\left(\frac{\beta\hbar\omega}{2}\right)\chi''_{\mu\nu}(\omega, Q=0)\end{aligned} \tag{2.7}$$

In the bosonic language this expression amounts to the evaluation of two- and four-point functions in a free theory. The transverse contributions are exclusively two-point functions and should therefore only be sensitive to, in this approximation, the one magnon spectrum. The longitudinal component of each spin contains a number operator so evaluating the longitudinal absorption involves a four-point function. A four-point function in free field theory splits into an integral over pairs (in our case with net momentum zero) and necessarily generates a continuum response. It is interesting that this continuum can generate contributions that look sharp enough in width to be confused with higher energy spin wave modes or other bound states.

For our Hamiltonian, the 1/S corrections to spin-wave theory are small but not insignificant. They are strongest at 0-field, and close to the ∼7 T transition. The 0-field corrections come from spin flip occupation at momentum given by the wave vectors of the unchosen zigzag orders. The zero field corrections are due to soft fluctuation modes at the right wave-vector that would take one zigzag configuration to one of the other two degenerate states. These corrections however should not couple strongly to the individual $Q = 0$ modes. Near the transition, the zero-point fluctuation (namely, the occupation of the Holstein-Primakoff bosons $n_k = a_k^{\dagger}a_k$) is almost exclusively at $Q = 0$ and we expect quantum corrections to our calculated spectra.

In the zigzag state, the unit cell of the honeycomb is enlarged to include four sites, as such there are four independent dispersing magnon modes. Of these, only two contribute to THz absorption, corresponding to the Ω_1 and Ω_2 modes discussed above. The two higher energy modes cannot be excited by the uniform in-plane THz field. This selection rule is exact, and is a result of a Z_2 symmetry of the zigzag state, whereby two pairs of spins within the unit cell may be exchanged. Thus, we do not associate the observed peaks at L_3 and L_4 with these modes.

We find the Hamiltonian enjoys two residual Z_2 symmetries even in presence of the zigzag order. The first is a sublattice symmetry. In a zigzag order the sublattice contains four spins, two on each ferromagnetic strip. The sublattice symmetry is a simultaneous switching of spins within each zigzag strip. This symmetry acts simply on the $Q = 0$ modes and they transform under representations of it. The higher energy modes are odd under this transformation and the lower energy modes are even. A uniform magnetic field is even under this transformation so it can only couple to the lower modes. This explains the absence of a response from the two higher spin wave modes. The second selection rule is the result of a spin-space symmetry of the zigzag state. This symmetry exchanges the two spin directions not associated with the bond that joins ferromagnetic strips. For instance, if the bond that joins the ferromagnetic strips is z-type, then at zero external field there is a symmetry upon the exchange of the x and y spin coordinates. This symmetry is approximate at finite field and exact for zero field. One of the lower modes, Ω_1 is odd under this transformation, while Ω_2 is even. The in-plane probe field, B_{THz}, if applied parallel or perpendicular to the ordering wave vector will be respectively odd or even under this transformation and couple to a mode of the same parity.

To find appropriate values for the parameters in Eq. 2.3, we began with the representative values chosen by Winter et al. [169, 166] to model INS data, and adjusted them to fit the energies of the modes seen by TDTS. We note that the parameters suggested by Ran et al. [123], obtained by fitting exclusively to INS spectra at the M point, yield spin wave energies at $Q = 0$ much larger than found experimentally. A linear spin wave calculation with the parameters of Winter et al. leads to an accidental degeneracy of modes Ω_1 and Ω_2. Refinement of these parameters is needed to account for our observation that these modes are split by 0.7 meV at $H = 0$. We find that fitting the spectra is accomplished by increasing the relative strength of the Γ term, such that $\Gamma/K \sim -1$ instead of $\Gamma/K = -1/2$. A representative fit to the energies of modes Ω_1 and Ω_2 as a function of H using the parameter set (J, K, Γ, J_3) = (-0.35, -2.8, 2.4, 0.34) meV is shown as dots in Fig. 2.3(f). We assume the same in-plane g-factor of 2.3 as used by Winter et al. [169, 166].

The calculated energies of the magnon modes are an excellent fit to the measured energies. Nevertheless, the parameters we have chosen should not be viewed as a definitive set representing microscopic interactions. As we show below, there are sizable quantum corrections to spin wave theory, which should be viewed as based on renormalized parameters. Such renormalized interactions may be dependent on magnetic field and the wave vector of the mode. In this context the main role of the LSWT analysis is to explain the origin of defining features of the spectra, such as spectral weight ratios, zero-field splittings, polarization selection rules, and trends with increasing applied magnetic field.

2.3.2 Low-Field Crossover

In the following we show that the polarization selection rules predicted by LSWT account for the intricate mode-switching behavior observed at intermediate magnetic fields, shown in Fig. 2.3 (a-d). The crossover at H =1.5 T coincides with the disappearance of magnetic Bragg peaks corresponding to one of the three possible orientations of zigzag order on the honeycomb lattice [136, 18]. Previously, this effect was interpreted assuming that three degenerate zigzag orientations are present as domains [136]. Within this picture, application of a magnetic field lifts the 3-fold degeneracy, driving energetically favored domains to grow at the expense of others. The possibility that the disappearance of magnetic Bragg peaks is related to a gradual reorientation of the ordered moments within domains was also discussed [18].

We find that a picture of gradual domain growth [136] or spin reorientation [18] is incompatible with the abrupt changes in the THz spectra that are observed when the applied magnetic field reaches 1.5 T. Instead, our explanation of the sudden changes at 1.5 T is based on the fact that in α-RuCl$_3$ the C_3 symmetry of the honeycomb lattice is broken, which removes the degeneracy of the three different possible orientations of the zigzag magnetic order. The dependence of the relative energy of the three orientations on H will lead to a field-induced level crossing in which the wavevector of the zigzag order will abruptly switch. In the following, we refer to this phenomenon as a "Q-flop" transition to distinguish it from the conventional spin-flop in which the spin direction changes but not the ordering wavevector. We believe that a Q-flop transition is required to account for the abrupt changes in the THz spectra and the vanishing of certain elastic neutron peaks near 1.5 T [136, 18]. Below, we discuss in detail how the Q-flop picture accounts for the unusual evolution of mode frequencies and spectral weights as a function of magnetic fields.

As mentioned previously, the breaking of C_3 occurs with a relatively small elongation of one of the three bond directions. We incorporate this distortion into the spin Hamiltonian by reducing the coupling constants J, K and Γ for the "stretched" bond. Breaking C_3 symmetry in this manner lifts the degeneracy between the three possible zigzag wave vectors, Q; the zigzag with Q parallel to

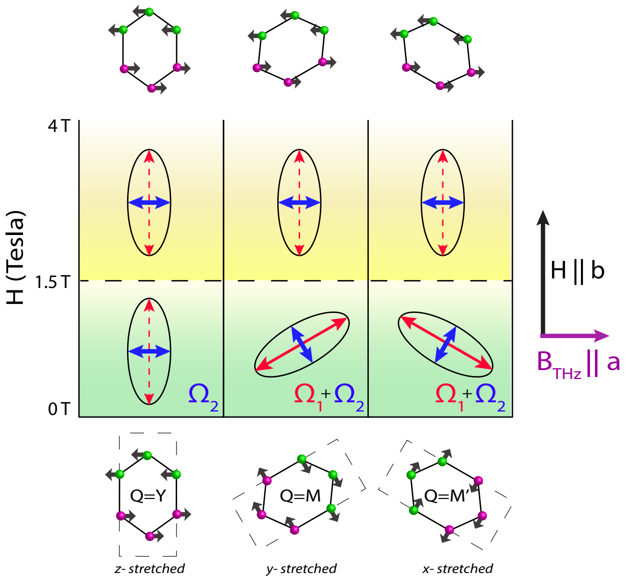

Figure 2.4: Illustration of the evolution of the three possible zigzag states and active modes for perpendicular case $H \parallel b$, $B_{THz} \parallel a$, where a, b are axes of the z-stretched domain. Bottom row of honeycombs shows preferred spin orientations at H = 0 T, with ordering wave vectors defined with respect to the z-stretched domain. The ellipses show the projection of polarization of Ω_1 (red) and Ω_2 (blue) onto the ac plane for each domain above and below $H_X = 1.5$ T. Solid arrows indicate a mode that absorbs for $B_{THz} \parallel a$, dashed arrows indicate a mode that does not absorb. Upper row of honeycombs shows reoriented spins above H_X.

the direction of its stretched bond (local monoclinic b axis) is energetically favored, the two other orientations of Q related by ±120° rotation are degenerate and higher in energy. This zero-field splitting plays a key role in shaping the field dependence of the THz spectra.

Our scenario for the evolution of the spectra with magnetic field is illustrated in Fig. 2.4, which presents a table of the energetically preferred states and active modes for each domain, for values of H below and above 1.5 T. We label each bond direction by x, y, or z, depending on the orientation of its Kitaev interaction. The hexagons with x, y, and z-stretched bonds shown in the bottom row of the table illustrate the spin order of the three domains at $H = 0$, where the spins are projected onto the ab plane. Our calculations show that application of a magnetic field favors zigzag orientations for which $|Q \cdot H|$ is largest. At a crossover field, H_X, the $Q \cdot H$ energy gain exceeds the zero-field splitting. For $H > H_X$ the zigzag wave vector in all domains aligns with the direction selected by the magnetic field, while structural domains remain intact. The field-induced crossover is illustrated in Fig. 2.4 for the case where the applied magnetic field favors the domain shown in the left-hand column, in which the z bonds are stretched. For $H > H_X$ the zigzag wave vector of the y and x domains will reorient to the Q of the z-stretched domain. This process is analogous to the usual spin-flop transition in antiferromagnets, with the distinction that here the rotation involves both the direction of the moments and wave vector of the magnetic order.

The Q-flop crossover described above accounts naturally for the complex evolution of the THz absorption with applied field when we take into account the polarization and relative spectral weight of Ω_1 and Ω_2. As illustrated by the arrows inside the ellipses in Fig. 2.4, for the preferred zigzag order of a z-stretched domain ($Q = Y$), Ω_1 is excited by $B_{THz} \parallel b$ and Ω_2 by $B_{THz} \parallel a$. The polarization of these modes reflects an approximate symmetry with respect to exchange of x and y spin coordinates within the zigzag state. This symmetry is exact at zero field. Furthermore, our LSWT calculations predict that the spectral weight of Ω_1 is approximately a factor of six larger than that of Ω_2 (as indicated by the eccentricity of the ellipses). Thus, LSWT predicts strong optical anisotropy for a single structural domain. The fact that the measured THz absorption is nearly isotropic in plane follows from the presence of the three structural domains with comparable, though unequal, population.

The state of the system for $H < H_X$ is indicated by the lower row of ellipses in Fig. 2.4. In this regime, for all directions of B_{THz} the spectrum is dominated by the strong Ω_1 mode at 2.6 meV, although Ω_2 at 3.3 meV appears faintly as well. The upper row of ellipses shows the reorientation of the polarization that accompanies the Q-flop crossover at H_X. With all the ellipses now aligned with the applied field, there is suddenly a strong dependence on the relative orientation of B_{THz} and H; $B_{THz} \parallel H$ couples only to Ω_1 while $B_{THz} \perp H$ couples only to Ω_2. This results in the mode-switching from Ω_1 to Ω_2 that is observed only in the $B_{THz} \perp H$ channel. Fig. 2.3 panels (e) and (f) show the evolution of the THz absorption spectra calculated with LSWT on the basis of the above model, which accurately reproduces the complex field and polarization dependent features of the experimental data.

In Fig. 2.5, we show that the multi-domain LSWT theory described above captures the curious deep minimum in spectral weight for $B_{THz} \perp H$ at 1.5 T (expressed as $\chi_\perp(0)$). The upper theoretical curve is the classical result, while the lower curve includes zero-point fluctuations of the spin 1/2 moments. The sudden reduction in spectral weight for $B_{THz} \perp H$ occurs when the applied field aligns the Q of each domain, such that at $H = H_X$, B_{THz} couples only to the weaker Ω_2 mode. Although the crossover predicted by the theory is sharp when compared with experiment, broadening of the Q-flop crossover is expected in the presence of structural disorder. We note that our scenario is consistent with the increase of the M point spin-wave intensity at 2 T observed in INS measurements [18].

2.3.3 Two-Magnon Contribution

Finally, we discuss the features L_3 and L_4 that are observed in the $B_{THz} \perp H$ channel in the photon energy range $\sim 4-6$ meV (Fig. 2.3 panels (b) and (d)). These modes cannot be identified as single magnon excitations because of the exact Z_2 symmetry discussed above. However, LSWT predicts absorption by a continuum of two-magnon states in precisely this energy range (Fig. 2.3(f)). A further prediction is that the two-magnon absorption takes place selectively for B_{THz} parallel to the ordered moment. As shown in Fig. 2.4, for $H > H_X$ the moments have flopped to an orientation that is nearly perpendicular to H. Thus, the two-magnon interpretation of L_3 and L_4 is consistent with the selection rule seen in the data, as these features appear for $B_{THz} \perp H$ and are unobservable for $B_{THz} \parallel H$.

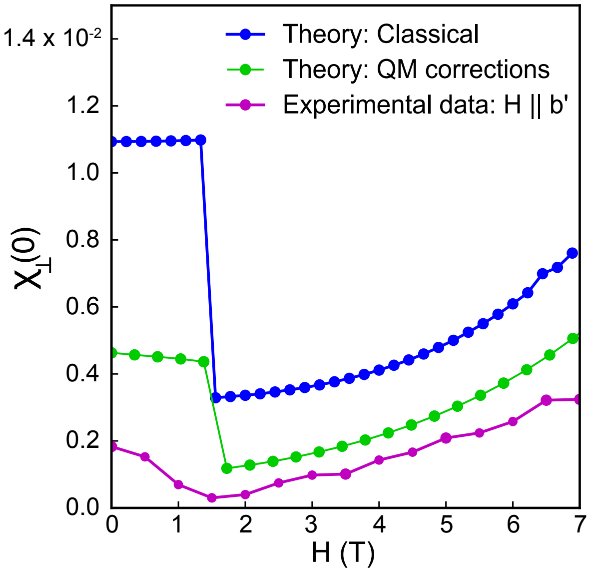

Figure 2.5: Experimental and theoretical $\chi(0)$ as a function of $H \parallel b \perp B_{THz}$ configuration. Blue: Susceptibility of the classical spin configuration. Green: Calculation of susceptibility with corrections. Magenta: Experimental values.

Although the selection rules show unambiguously that L_3 and L_4 are two-magnon excitations, the details of the calculated field dependence (Fig. 2.3(f)) differ from the data. This is in contrast to the excellent agreement in the case of the single-magnon modes Ω_1 and Ω_2. The most likely origin of this discrepancy is that while the single magnon modes are measured at $Q = 0$ the two-magnon absorption depends on the spin wave dispersion over the entire Brillouin zone. While our LSWT parameters reproduce the local minima at the M-points seen by INS, they do not reproduce the local minimum observed also at the Γ-point [18]. Indeed, all the theoretical models of this system studied to date do not reproduce this feature of the INS data [169, 148]. The dispersion of the modes across the Brillouin zone for our LSWT model, at $H = 2$ T, is shown in Fig. 2.6, where local minima appear at the M-points but not the Γ-point. We find that a local minimum at the Γ-point may be introduced by adding a second nearest neighbor ferromagnetic Heisenberg term on bonds perpendicular to the order wave vector on the order of .3 mev. Anisotropic second neighbor terms of this order and larger are predicted by ab initio studies [167]. Including such terms has the additional benefit of increasing the M-point gap closer to observed values. We would like to emphasize that in modeling the full dispersion, such terms shouldn't be ignored due to their small magnitude because for each site, there are six second neighbor couplings. Further study is required to fit such terms to experimental data. However, we find that a Γ-point minimum appears within LSWT when further interactions are added, for example second nearest-neighbor ferromagnetic coupling. Finding a spin Hamiltonian that describes all aspects of the single-magnon, two-magnon, and INS spectra is a goal for future research.

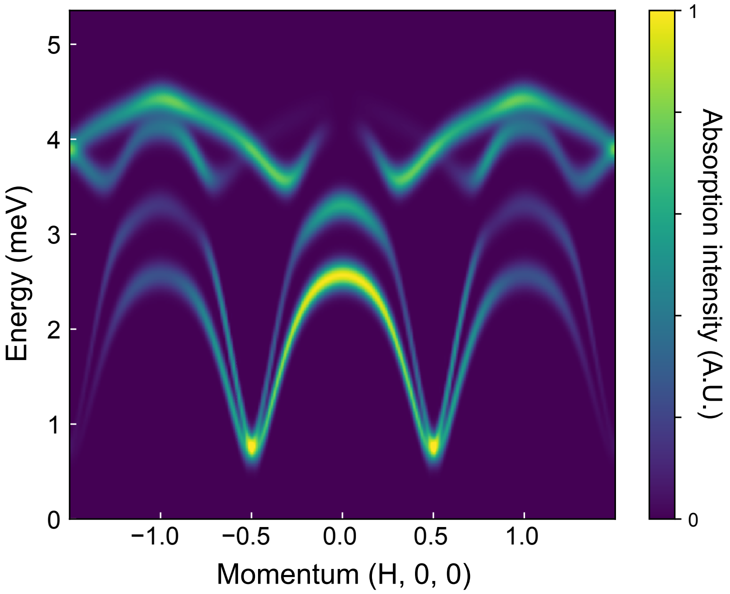

Figure 2.6: Theoretical spinwave dispersion at $H = 2$ T applied along the b-axis.

2.4 Discussion

In summary, we used polarized time-domain THz spectroscopy to track the frequencies and spectral weights of optically accessible magnetic excitations in α-RuCl$_3$ approaching the ~7.5 T transition to a spin disordered state. The THz spectra were determined for parallel and perpendicular orientation of the static and THz magnetic fields. We observed two sharp resonances at 2.5 and 3.2 meV and broader features in the range 4-6 meV that appear only at applied fields of above approximately 4 T. In the theoretical section of the paper, we showed that linear spin wave theory can account for the totality of the data, *i.e*, the field dependence of spectral weights, mode frequencies, and polarization selection rules. The two lower frequency peaks are attributed to zero-wavevector magnons and the higher energy features that appear at approximately 4 T are consistent with a continuum of two-magnon excitations.

In our analysis, we focused on the unusual field dependence observed with H perpendicular to B_{THz}, where an apparent jump in spin wave frequency from 2.5 to 3.2 meV and a deep, narrow minimum in spectral weight occur at an applied field of 1.5 T. We showed these phenomena arise from the combination of two factors. First the C_3 symmetry of a perfect honeycomb is broken in the α-RuCl$_3$ lattice, which gives rise to the presence of three structural domains. Second, the frequencies of the two optically active spin waves are split even in zero applied magnetic field; the degeneracy of these modes seen in previous spin-wave calculations [169, 166] is an artifact of the parameters used in those models. Based on these factors, we conclude that the apparent jump in frequency and spectral weight minimum arise from a Q-flop crossover at 1.5 T, where the external field overcomes the anisotropy of the crystal to select a preferred ordering wave vector of the zigzag state. Although the mode jump was previously associated with Dzayaloshinskii-Moriya (DM) interaction [121], or to a sudden splitting of modes caused by the applied magnetic field [140], we believe that our model based on zero-field splitting and field-induced ground state energy crossing is uniquely able to account for the totality of the data. The constraints on the effective spin Hamiltonian parameters that emerge from our analysis will aid in understanding the phase diagram of α-RuCl$_3$ and potential for existence of spin liquid ground states in this fascinating compound.

Chapter 3

Theory of Z_2 Flux Binding to Lattice Vacancies in Kitaev Spin Liquids

3.1 Introduction

Anyons are particles with nontrivial braiding statistics that can emerge as excitations in phases of matter with topological order in two spatial dimensions [145, 161]. The experimental realization and detection of anyons in concrete physical systems has long been an important goal. Only recently this has been achieved in fractional quantum Hall systems using mesoscopic interference experiments [105].

Quantum spin liquids, discussed in some length in the introduction section, can also host anyon excitations. However, it is an open problem how to controllably create and detect anyonic excitations in this case. Even experimental identification of a spin liquid is an unrealized goal, in part because it is hard to come up with positive signatures of a spin liquid. Finding concrete schemes for creating and detecting topological excitations of spin liquids is a promising approach to obtain unique signatures of such phases. To this end, solvable models of spin liquids, such as Kitaev's honeycomb model, offer a useful laboratory for studying manipulation and detection of anyons.

Kitaev's Honeycomb model is a solvable spin model with a Z_2 spin liquid ground state. The excitations include propagating Dirac-Majorana fermions and static gapped Z_2 fluxes that act as a source of π-flux for the fermions. With addition of time-reversal symmetry breaking terms, Kitaev's honeycomb model can also realize a non-abelian spin liquid, hosting non-abelian anyon excitations. The model, its solution and basic properties are reviewed in the introduction.

An interesting property of the Kitaev honeycomb model for the purpose of preparing and manipulating anyons is that lattice vacancies tend to bind a flux of the Z_2 gauge field [164, 70, 56]. In the non-abelian phase the vacancy traps a non-abelian anyon, at least if the gap is not too big [70]. A natural question is whether these results, obtained via exact solution of the honeycomb model represent more general properties of Z_2 spin liquids and proximate non-abelian phases.

In this chapter we identify a robust mechanism for trapping of Z_2 fluxes by lattice vacancies. Our analysis is based on the universal low-energy theory of the spin liquid and a proximate non-abelian chiral spin liquid.

In section II we investigate the effect of lattice vacancies on the ground state of a Z_2 Dirac

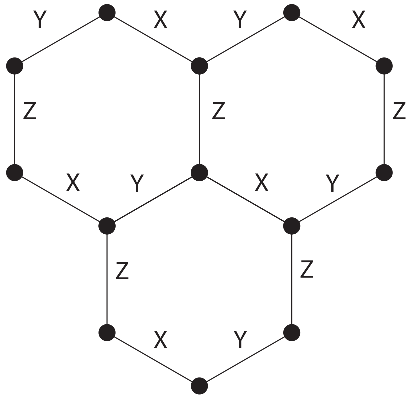

Figure 3.1: In the Kitaev honeycomb model, nearest neighbor spins couple with Ising interactions whose spin component depends on the direction of the connecting bond.

spin liquid by treating them as scattering centers. We show that a vacancy produces a scattering resonance unless it is accompanied by a Z_2 (i.e. π) flux. The presence of the scattering resonance involves transfer of spectral weight from large negative energies to a peak at zero energy which implies an increase of the ground state energy. Thus, the suppression of the scattering resonance by the Z_2 flux explains the binding energy.

In section III we show that the flux binding has a topological origin by formulating a pumping argument. To this end we weakly break time-reversal symmetry to open a small gap in the Dirac dispersion, which takes the system slightly into a non-abelian spin liquid phase. Threading a Z_2 flux adiabatically through the vacancy then reduces the energy through spectral flow.

3.2 Flux Trapping From Low-Energy Scattering Theory

3.2.1 The Low-Energy Effective Theory

The low-energy theory of a Z_2 spin liquid can be motivated and derived starting from the solution of Kitaev's honeycomb model, but is more general. Kitaev's model is reviewed in the introduction, and we give it here for convenience:

$$H = -\sum_{<j,k>_\gamma} J^\gamma \sigma_j^\gamma \sigma_k^\gamma \quad \gamma \in \{x, y, z\}. \tag{3.1}$$

Where the spin-1/2 moments are located on the honeycomb lattice and interact via bond-dependant Ising interactions as shown in Fig. 3.1. We will focus on the isotropic point where all couplings J^γ are approximately equal. As shown in the introduction the exact solution of this model involves rewriting spin operators using four Majorana operators $\sigma_j^\gamma = i b_j^\gamma c_j$ supplemented by a local parity constraint. The model is then given as a Hamiltonian of Majorana fermions coupled to Z_2 gauge degree of freedom on the links and the ground state can be shown to be in the sector with no Z_2 flux through plaquettes. In the zero flux configuration, the fermions have two conical crossings of zero-energy leading to a Dirac dispersion at low-energies [78]. In Kitaev's model the Z_2 gauge field fluctuations are completely static, so the physics is described by non-interacting fermions for any given flux configuration. More generally the fluxes can gain dynamics, but they represent gapped degrees of freedom. Integrating out the gapped gauge field fluctuations leads to interaction terms between the Majorana fermions that are irrelevant at low energies. In what follows we will allow for bound Z_2 flux excitations that act as a source of π-flux for the Majorana fermions.

The discreteness of Z_2 fluxes presents a challenge for writing a long wavelength continuum field theory of the Majorana fermions that couple to them. First, a Z_2 flux can only be implemented using a singular vector potential as illustrated in Fig. 3.2. Second, it is often useful to introduce a perturbation adiabatically and this is impossible to do with a flux of a Z_2 gauge field because of its discreteness. We resolve both these issues by formally doubling the problem. By taking two uncoupled layers of the spin liquid the Majorana fermions can be replaced with complex fermions $a = c_1 + ic_2$ that can couple to a static U(1) gauge field. The resulting model is equivalent to the original (doubled) Majorana model as long as all physical configurations of the $U(1)$ gauge field include only zero or π fluxes threading plaquettes. However, the $U(1)$ gauge freedom allows us to represent these configurations vector potential field that is smooth everywhere except at the origin and can be included in a continuum field theory. Furthermore, we can study the change between a configuration with zero flux threading a plaquette to one with a Z_2 flux by adiabatically increasing the flux from zero to π.

The low-energy Dirac theory coupled to the $U(1)$ vector potential is given by

$$H = \int d^2x(\psi_K^\dagger \vec{\sigma} \cdot (\vec{p} - \vec{A})\psi_K + \psi_{K'}^\dagger \vec{\sigma}^* \cdot (\vec{p} - \vec{A})\psi_{K'}), \quad \vec{A} = \Phi \frac{\hat{\theta}}{r}. \tag{3.2}$$

Here $\psi_K^\dagger$ and $\psi_{K'}^\dagger$ are each two component spinors in the sublattice degree of freedom and σ^α are Pauli matrices in this space. The labels K and K' represent the two valleys of the Dirac dispersion. A convenient gauge to describe an Aharonov-Bohm flux Φ at the origin has $\vec{A} = \Phi\, \hat{z} \times \hat{r}/r$.

As in graphene, the Dirac fermions are protected by particle-hole symmetry and time-reversal symmetry. In this case because the model must describe two decoupled Majorana-Dirac models, the particle-hole symmetry cannot be broken by any physical perturbation. Therefore, only time-reversal symmetry breaking can generate a gap. In section III we show that under the presence of weak time-reversal symmetry breaking the conclusions of this section are not changed.

A lattice vacancy can be described as a special impurity potential within the effective continuum theory. First, we note that it prevents occupation of a specific lattice site belonging to one sub-lattice, say sublattice A. Therefore, it acts as a local infinite repulsive potential for only one pseudo-spin σ component. Second, because the potential it produces the same inter-valley as intra-valley coupling. These two observations imply the following potential to represent a vacancy at the origin:

$$U(r) = u\, \delta(r)\psi^\dagger(1 + \sigma^z)(1 + \tau^x)\psi, \tag{3.3}$$

where σ and τ are Pauli matrices that act on the sublattice and valley degrees of freedom respectively. We always need to take the limit $u \to \infty$ at the end of the calculation to represent a physical vacancy.

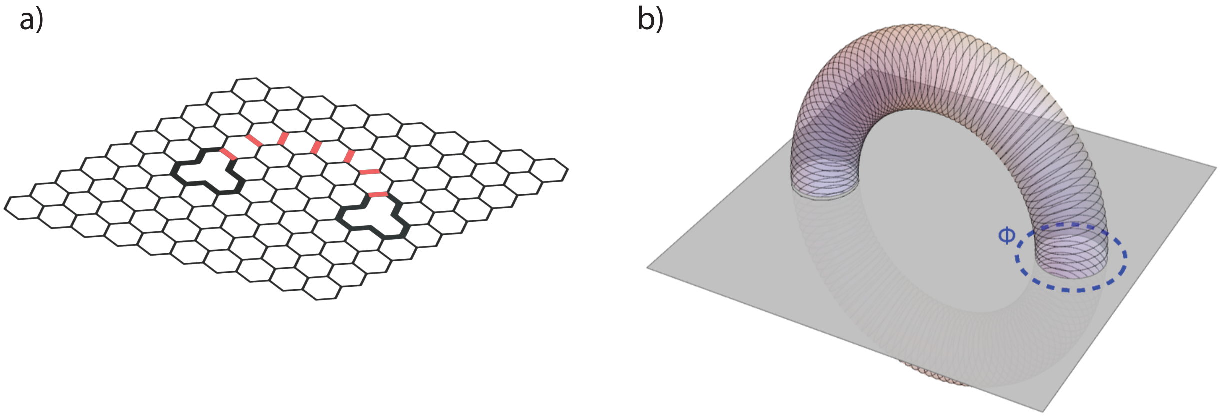

Figure 3.2: (a) A lattice vacancy changes the ground state flux configuration by binding a Z_2 flux in the honeycomb Kitaev spin liquid. The red lines represent singular vector potential connecting the fluxes, passing over which fermions acquire a minus sign. (b) We describe the effect of Z_2 fluxes within a continuum low-energy theory where fluxes are represented as smooth Aharonov-Bohm fields. In the double layer system, these can contain arbitrary flux Φ.

3.2.2 General Argument Using Friedel Sum Rule

In this section we use a Friedel sum rule to argue that a lattice vacancy gives rise to a scattering resonance, whereas the presence of a Z_2 flux near the vacancy suppresses the resonance. As explained above, suppression of the resonance involves transfer of spectral weight from the zero-energy peak to large negative energies, reducing the ground state energy.

Friedel's sum rule relates the charge that is removed from the system by an impurity potential to the scattering phase shift at zero energy. For a short-range potential Friedel's sum rule is given by [50]:

$$\Delta N = \frac{1}{\pi}\eta(0). \tag{3.4}$$

In this expression $\eta(E)$ is the scattering phase shift and it assumes that the scattering phase shift vanishes at energies of the order of the cutoff. In our case the particle-hole symmetry of the Dirac fermions ensures that creating a lattice vacancy corresponds to removing (or adding) half-charge from the system, i.e. $\Delta N = \pm 1/2$. Hence, by the Friedel sum rule, the zero-energy scattering phase shift is $\eta(0) = \pm\frac{\pi}{2}$. Recall that the scattering cross section depends on the phase shift as $\sin^2(\eta)$. A phase shift of $\pi/2$ corresponds to the unitarity limit [61]. By the Breit-Wigner[26] formula a scattering phase shift $\pi/2$ implies that the cross section and the density of states form a peak at zero energy corresponding to a resonance. This is familiar in tight-binding models of graphene, where a quasilocalized zero-energy mode is known to appear created by a lattice vacancy [20] and earlier from the resonant-level model [8, 42]. The appearance of a resonance incurs an energy cost. Due to particle-hole symmetry, the spectral weight associated with the zero-energy resonance must be taken from both positive and negative energies. As the ground state energy is the sum over all negative energy states, the transfer of states from negative to zero energy increases the ground state energy.

The Friedel sum rule shows us that the scattering phase shift at zero energy is $\eta(0) = \pi/2$. The scattering cross section depends on $\sin^2(\eta)$ and therefore the zero-energy scattering has reached the unitary limit [61]. By the Breit-Wigner formula a scattering phase shift $\pi/2$ implies that the cross section forms a peak - corresponding to a metastable bound state also called a resonance [26]. This is familiar in tight-binding models of graphene. On a finite lattice this appears as a quasilocalized zero-energy mode created by a lattice vacancy [119]. The creation of a lattice vacancy in any bipartite hopping model imbalances the number of sublattice sites and guarantees the appearance of a zero-energy eigenstate. In an infinite system this mode isn't normalizable, and therefore appears through a resonance of the scattering states [119]. We have thus shown that lattice vacancies induce a zero-energy scattering resonance [46, 119]. Due to particle-hole symmetry, the spectral weight associated with this zero-energy resonance must be drawn from negative energies. As the ground state energy is the sum over all negative energy states, this must increase the ground state energy.

Next, we seek to use a Friedel sum rule to compare the scattering phase shift when a Z_2 flux is threaded through a vacancy, however the previous Friedel sum rule only worked for short-ranged potentials. To remedy this we consider a more general Friedel sum rule. We begin by calculating the change in particle number ΔN as a result of a perturbation:

$$\begin{aligned}\Delta N &= \int_{-\Lambda}^{0} \Delta\rho(E) dE \\ &= -\frac{1}{\pi}\int_{-\Lambda}^{0} \operatorname{Im}(\operatorname{Tr}(G(E) - G^0(E)))dE \\ &= \frac{1}{\pi}\int_{-\Lambda}^{0} \partial_E \operatorname{Im}(\ln\det(T(E)))dE \\ &= \frac{1}{\pi}(\eta(0) - \eta(-\Lambda)),\end{aligned} \tag{3.5}$$

Here $\rho(E) = -\frac{1}{\pi}\operatorname{Im}\operatorname{Tr}G(E)$ is the density of states, and Λ is the cutoff of the system. In this expression $G^0(E)$ and $G(E)$ are the Green's functions before and after the perturbation is introduced and the T matrix is defined by the relation $G(E) = G^0(E) + G^0(E)T(E)G^0(E)$. We have utilized the Green's function identity $\operatorname{Tr}(G(E) - G^0(E)) = \partial_E \ln\det T(E)$ [61]. Now fixing $\Delta N = -1/2$ we obtain the general Friedel sum rule for vacancies which can accommodate long-range potentials:

$$\eta(0) - \eta(-\Lambda) = -\pi/2. \tag{3.6}$$

The only difference between this Friedel sum rule and the one given previously is the appearance of a scattering phase shift at the cutoff energy. However, in the absence of long-range potentials like an Aharonov-Bohm field, we can take $\eta(-\Lambda) \equiv 0 \mod \pi$, physically stating that at sufficiently high energies the quasiparticles are essentially free [93].

Next, we apply this Friedel sum rule to calculate the zero-energy phase shift of a vacancy threaded with flux Φ, $0 < \Phi < 1$. For this case we can no longer safely assume that $\eta(-\Lambda) \equiv 0$ mod π. This is because even at the highest energies, in an Aharonov-Bohm field, encircling the origin imparts a phase. However, we can provide a quick heuristic derivation of this phase shift and we will verify the resulting predictions in the next section. In the presence of an Aharonov-Bohm potential, all particles acquire an additional angular momenta Φ. At asymptotically large distances, this leads to the simple change of outgoing and ingoing radial waves being multiplied by a phase $\propto e^{\pm i(\pi\Phi/2)}$. This is true in both the Schrödinger equation [3, 129] and for the components of the Dirac equation [54, 126]. In the Schrödinger equation this leads to energy-independent scattering phase shifts in all partial waves $\eta_l(E) = -\frac{\pi}{2}(|l+\Phi|-|l|) = \pm\frac{\pi}{2}\Phi$, where the sign comes from whether the effective angular momentum $l+\Phi$ is positive or negative [3, 129]. In the Dirac equation, the scattering phase shifts approach this at large energies [54, 126]. We assume that this holds for our low-energy theory and evaluate $\eta(-\Lambda)$ by summing over all angular momentum l and valley v contributions:

$$\eta(-\Lambda) = \sum_{l,v} \eta_{l,v}(E) = -\pi\Phi(1-\Phi). \tag{3.7}$$

This sum requires analytic continuation and has been performed before in the context of Friedel sum rules in the presence of Aharonov-Bohm fields [103]. The result is proportional to the correction of the ideal gas law for anyons [39]. There it corresponds to an anyonic exclusion pressure. Rearranging Eq. (3.6) we obtain the Friedel sum rule for vacancies threaded with flux:

$$\eta(0) \equiv \pi(1/2 - \Phi(1-\Phi)) \mod \pi. \tag{3.8}$$

We note that the scattering amplitude $\sin^2(\eta(0))$ is minimized for $\Phi = 1/2$, or in other words, for a Z_2 flux. Additionally, this scattering cross section is reduced by a factor of one-half relative to vacancy-only scattering. We have thus shown that by threading a Z_2 flux reduces scattering peak at zero-energies due to a lattice vacancy.

The fact that a Z_2 flux maximally suppresses the scattering resonance from a lattice vacancy suggests that the binding energy for the pair arises from this effect. As the resonance is suppressed, spectral weight must be transferred back to larger negative energies which should make the ground state energy lower. However, it is unclear if other effects compete with this, and we must verify that this doesn't happen with a direct solution of the scattering theory.

3.2.3 Solution of Scattering Problem

In this subsection we will solve the scattering theory of the Dirac fermions perturbed by vacancies and fluxes. To corroborate the Friedel sum rule's result, we will explicitly show how spectral weight transfers from the zero-energy resonance to the cutoff scale as a result of threading flux and that no competing effects occur.

To show the transfer of spectral weight, we need to calculate the shift in density of states induced by a lattice vacancy with and without a Z_2 flux. To do this we will calculate the Green's functions of the Dirac fermions with a vacancy and with a vacancy threaded by flux. We accomplish this in three steps: first, we solve the non-interacting Dirac equation with and without Z_2 fluxes, second, we use these solutions to calculate "free" Green's functions G^0, and finally, we use an exact expression for the T matrix of a vacancy to calculate the "final" Green's functions G from the free Green's functions. With these final Green's functions in hand, we compare the shift in density of states between the two cases. Then, we use these density of states to evaluate the binding energy of a Z_2 flux and a lattice vacancy.

The single particle Dirac Hamiltonian in the Aharonov-Bohm field can be solved directly[126, 54]. The problem is greatly simplified by using the conservation of the z component of angular momentum $J_z = L_z \pm \frac{1}{2}\sigma^z$ in valleys K' and K respectively. The Aharonov-Bohm fields do not spoil this conservation because they are rotationally invariant. We can now reduce the Dirac equations to a one-dimensional radial equation for the four components of the spinor by using the ansatz:

$$\psi(r,\theta) = \begin{bmatrix} \psi_A^K(r,\theta) \\ \psi_B^K(r,\theta) \\ \psi_A^{K'}(r,\theta) \\ \psi_B^{K'}(r,\theta) \end{bmatrix} = \begin{bmatrix} \psi_A^K(r)e^{i(j+1/2)\theta} \\ \psi_B^K(r)e^{i(j-1/2)\theta} \\ \psi_A^{K'}(r)e^{i(j'-1/2)\theta} \\ \psi_B^{K'}(r)e^{i(j'+1/2)\theta} \end{bmatrix}, \tag{3.9}$$

where j, j' are the half-integral total angular momentum quantum numbers of the valleys K and K'. Using the above ansatz leads to the following radial equations in each valley:

$$\begin{bmatrix} 0 & (\mp\partial_r + \frac{j\mp 1/2-\Phi}{r}) \\ (\pm\partial_r + \frac{j\pm 1/2-\Phi}{r}) & 0 \end{bmatrix} \begin{bmatrix} \psi_A^{K/K'}(r) \\ \psi_B^{K/K'}(r) \end{bmatrix} = E \begin{bmatrix} \psi_A^{K/K'}(r) \\ \psi_B^{K/K'}(r) \end{bmatrix}. \tag{3.10}$$

The solutions of these equations are given by Bessel functions of order $j' \pm 1/2 - \Phi$. Intuitively, this is telling us that a flux shifts the effective angular momentum of all particles in its presence by Φ. Despite the appearance of uncoupled equations in the valleys, a crucial element of this calculation is a boundary condition that forces a relationship between the valleys at non-zero Φ. For $\Phi = 1/2$ this condition is:

$$\begin{aligned} &\lim_{r\to 0}(r^{1/2}\psi_A^K(r) = r^{1/2}\psi_A^{K'}(r)), \\ &\lim_{r\to 0}(r^{1/2}\psi_B^K(r) = r^{1/2}\psi_B^{K'}(r)). \end{aligned} \tag{3.11}$$

When a Dirac fermion is coupled to a flux, a boundary condition must be added to ensure that the Hamiltonian remains well-defined [54, 126]. In the case of multiple Dirac fermions the valley fermions can be related by this boundary condition [127]. In this appendix we derive the boundary condition presented. From Eq. (3.11) we notice that for any wavefunction which is less singular than $r^{-1/2}$ near the origin that the condition is trivial. Therefore, most states are not impacted by this condition. Looking forward to the next section, this boundary condition is important as it results in a single bound zero-mode appearing with a Z_2 flux when time-reversal symmetry is broken.

After solving the radial equations, we can sum over all eigenstates to calculate the free Green's functions with and without a Z_2 flux:

$$G^0(r,r',E) = \sum_{\gamma\in\{\pm\}} \int d^2k \sum_{j,j'} \frac{\psi_{j,j',\gamma E(k)}(r)\psi^\dagger_{j,j',\gamma E(k)}(r')}{z-\gamma E(k)}. \tag{3.12}$$

In this expression we sum over particle/hole branches γ and angular momenta j and j'. The Green's functions for $\Phi = 0$ and $\Phi = 1/2$ are calculated in the supplemental material. For $\Phi = 0$, the diagonal Green's function is given by:

$$G^0(r,r;E)_{\alpha\beta,\alpha\beta} = \frac{E}{4\pi}\ln\left(\frac{E^2}{E^2-\Lambda^2}\right). \tag{3.13}$$

Here $\alpha = A, B$ is the sublattice index and $\beta = K, K'$ is the valley index. All diagonal elements of the Green's functions are the same. For $\Phi = 1/2$, the diagonal Green's function close to the origin is dominated by a divergent contribution:

$$G^0(r, r; E)_{\alpha\beta,\alpha\beta} \approx -i\frac{e^{2irz}}{2\pi r}. \tag{3.14}$$

Far from the origin it approaches the $\Phi = 0$ case's Green's function.

Now, we find the exact expression for the T matrix of a vacancy [92, 46, 61]. For the lattice vacancy potential Eq. (3.3), denoted here as U, the T matrix is given by a geometric sum that we can evaluate directly:

$$\begin{aligned} T(E) &= (1 + 4uG^0(r_v, r_v, E)_{+x,A;+x,A} + (G^0(r_v, r_v, E)_{+x,A;+x,A})^2 + \ldots)U \\ &= (1 - 4uG^0(r_v, r_v; E)_{+x,A;+x,A})^{-1}U \\ \lim_{u\to\infty} T(E) &= -\delta(r - r_v)(G^0(r_v, r_v; E)_{+x,A;+x,A})^{-1}\frac{(1+\sigma^z)}{2}\frac{(1+\tau^x)}{2}. \end{aligned} \tag{3.15}$$

Here we have indicated that the Green's function is taken from the A sublattice and valley-even $(+x)$ component. $r_v = 0$ is the location of the vacancy.

We can calculate the Green's function corresponding to a system with a vacancy by applying the T matrix to the free Green's function. This is accomplished using the relationship $G = G^0 + G^0TG^0$. Taking the imaginary part of these Green's functions we get the density of states. With some simplifying Green's function identities we can evaluate the total shift in density of states (see appendix)[61]:

$$\Delta\rho(E) = \partial_E \mathrm{Arg}\frac{1}{G^0(r_v, r_v, E)_{+x,A;+x,A}}. \tag{3.16}$$

Therefore, given our free Green's functions G^0, we can quickly calculate the shift in density of states due to the vacancy. By looking at the Green's functions rate of change of phase we can anticipate the results. For $\Phi = 0$, the Green's function (Eq. (3.13)) at zero energy changes sign. This corresponds to an abrupt phase shift of Π which via Eq. (3.16) will lead to a delta function peak at the origin. This is our predicted resonance. For $\Phi = 1/2$, we note that the phase of the Green's function (Eq. (3.14)) near zero-energy is constant. Therefore, a lattice vacancy does not induce more shifts in density of states when a flux is present.

First, we consider the case of introducing a vacancy without flux. We find that the scattering resonance well known from graphene appears [119, 46]. The total shift in density of states is well-approximated by:

$$\Delta_v\rho(E) \approx \delta(E) - (\delta(E - \Lambda) + \delta(E + \Lambda)), \tag{3.17}$$

with corrections that vanish under integration for large Λ. We find that the dominant scattering physics corresponds to the creation of a zero-energy scattering resonance and that this spectral weight almost all comes from the cutoff energy (see Fig. 3.3(a)). This directly implies that the ground state energy increases as a result of the vacancy.

Second, we compare the case of a vacancy with flux threaded through it. We anticipate from the Friedel sum rule that a Z_2 flux will suppress the scattering peak at zero-energy. Utilizing Eq. (3.16) we find that the shift in density of states is well-approximated by:

$$\Delta_{v\Phi}\rho(E) \approx \frac{1}{2}\delta(E) - \frac{3}{4}(\delta(E + \Lambda) + \delta(E - \Lambda)), \tag{3.18}$$

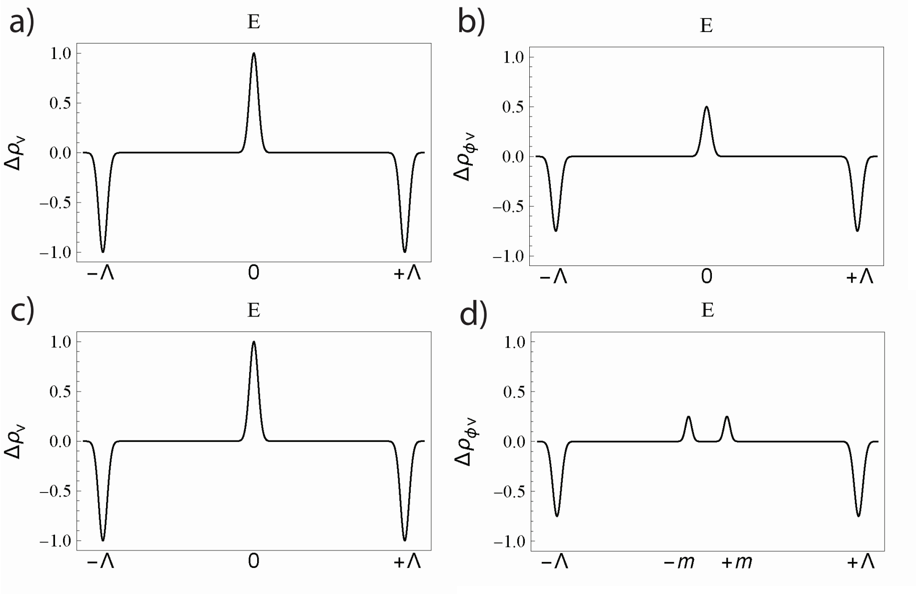

Figure 3.3: (a) A lattice vacancy generates a resonance at zero-energy. The y-axis represents the shift in density in units of delta functions. Half-filling necessitates that spectral weight is drawn from large energies and thereby increases the ground state energy. (b) When a flux is threaded through the vacancy the resonance is partially suppressed and the spectral weight is returned to high energies, thereby generating a binding energy for the flux-vacancy pair. (c) The response to a vacancy is unchanged in the presence of time-reversal symmetry breaking (d) When a flux is threaded through the vacancy in the presence of time-reversal symmetry breaking the zero-energy peak is split between $E = \pm m$.

in the large Λ limit. We note that the zero-energy resonance induced by a vacancy now has reduced in magnitude by half (compare panels (a) and (b) in Fig. 3.3). We see from the solution to the scattering theory that this spectral weight returns directly to the cutoff scale.

From the shift of the density of states induced by a vacancy, both with and without a flux bound to it, we can calculate the respective change to the ground state energy. Specifically, the binding energy of a π-flux to the vacancy is

$$E_{v\Phi} - E_v = -\frac{\Lambda}{4}. \tag{3.19}$$

This binding energy originates from pushing half of the resonance's spectral weight from zero energy back to the cutoff scale.

3.3 Topological Argument for Flux Binding by Vacancies

In this section we will show that in presence of a weak time-reversal breaking field which introduces a gap to the Majorana dispersion, the binding energy of a flux to a vacancy can be derived from a topological argument. Furthermore, we will argue that the binding energy is in general not dependent on the strength of the time-reversal breaking field in the limit of small field. Hence, the argument we develop can also be used to explain the flux binding in the gapless phase, which was explained in the previous section using a different approach (scattering theory).

In presence of a time reversal breaking field the gapless Kitaev spin liquid becomes a gapped non-abelian state in which Z_2 fluxes become Ising anyons [78]. Therefore, our argument will also establish that in the non-abelian state, at least with moderate time-reversal breaking field, lattice vacancies naturally bind Ising anyons.

Like in the previous section, we will double the effective theory of the spin liquid, written in terms of free Majorana fermions, to a theory of (complex) Dirac fermions, which can couple to an external $U(1)$ flux. Our argument will rely on tracking the evolution of the ground state energy upon adiabatic flux insertion into the hole associated with the vacancy. The essence of the argument uses the fact that in presence of time-reversal breaking field the Dirac theory (i.e. doubled Majorana model) is in a quantum Hall state [1]. As in Laughlin's well-known argument, adiabatically threading flux pumps charge away from the vacancy toward the bulk [85]. The zero mode that carried this charge moves to negative energy, thereby lowering the ground state energy.

To establish this phenomenon carefully, we examine a Corbino disc geometry centered on the vacancy (see Fig. 3.4(a)). In what follows we will consider the anomalous edge theory living on the inner and outer boundaries of the Corbino disc. To facilitate a low-energy theory, we enlarge the hole so that instead of a single vacancy it consists of a cluster of $2N + 1$ vacancies. We will ask whether this larger cluster of vacancies traps a Z_2 flux (half a flux quantum, $\Phi = 1/2$). Note that by the Friedel sum rule argument given in the previous section, an odd number of vacancies gives rise to a resonance and hence at least one zero mode.

When we turn on a time-reversal breaking field, the bulk forms a gapped quantum Hall state, while the zero mode in the hole becomes one mode of the chiral edge state on its perimeter [78]. More precisely, the chiral edge state disperses linearly with the discrete angular momentum around the hole and includes a mode at exactly zero energy:

$$H = -v_E \sum_k (k - k_0)(\psi(k)^\dagger \psi(k)). \tag{3.20}$$

Here v_E is the edge velocity, $k = \frac{2\pi n}{L}$ with n an integer. k_0 is the zero-intercept of the dispersion. The sign of v_E (direction of the chiral edge state) depends on the direction of the time-reversal symmetry breaking field. For convenience we will assume $v_E > 0$. There is also an edge state located on the outer edge of the Corbino disk with perimeter $L_o \gg L$. This state has the opposite chirality of the inner edge state (opposite sign velocity). Adiabatic threading of a flux Φ (in units of the flux quantum) through the hole leads to transport of the angular momentum states from n to $n + \Phi$.

---

[1] Microscopically the doubled model with time-reversal breaking field is the same as the Haldane model [57].

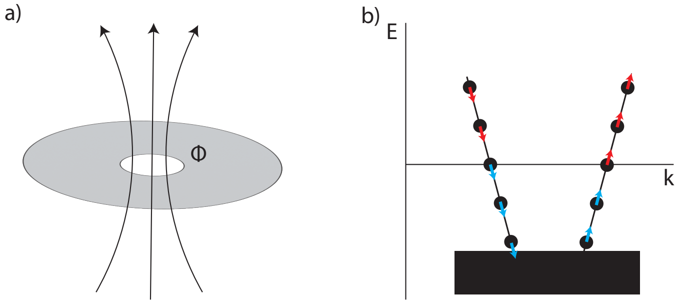

Figure 3.4: (a) The annulus geometry used for the flux pumping argument. The interior boundary is formed from a cluster of $2N+1$ vacancies and flux Φ is adiabatically threaded through it. (b) The edge spectrum's spectral flow is indicated with arrows. Blue arrows correspond to states which are occupied in the ground state. One of two initially zero energy modes remain occupied during spectral flow. The black bar corresponds to ultraviolet details which connect the two curves.

When the angular momentum shifts $n \to n+1$, a single charge has been transported from one edge to the other.

As seen in Fig. 3.4(b), the spectral flow as flux is adiabatically threaded through the vacancy induces energetic changes in the single particle energies. These changes at first glance appear to cancel, the modes of one edge state shift up while the other shift down. However, only negative energy modes contribute to the many-body ground state energy. Before threading flux, we have exact zero modes on the inner and outer edge, because one (the inner zero mode) moves to negative energy and the other (outer zero mode) moves to positive energy their contributions remain uncompensated. It is this effect that leads to a binding energy between lattice vacancies and Z_2 fluxes.

To make this argument quantitative we can calculate the ground state energy by summing over states. As mentioned earlier, when the number of vacancies that form the inner hole is odd the chiral edge state must possess a mode with exactly zero-energy. This zero mode corresponds to some angular momentum $k_0 = 2\pi n_0/L$, with n_0 integer, which we can set to zero for convenience. The mode energies in presence of the flux Φ are then $E_i(n,\Phi) = -v_E\frac{2\pi(n+\Phi)}{L}$ and $E_o(n,\Phi) = +v_E\frac{2\pi(n+\Phi)}{L_o}$. Summing over the states yields the shift in ground state energy as a function of flux Φ $(0 \le \Phi < 1)$:

$$\begin{aligned}\Delta E(\Phi) &= E(\Phi) - E(0)\\ &= -\frac{2\pi v_E}{L}\sum_{n=0}^{\infty}((n+\Phi)-n) - \frac{2\pi v_E}{L_o}\sum_{n=1}^{\infty}((n-\Phi)-n).\end{aligned} \tag{3.21}$$

These sums are seemingly divergent but are, in fact, regularized by the finite width of the edge dispersions, which are connected to each other through the bulk (see Fig. 3.4(b)). The physical regularization can be done by reducing the velocity toward zero with increasing n. To accomplish this we set $\frac{dE_i}{dk} = -v_E e^{-a|k|}$ with $a > 0$. Physically, a should cut off the growth of energies near the cutoff momenta Λ and therefore, a should be on the order of the lattice constant $l \sim 1/\Lambda$.

Integrating over k gives the regularized energies:

$$\begin{aligned} E_i(n,\Phi,a) &= -v_E\frac{1}{a}(1-\mathrm{sgn}(n+\Phi)e^{-a\frac{2\pi|n+\Phi|}{L}}), \\ E_o(n,\Phi,a) &= +v_E\frac{1}{a}(1-\mathrm{sgn}(n+\Phi)e^{-a\frac{2\pi|n+\Phi|}{L_o}}). \end{aligned} \tag{3.22}$$

Using these regularized energies and summing over states we can calculate the shift in ground state energy induced by threading $\Phi = 1/2$ flux:

$$\Delta E(\Phi = 1/2, a) = -\frac{v_E}{2a}\tanh\Big(\frac{\pi a}{2L}\Big). \tag{3.23}$$

As this energy is negative, in the language of the spin liquid, a Z_2 flux is bound. As the number of vacancies making up the hole tends to one ($L \sim \mathcal{O}(1)$) this binding energy becomes proportional to the cutoff energy Λ. As this binding energy is on the order of the cutoff Λ for any strength of time-reversal symmetry breaking, it must then continue to hold in the gapless case. Therefore, this topological argument ensures that lattice vacancies bind Z_2 fluxes in both the non-abelian and gapless Kitaev spin liquids.

In the limit of a large hole, or equivalently small a/L, summing over states yields the following simple form of the shift of ground state energy for arbitrary flux Φ:

$$\begin{aligned} \Delta E(\Phi,a) &= -\frac{v_E\pi}{L}(\Phi(1-\Phi)+\frac{a}{L}f(\Phi)+\mathcal{O}(\frac{a}{L})^2), \quad f(1/2)=0=f(0) \\ &\approx -\frac{v_E}{L}\eta(-\Lambda). \end{aligned} \tag{3.24}$$

While only $\Phi = 0$ and $\Phi = 1/2$ are possible for the individual spin liquid layers, this result shows that $\Phi = 1/2$ minimizes the ground state energy over all $U(1)$ possibilities. Another method that leads to the same answer, in this limit, is zeta function regularization as done in Section 3.2 for deriving a Friedel sum rule and it is presented in the appendix. Interestingly, we find that in this limit, the shift in ground state energy is proportional to the scattering phase shift due to a flux Φ at the cutoff scale.

A corollary of the topological argument is that in the limit of a large hole the flux binding is protected from generic local perturbations. Local perturbations cannot remove the chiral edge state, nor can they remove the edge mode at precisely zero energy when an odd number of vacancies form the inner hole. The perturbations could, for example, break the rotational symmetry, in which case we can no longer label the discrete states of the edge mode by angular momenta. But the charge pumping argument, which relies on the spectral flow of the zero-energy state still holds. Additionally, local perturbations with strength t can only couple to the Z_2 flux density at order $\mathcal{O}(L)$ in perturbation theory as a fermion must be transported around the hole to observe the flux. Intermediate states in this perturbation calculation will have fluxes excited on the perimeter of the hole because generic spin perturbations excite fluxes. Therefore, such contributions will be suppressed by a factor $(t/\Delta)^L$, where Δ is the Z_2 flux gap. In the context of the spin liquid, a strong on-site field could be added, effectively freezing a single spin and therefore adding another vacancy. Then we would no longer be guaranteed the zero mode that was critical for our argument. However, to freeze a spin would require a perturbation on the order of the cutoff scale.

Having argued that lattice vacancies bind Z_2 fluxes, we verify that these fluxes are accompanied by Majorana zero modes as expected for Ising anyons in the non-abelian phase. In our doubled

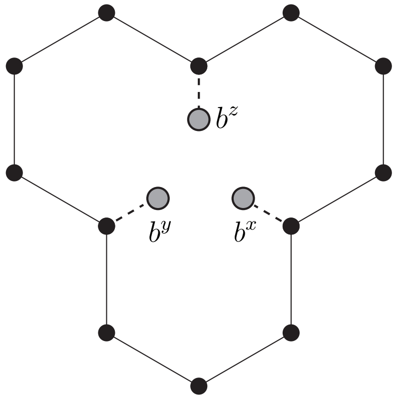

Figure 3.5: Creating a lattice vacancy breaks the bonds of the Z_2 bond variables. In the Kitaev honeycomb model a magnetic field couples the b and c Majorana, however in the general case an odd number of additional Majorana fermion will be coupled locally. This ensures that the result of threading a flux through a vacancy still creates an Ising anyon.

system the Majorana zero modes are doubled and therefore should show up as Dirac zero modes. However, as we have used extensively in the topological argument, a lattice vacancy creates a zero mode that is moved to non-zero energies by spectral flow when a Z_2 flux is adiabatically threaded. From this it might appear that Z_2 fluxes bound to lattice vacancies are not Ising anyons.

To understand the resolution to this problem we can first gain some intuition from Kitaev's honeycomb model. In this model each spin degree of freedom is composed of four Majorana modes, the c Majorana mode, and three b^γ Majoranas that constitute the gauge field. In the undisturbed honeycomb lattice these gauge field Majorana were paired into the Z_2 bond variables $u^\gamma_{jk} = ib^\gamma_j b^\gamma_k$. After their removal, the Majorana with which they paired into bond variables become decoupled (see Fig. 3.5). So, before inserting the flux we have four Majorana zero modes around the vacancy: the three unpaired b Majoranas and the vacancy induced zero mode in the c-Majorana sector. Inserting the Z_2 flux will pump out the c-zero mode leaving the three b^γ-modes at zero energy. In a generic model all four original zero modes will be coupled with each other. But this coupling cannot change the parity of Majorana zero modes. In particular, upon inserting the Z_2 flux, we will generically have one remaining zero mode, as expected for an Ising anyon.

3.4 Discussion

We have shown that lattice vacancies bind Z_2 fluxes in the gapless and gapped non-abelian Z_2 Kitaev spin liquids. This was shown from general properties of the spin liquids and did not rely on details of particular models. To remain model independent, our starting point was a low-energy theory for the spin liquid with vacancies and Z_2 fluxes. In the gapless case we showed that a lattice vacancy created an energetically expensive scattering resonance at zero energy and that a Z_2 flux suppressed this. We argued this first by introducing a Friedel sum rule for the scattering phase shift created by a vacancy with flux threaded through it. Then, by solving the scattering theory, we were able to directly calculate the binding energy. In the non-abelian phase, we showed that the binding energy in both phases had a topological origin. By doubling the effective theory of the spin liquid and identifying the system as a quantum Hall state we formulated a pumping argument for the binding energy. We showed that spectral flow induced by adiabatically threading a Z_2 flux through the vacancy reduced the ground state energy. This extends previous numerical results [163, 164, 70] on the Kitaev honeycomb model by ensuring that this is a generic property of the spin liquids considered.

The structure of the arguments presented in this chapter suggests several generalizations. While we focused only on Z_2 spin liquids, by doubling the spin liquid's effective theories we allowed for external $U(1)$ valued fluxes. Both the Friedel sum rule approach, and the topological argument, suggested that Z_2 fluxes produced the minimal ground state energy when threaded through a vacancy over all $U(1)$ possibilities. An honest calculation of the optimal $U(1)$ flux must include gauge field dynamics, which we have ignored due to the flux gap of the Z_2 phase. It is an interesting future direction to consider how dynamical gauge fields would modify this picture. Zooming a bit out on the structure of our argument, we included a Z_2 flux in a low-energy theory by minimally coupling an Aharonov-Bohm field to the fermions. The Aharonov-Bohm field's flux was fixed by the mutual statistic of the fermions and the fluxes. Such a calculation could be repeated for other anyon content. For instance, we could model the impact of another anyon's (potentially non-abelian) mutual statistic by minimally coupling a $U(N)$ valued "Aharonov-Bohm" field. Whether other types of point defects could be shown to trap other types of anyons remains to be seen.

Now that we have shown that lattice vacancies offer a robust tool for creating and trapping Ising anyons, we can consider how they can be utilized. Rydberg quantum simulators have created gapped abelian Z_2 spin liquids [137], and proposals for generating the spin liquids discussed in this chapter exist [69]. Creating lattice vacancies in optical lattice simulations simply corresponds to not trapping an atom. Therefore, the Rydberg atom simulations are well-equipped to use this feature of non-abelian spin liquids to create and trap Ising anyons. Even static trapped Ising anyons could be useful for a measurement based topological quantum computation scheme [24, 25]. While the non-abelian Z_2 spin liquid isn't sufficient for universal quantum computation [106], the circumstances leading to Ising anyons binding to lattice vacancies appear to be so general that we eagerly anticipate further study revealing a sufficient non-abelian spin liquid exhibiting the same effect.

Supplemental Material

In this supplemental material we will derive some of the results which were used in the main text. The goal of these calculations is to show that a lattice vacancy creates a binding energy for a Z_2 flux. The steps that are used to arrive at this fact are the following: first we derive the single particle solutions to the Dirac equations with and without a Z_2 flux, second we derive the associated Green's functions, third we solve for the Green's functions after a vacancy is introduced with scattering theory, finally these Green's functions can be utilized to calculate density of states and hence ground state energies to verify that a lattice vacancy binds a Z_2 flux. These steps each correspond to a section of this supplemental material. After this is accomplished, we demonstrate that a chiral spin liquid called the Yao-Kivelson-Kitaev (YKK) model also exhibits lattice vacancies binding Z_2 fluxes. To this end we first provide proof of what the background flux configuration in this model. In a particular limit the YKK model becomes the non-abelian Kitaev honeycomb model, and this argument therefore provides a proof of the ground state flux pattern in both models (that is commonly assumed to be true). Next, we show with exact finite lattice calculations that introducing a vacancy in the YKK model binds a Z_2 flux.

3.5 Low-Energy Theory - Single Particle Solutions

In this section of the supplementary material, we will solve for the single-particle solutions of the low-energy theory which is used in the main text. The starting point of our analysis of low-energy Hamiltonian of the isotropic Kitaev model [78]:

$$H_{\pm} = \pm m\sigma^z + v_f\left(\sigma^x(p^y - A_y) \pm \sigma^y(p^x - A_x)\right). \tag{3.25}$$

Here we have minimally coupled a vector potential A, the spin operators σ act on sublattice indices $(B,\, A)$ and $\pm$ refers to valley indices. This vector potential can be vanishing to describe a flux-free vacuum or set to be an Aharonov-Bohm field at the origin to describe the presence of a magnetic flux:

$$\vec{A} = \Phi\frac{\hat{\theta}}{r}. \tag{3.26}$$

We will only focus on the cases of $\Phi = 0$ and $\Phi = 1/2$. We will take the convention that the four component (sublattice and valley indices) spinor is written:

$$\psi = \begin{bmatrix} \psi_B^+ \\ \psi_A^+ \\ \psi_A^- \\ \psi_B^- \end{bmatrix}, \tag{3.27}$$

as in this basis the Hamiltonians in both valleys take the same form:

$$H = m\sigma^z + (-\sigma^y(p^x - A_x) + \sigma^x(p^y - A_y)). \tag{3.28}$$

The eigenfunctions of this Hamiltonian in each valley can be quickly found by utilizing the conservation of $J_z = -i\partial_\theta + \frac{\sigma^z}{2}$ which allows us to write the ansatz:

$$\psi_n(r,\theta) = \begin{bmatrix} f(r) \\ g(r)e^{i\theta} \end{bmatrix} e^{in\theta}. \tag{3.29}$$

With this ansatz the eigenvalue equation takes the form:

$$\begin{bmatrix} m & (\partial_r + \frac{n+1-\Phi}{r}) \\ (-\partial_r + \frac{n-\Phi}{r}) & -m \end{bmatrix} \begin{bmatrix} f(r) \\ g(r) \end{bmatrix} = E \begin{bmatrix} f(r) \\ g(r) \end{bmatrix}, \tag{3.30}$$

where here we have allowed for general flux Φ.

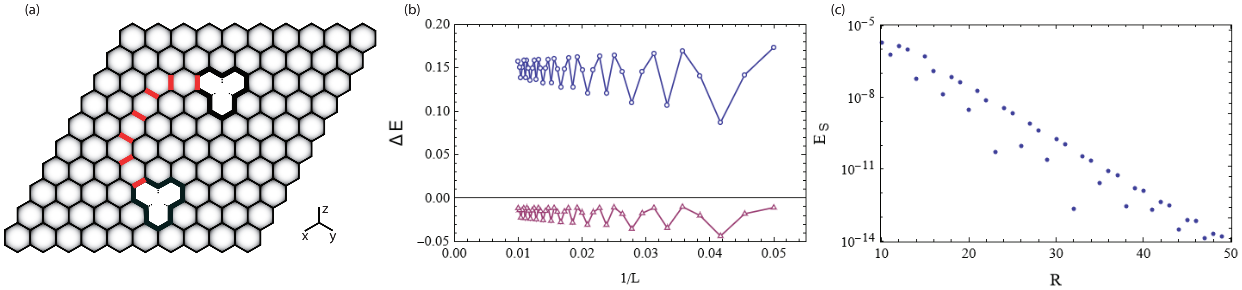

Figure 3.6: (a) Within the Kitaev honeycomb model lattice vacancies lead to a ground state flux configuration with a Z_2 flux that threads each hole. (b) Ground state energy cost of creating a flux with (red) or without (blue) a vacancy present as a function of system size. Energies are reported in units of J (c) The splitting of the lowest energy fermionic modes in the presence of a vacancy bound flux in the non-abelian phase is exponentially suppressed in distance separating them.

Solving this equation, we obtain the most general single particle solutions at energy E:

$$\psi_{E,n,\Phi}(r,\theta)=\begin{bmatrix}\frac{(E+m)}{\sqrt{(E-m)(E+m)}}(c_1J_{n-\Phi}(\sqrt{E^2-m^2}r)+c_2Y_{n-\Phi}(\sqrt{E^2-m^2}r))\\ (c_1J_{n+1-\Phi}(\sqrt{E^2-m^2}r)+c_2Y_{n+1-\Phi}(\sqrt{E^2-m^2}r))e^{i\theta}\end{bmatrix}e^{in\theta}, \tag{3.31}$$

with integration coefficients c_1 and c_2. When $\Phi=0$, in the absence of flux, the $r\to 0$ boundary condition is fixed by regularity. All the Y Bessel functions diverge at the origin, therefore $c_2=0$. The normalized $\Phi=0$ solutions are then given by:

$$\psi_{E,n,0}(r,\theta)=\frac{\sqrt{k}}{2\sqrt{\pi}}\begin{bmatrix}\mathrm{sgn}(E)\sqrt{1+m/E}(J_n(kr))\\ \sqrt{1-m/E}(J_{n+1}(kr))e^{i\theta}\end{bmatrix}e^{in\theta}. \tag{3.32}$$

For any $\Phi\neq 0$ the story is more complicated. For any $\Phi\neq 0$, there exists a single angular momentum sector n for which no choice of coefficients ensures regularity of the wavefunction. For $\Phi=1/2$, this is the $n=0$ sector. For all $|n|>0$, regularity fixes the integration constants:

$$\psi_{E,n,1/2}(r,\theta)=\frac{\sqrt{k}}{2\sqrt{\pi}}\begin{bmatrix}\mathrm{sgn}(E)\sqrt{1+m/E}(J_{|n-1/2|}(kr))\\ \mathrm{sgn}(n)\sqrt{1-m/E}(J_{|n+1/2|}(kr))e^{i\theta}\end{bmatrix}e^{in\theta}\quad |n|>0 \tag{3.33}$$

Ultimately, the unavoidable singularity in the $n=0$ sector implies that the correct boundary condition must be specified with other information. We will accomplish this by parameterizing all possible well-defined boundary conditions and then narrowing the possibilities with microscopic symmetries. Well-defined boundary conditions lead to solution spaces on which H is self-adjoint. To be self-adjoint H must be symmetric and the Hilbert space it acts on must be the same as its dual.

The symmetric condition is:

$$W=\langle\chi|H\psi\rangle-\langle H\chi|\psi\rangle=0. \tag{3.34}$$

The contribution of a single valley to W can be calculated by applying the Hamiltonian (Eq. (3.28)) and is simplified with an integration by parts leaving only a contribution from the origin:

$$W = 2\pi i \lim_{r\to 0}(r \begin{bmatrix} f^*_\chi & g^*_\chi \end{bmatrix} \sigma^y \begin{bmatrix} f_\psi \\ g_\psi \end{bmatrix}). \tag{3.35}$$

For $\Phi = 0$, the symmetric condition is immediately satisfied if we choose the regular solutions in each n sector as $J_n(cr) \propto (cr)^{|n|}$ near the origin. Similarly, for $\Phi = 1/2$, this is satisfied for all $|n| > 0$ if the regular solutions are chosen. This then only leaves the special $n = 0$ sector to be resolved when $\Phi \neq 0$.

Similar to Roy, Stone [127], who considered a modified graphene model, we ensure a self-adjoint Hamiltonian by imposing a boundary condition at $r \to 0$ parameterized in the following way:

$$\lim_{r\to 0} r^{1/2} \begin{bmatrix} \psi^+_B \\ \psi^-_A \end{bmatrix} = \lim_{r\to 0} r^{1/2} \begin{bmatrix} a & b \\ c & d \end{bmatrix} \begin{bmatrix} \psi^+_A \\ \psi^-_B \end{bmatrix}, \tag{3.36}$$

with a, b, c and d as free complex parameters. Plugging this into Eq. 3.28 we get a boundary condition on χ in the dual space:

$$\lim_{r\to 0} r^{1/2} \begin{bmatrix} \chi^+_B \\ \chi^-_A \end{bmatrix} = \lim_{r\to r_0} r^{1/2} \begin{bmatrix} a^* & c^* \\ b^* & d^* \end{bmatrix} \begin{bmatrix} \chi^+_A \\ \chi^-_B \end{bmatrix} \tag{3.37}$$

For both Hilbert spaces to be the same this matrix must be the same as this implies the boundary conditions for eigenvalues in the direct and dual space coincide. This implies for real variables A, B, C, D:

$$M = \begin{bmatrix} a & b \\ c & d \end{bmatrix} = \begin{bmatrix} A & C - iB \\ C + iB & D \end{bmatrix}. \tag{3.38}$$

Therefore, we have completely parameterized all boundary conditions that ensure the Hamiltonian is self-adjoint with four real numbers. Now, we can specify these numbers further with the input of symmetry. Recall that our underlying theory is built from two uncoupled layers of Majorana fermions. Because of this, we could only break time-reversal symmetry to generate a gap - and cannot open the trivial inversion symmetry breaking gap. Additionally, we can not break particle-hole symmetry. Inversion symmetry acts by swapping sublattice and valley indices respectively. This implies that the matrix M encoding the boundary conditions obey $\sigma^x M \sigma^x = M$. Particle-hole symmetry acts by flipping valley indices while maintaining sublattice indices and this translates into a condition $M^2 = 1$. Together, these conditions force $B = 0$, $A = D$, and $A^2 = C^2 = A^2 + C^2 = 1$. Up to phase redefinitions, the matrix M is either equal to the identity or σ^x. If we enforce an additional reflection symmetry, $M = \sigma^x$, however, this also follows from the more robust assumption that no bound state is valley-polarized (and hence doesn't carry momentum). We will therefore take $M = \sigma^x$ and verify our assertion after deriving the bound state spectrum.

Our boundary conditions therefore force a spinor near the origin (at fixed angle $\theta = 0$) to have ratios of components given by:

$$\begin{aligned} &\lim_{r\to 0}(r^{1/2}\psi^1 = r^{1/2}\psi^4), \\ &\lim_{r\to 0}(r^{1/2}\psi^2 = r^{1/2}\psi^3). \end{aligned} \tag{3.39}$$

The allowed scattering states are all solutions with $|E| > |m|$ that satisfy this condition near the origin. This condition is trivially satisfied for all $\Phi = 0$ solutions described previously, as they are regular near the origin. In the $n = 0$ sector of $\Phi = 1/2$, all wavefunctions have a $r^{-1/2}$ singularity rendering this condition non-trivial. To satisfy these boundary conditions, near $r \to 0$, all the $n = 0$ solutions must asymptote to:

$$\psi \approx r^{-1/2} \begin{bmatrix} x \\ y \\ y \\ x \end{bmatrix}, \tag{3.40}$$

at $\theta = 0$ for some constants x and y. All such scattering states are linear combinations of the following basis:

$$\begin{aligned} \psi_1 &= \frac{\sqrt{k}}{2\sqrt{2\pi}} \begin{bmatrix} \mathrm{sgn}(E)\sqrt{1-(m/E)^2}J_{-1/2}(kr) \\ (1-m/E)J_{1/2}(kr)e^{i\theta} \\ (1+m/E)J_{1/2}(kr) \\ \mathrm{sgn}(E)\sqrt{1-(m/E)^2}J_{-1/2}(kr)e^{i\theta} \end{bmatrix}, \\ \psi_2 &= \frac{\sqrt{k}}{2\sqrt{2\pi}} \begin{bmatrix} \mathrm{sgn}(E)(1+m/E)J_{1/2}(kr) \\ \sqrt{1-(m/E)^2}J_{-1/2}(kr)e^{i\theta} \\ \sqrt{1-(m/E)^2}J_{-1/2}(kr) \\ \mathrm{sgn}(E)(1-m/E)J_{1/2}(kr)e^{i\theta} \end{bmatrix}. \end{aligned} \tag{3.41}$$

Having completed the description of the scattering states we turn to bound modes, for which $|E| < |m|$. A bound mode must satisfy our boundary conditions (Eq. (3.40)) and be normalizable. To find the normalizable solutions, we start with the general solution set (Eq. (3.31)) and consider only solutions which decay at large distances. This relates the bound state energy to the ratio of spinor components, within a valley, at the origin:

$$\psi^1/\psi^2 = \mathrm{sgn}(m)\sqrt{\frac{m+E_B}{m-E_B}}, \tag{3.42}$$

where ψ is a pseudospin spinor and E_B is the energy of the bound state. Our boundary condition excludes a valley-polarized solution. To have a bound state, the energy of the bound state in the upper and lower valleys must match (as $H\psi = E\psi$). This forces $x/y = y/x = \pm 1$. Assuming without loss of generality $m > 0$, only the ratio $x/y = +1$ leads to a bound state and its energy is $E_b = 0$; that is, we have found a zero-mode. The wavefunction of this bound state is given by:

$$\psi_B(r,\theta) = \frac{e^{-r|m|}\sqrt{|m|}}{\sqrt{4\pi r}} \begin{bmatrix} \mathrm{sgn}(m) \\ e^{i\theta} \\ 1 \\ \mathrm{sgn}(m)e^{i\theta} \end{bmatrix}. \tag{3.43}$$

Had we instead taken $M = 1$ for our boundary conditions, we could form bound state solutions with only the top or bottom two components. These would be valley-polarized and have an unphysical net momentum of $K_\pm$. This complex zero-mode split between the two layers implies the existence of an unpaired Majorana zero-mode in each layer bound to the flux, as expected in the non-abelian spin liquid.

3.6 Low-Energy Theory - Initial Green's functions

In the main text we refer to the Green's functions of the system before a vacancy is created as the initial Green's functions and label them with a superscript G^0. In this appendix we will calculate the initial Green's functions G^0 and from these we will obtain the density of states (with and without flux) prior to creating lattice vacancies. We can calculate the Green's functions directly by summing and integrating over the bound and scattering solutions respectively:

$$G_{\alpha_1\beta_1;\alpha_2\beta_2}(r,r',z) = \int dk(\sum_n \frac{\psi_{n,E(k)}(r)\psi^\dagger_{n,E(k)}(r')}{z-E(k)} + \sum_n \frac{\psi_{n,-E(k)}(r)\psi^\dagger_{n,-E(k)}(r')}{z+E(k)}) + \sum_i \frac{\psi_i(r)\psi_i^\dagger(r')}{E-E_i}. \tag{3.44}$$

In this equation G is retarded, z has small positive imaginary part, the states are continuum normalized with norm of $\delta(k-k')$. All wavefunctions ψ have pseudospin (sublattice) indices α and valley indices β.

To calculate the density of states, we need to evaluate the trace of the Green's function. For this we first calculate the on-site Green's function in the case of $\Phi = 0$. Plugging the solutions Eq. (3.32) into the definition of the Green's function we arrive at:

$$\mathrm{Tr}G(r,r,z) = \int \frac{2zkdk}{\pi(z^2-E^2(k))} \sum_{n=-\infty}^{\infty} J_n^2(kr) = \int \frac{2zkdk}{\pi(z^2-E^2(k)} = \frac{z}{\pi}\log\left(\frac{m^2-z^2}{m^2+\Lambda^2-z^2}\right). \tag{3.45}$$

The local density of states is given by the imaginary part of this expression:

$$\rho(r,E) = -\frac{1}{\pi}\mathrm{Im}\mathrm{Tr}G(r,r;z) = \frac{|E|}{\pi}\Theta(E^2-m^2). \tag{3.46}$$

Here Θ is the Heaviside theta function. We have recovered the familiar Dirac conical density of states.

As discussed in the main text, the response to a vacancy can be calculated with the sublattice-polarized and valley-even component of the initial Green's function, G^0. A calculation like the one above yields:

$$G^0(r_v,r_v;z)_{+x,A;+x,A} = \frac{z}{4\pi}\log\left(\frac{m^2-z^2}{m^2+\Lambda^2-z^2}\right). \tag{3.47}$$

Repeating the above calculations for the $\Phi = 1/2$ case, we find that the local density of states will vary dramatically from the $\Phi = 0$ case near the origin. However, the integrated density of states will be identical with the exception of an increase of density of states at $E = 0$. Plugging in the $\Phi = 1/2$ solutions (Eq. (3.33),(3.41),(3.43) to the Green's function definition we arrive at the following:

$$\begin{aligned}
\mathrm{Tr}G(r,r;z) &= \int \frac{2zkdk}{\pi(z^2-E^2(k))}(2\sum_{n=0}^{\infty} J^2_{n+1/2}(kr) + \frac{(E^2(k)-m^2)}{2E^2(k)}(J^2_{-1/2}(kr) - J^2_{1/2}(kr)) \\
&+ \frac{|m|e^{-2r|m|}}{\pi r z} \\
&= \int \frac{2zkdk}{\pi(z^2-E^2(k))}(\frac{2\mathrm{Si}(2kr)}{\pi} + \frac{E^2(k)-m^2}{2E^2(k)}(J^2_{-1/2}(kr) - J^2_{1/2}(kr)) + \frac{|m|e^{-2r|m|}}{\pi r z} \\
&= G_{\Phi=0}(r,r;z) \\
&+ \int \frac{2zkdk}{\pi(z^2-E^2(k))}(\frac{2\mathrm{Si}(2kr)}{\pi} - 1) + \int \frac{2zk^2\cos(2kr)dk}{\pi^2 r E^2(k)(z^2-E^2(k))} + \frac{|m|e^{-2r|m|}}{\pi r z},
\end{aligned} \tag{3.48}$$

where the last term came from the bound state and $E(k) = \sqrt{m^2+k^2}$ is the dispersion of the Dirac modes. In the previous expression Si is the Sin Integral which approaches $\pi/2$ as its argument goes to infinity and zero as its argument goes to zero. The grouping of terms was chosen to demonstrate that as distance from the origin grows the Green's function becomes identical to the $\Phi = 0$ case. At short distances there are strong deviations coming from the $n = 0$ angular momentum sector, which contribute the $1/rE$ singularity.

Using this Green's function to calculate the local density of states we arrive at:

$$\rho(r,E) = \frac{|E|}{\pi}(\frac{2\mathrm{Si}(2kr)}{\pi} + \frac{k\cos(2kr)}{E^2\pi r})\Theta(E^2-m^2) + \frac{|m|e^{-2rm}}{\pi r}\delta(E), \tag{3.49}$$

where we see an enhancement of local density of states at small k and r. To get the total density of states we can integrate the Green's function over space, momenta and take the imaginary part:

$$\begin{aligned}
\rho(E) &= -\frac{1}{\pi}\mathrm{Im}(2\pi\int rdr\mathrm{Tr}G(r,r,z)) \\
&\underset{\Lambda\to\infty}{=} \rho_{\Phi=0}(E) - \frac{1}{4}(\delta(E-M)+\delta(E+M)) + \delta(E).
\end{aligned} \tag{3.50}$$

This expression can be derived by integrating against e^{-ar} and taking the limit as $a \to 0^+$. At $m = 0$ we have the simple result:

$$\rho(E) = \rho_{\Phi=0}(E) + \frac{1}{2}\delta(E). \tag{3.51}$$

The shift of density of states due to the creation of a flux at finite cutoff depends on cutoff implementation details. However, the restriction of remaining half-filled implies that the worst-case in terms of flux energy (largest energetic cost) is that the low-energy change of density of states is totally compensated at the band edge:

$$\rho(E) = \rho(E)_{\Phi=0} = -\frac{1}{4}(\delta(E-\Lambda)+\delta(E+\Lambda)+\delta(E-m)+\delta(E+m)) + \delta(E), \tag{3.52}$$

which we will assume for the sake of making the strongest argument that threading a flux through a vacancy is the preferred ground state. One particular implementation of the cutoff would be to restrict integration of Eq. (3.49) over space to $r \gtrapprox 1/\Lambda$, effectively softening the singularity of the near flux modes. In such a case the largest reduction of density of states occurs near $k = 0$ instead of the band edge.

We can also compute the valley-even sublattice polarized Green's function for the $\Phi = 1/2$ case:

$$\begin{aligned} G^0(r_v, r_v, z)_{+x,A;+x,A} = & \int \frac{2zkdk}{\pi(z^2 - E^2(k))}\Big(\frac{\mathrm{Si}(2kr_v)}{2\pi} + \frac{E^2(k) - m^2}{4E^2(k)}(J^2_{-1/2}(kr_v) - J^2_{1/2}(kr_v)) \\ & + \frac{|m|e^{-2r_v|m|}}{2\pi r_v z} \\ \approx & -\frac{2r_v z}{\pi^2}(\Lambda - \sqrt{m^2 - z^2}\arctan\left(\frac{\Lambda}{\sqrt{m^2 - z^2}}\right) - \frac{ie^{2ir_v\sqrt{z^2-m^2}}\sqrt{z^2 - m^2}}{2\pi r_v z}, \end{aligned} \tag{3.53}$$

in the last equality we have taken $\mathrm{Si}(2kr) \approx 2kr$, and the remaining terms are evaluated in the infinite cutoff limit. Approximating the sine integral is valid for $kr < \pi/4$ as the vacancy is located as close to the origin as possible. The first term vanishes as $z \to 0$, so the second term dominates the low-energy physics.

3.7 Low-Energy Theory - Vacancy Scattering

In this section of the supplemental material we apply scattering theory techniques to exactly solve for the change in density of states induced by lattice vacancies [92, 46, 61].

We will model a vacancy with the limit of a large on-site potential V. H^0 corresponds to the Hamiltonian before introducing a vacancy for which we have already solved for a Green's function G^0. The Green's function including the perturbation, G, must satisfy:

$$(z - H^0 - V)G(r, r', z) = 1. \tag{3.54}$$

Multiplying by G^0 we obtain the following equation for G:

$$G(r, r', z) = G^0(r, r', z) + G^0(r, r'', z)V(r'')G(r'', r', z). \tag{3.55}$$

Iterating this equation, we get a formal solution:

$$\begin{aligned} G &= G^0 + G^0 T G^0 \\ T &= V + V G^0 V + \ldots . \end{aligned} \tag{3.56}$$

If this T matrix is known exactly, it can be used to directly calculate the change in density of states induced by the scattering potential V [92]:

$$\Delta\rho(E) = \frac{1}{\pi}\partial_E \arg\det(T(E)). \tag{3.57}$$

This expression was used in the main text to write a Friedel sum rule.

In the case of a point potential the T matrix can be evaluated explicitly. We specify $V = U\delta_{r,r_v}$ to be an onsite (position r_v) potential of strength U, then this infinite sum can be carried out:

$$\begin{aligned} T(r,r',z) &= \delta_{r,r_v}\delta_{r',r_v}\frac{U}{1-UG^0(r_v,r_v,z)} =_{U\to\infty} -\delta_{r,r_v}\delta_{r',r_v}\frac{1}{G^0(r_v,r_v,z)} \\ G(r,r',z) &= G^0(r,r',z) - \frac{G^0(r,r_v,z)G^0(r_v,r,z)}{G^0(r_v,r_v,z)}, \end{aligned} \tag{3.58}$$

where we have introduced a vacancy by taking the limit of infinite on-site potential. Therefore, given the initial Green's functions G^0 we arrive at the solution for the system when perturbed by a vacancy G. We will use this to calculate the shift in density of states induced by the vacancy and from there the ground state energy differences between having and not having a flux.

The local density of states (LDOS) can be calculated from the imaginary part of G:

$$\rho(r,E) = -\frac{1}{\pi}\mathrm{Im}(G(r,r',z)). \tag{3.59}$$

We can calculate the shift in LDOS by taking only the imaginary part of the difference $G - G^0$:

$$\Delta\rho(r,E) = \frac{1}{\pi}\mathrm{Im}(\frac{G^0(r,r_v,z)G^0(r_v,r,z)}{G^0(r_v,r_v,z)}). \tag{3.60}$$

Summing over all r, the total change in density of states can be written simply as:

$$\begin{aligned} \Delta\rho(E) &= \frac{1}{\pi}\mathrm{Im}\frac{1}{G^0(r_v,r_v,z)}\sum_r G^0(r_v,r,z)G^0(r,r_v,z) \\ &= -\frac{1}{\pi}\mathrm{Im}\frac{\partial_E G^0(r_v,r_v,z)}{G^0(r_v,r_v,z)} \\ &= -\frac{1}{\pi}\mathrm{Im}\partial_E \ln\big(G^0(r_v,r_v,z)\big) \\ &= \partial_E \mathrm{Arg}\frac{1}{G^0(r_v,r_v,z)}. \end{aligned} \tag{3.61}$$

Here we have used the identities [61]:

$$\int d\vec{r}G^0(r_v,r,z)G^0(r,r_v,z) = \langle r_v|((G^0)^2|r_v\rangle = \langle r_v|(-\frac{\partial G^0}{\partial E})|r_v\rangle. \tag{3.62}$$

In our double-valley model an on-site (on fixed sublattice) potential V, which scatters between all momenta, will be represented by:

$$V \approx u(r)(1+\sigma^z)\otimes(1+\tau^x), \tag{3.63}$$

where $u(r)$ is a sharply peaked function of r which we can take to be a delta function. This modifies our previous solution only in presentation:

$$\begin{aligned} T(z) &= (1 + 4UG^0(r_v,r_v,z)_{+x,A;+x,A} + (G^0(r_v,r_v,z)_{+x,A;+x,A})^2 + \ldots)V \\ &= (1 - 4UG^0(r_v,r_v;E)_{+x,A;+x,A})^{-1}V \\ \lim_{U\to\infty} T(z) &= -\delta(r-r_v)(G^0(r_v,r_v;z)_{+x,A;+x,A})^{-1}\frac{(1+\sigma^z)}{2}\otimes\frac{(1+\tau^x)}{2}. \end{aligned} \tag{3.64}$$

Here we have indicated that the Green's function is taken from the A sublattice and valley-even $(+x)$ component.

The shift in total density of states is then given by:

$$\Delta\rho(E) = \partial_E \mathrm{Arg} \frac{1}{G^0(r_v, r_v, z)_{+x,A;+x,A}}. \tag{3.65}$$

To find the response of the flux-free system to the creation of a vacancy we can use the Green's function Eq. (3.47) in the shift of density formula Eq. (3.65):

$$\Delta\rho(E) = \delta(E) - \frac{2(\Lambda^2)|E|}{(\Lambda^2 + m^2 - E^2)(E^2 - m^2)(\pi^2 + (\log\left(|\frac{m^2-E^2}{\Lambda^2+m^2-E^2}|\right))^2)} \Theta(E^2 - m^2) \approx \delta(E), \tag{3.66}$$

where the approximation is taking the infinite cutoff limit. At all values of m, a vacancy induces a shift of density of states at $E = 0$ by introducing a delta function. At $m = 0$ this is a resonance and at $m \neq 0$ this a vacancy bound state. As the model is forced to remain at half-filling due to particle-hole symmetry of the Majorana fermions, a single charge must be removed from the band edge to accommodate the removal of a half-charge and the zero-energy resonance.

Similarly, the shift in density of states caused by a vacancy when a Z_2 flux $(\Phi = 1/2)$ is present can be calculated by utilizing Eq. (3.53) and Eq. (3.65):

$$\Delta\rho(E) \approx -\delta(E) + \frac{1}{2}(\delta(E+m) + \delta(E-m)) =_{m\to 0} 0. \tag{3.67}$$

We see the vacancy gets rid of the flux zero mode and transfers spectral weight to the gap edges at finite mass. Note that this shift is relative to the Z_2 flux ground state in the absence of a vacancy. Comparing the shift in density of states to the flux free ground state without vacancy or flux, reveals a shift of $\frac{1}{2}\delta(E)$ at $m = 0$. Compared to the case of a vacancy with no flux, this has reduced the zero energy resonances spectral weight by half and returns a quarter charge to each band edge.

3.8 Regularizations of Ground State Energy Sum

In this appendix we show an equivalence of two regularizations of the ground state energy sum utilized in Section 3.3. The sum was:

$$\begin{aligned}\Delta E(\Phi) &= E(\Phi) - E(0) \\ &= -\frac{2\pi v_E}{L}\sum_{n=0}^{\infty}((n+\Phi) - n) - \frac{2\pi v_E}{L_o}\sum_{n=1}^{\infty}((n-\Phi) - n).\end{aligned} \tag{3.68}$$

In the main text we used a physically motivated regularization which let the velocity approach zero with increasing $|n|$. This was accomplished by setting $\frac{dE_i}{dk} = -v_E e^{-a|k|}$ with $a > 0$. Integrating this yielded the energies for modes on the inner and outer edges:

$$\begin{aligned}E_i(n,\Phi,a) &= -v_E \frac{1}{a}(1 - \mathrm{sgn}(n+\Phi)e^{-a\frac{2\pi|n+\Phi|}{L}}), \\ E_o(n,\Phi,a) &= +v_E \frac{1}{a}(1 - \mathrm{sgn}(n+\Phi)e^{-a\frac{2\pi|n+\Phi|}{L_o}}).\end{aligned} \tag{3.69}$$

For $a > 0$, the sums become convergent geometric series and the ground state energy can be evaluated. At $\Phi = 1/2$, in the large outer boundary limit, the shift in ground state energy at general a is given by:

$$\Delta E(\Phi = 1/2, a) = -\frac{v_E}{2a} \tanh\left(\frac{\pi a}{2L}\right). \tag{3.70}$$

At general flux Φ, in the large-hole limit $a/L \ll 1$, the shift in ground state energy is given by:

$$\Delta E(\Phi, a) = -\frac{v_E \pi}{L}(\Phi(1-\Phi) + \frac{a}{L} f(\Phi) + \mathcal{O}(\frac{a}{L})^2), \quad f(1/2) = 0 = f(0). \tag{3.71}$$

The $a/L \to 0$ limit yields a universal contribution which agrees between different regularization techniques.

An alternative approach to calculating these sums starts directly with the sum (Eq. (3.68)) and uses zeta function regularization. For this we first exponentiate each term of Eq. (3.68) to some power $-s$. For sufficiently large real s, these sums then converge and can be analytically continued back to power $s = -1$. That is we can calculate the finite part of $\Delta E(\Phi) = \Delta E(\Phi, s = -1)$ from the following:

$$\begin{aligned} \Delta E(\Phi, s) &= -\frac{2\pi v_E}{L} \sum_{n=0}^{\infty} ((n+\Phi)^{-s} - n^{-s}) - \frac{2\pi v_E}{L_o} \sum_{n=1}^{\infty} ((n-\Phi)^{-s} - n^{-s}) \\ &= -\frac{2\pi v_E}{L} (\zeta_H(s, \Phi) - \zeta_R(s)) - \frac{2\pi v_E}{L_o} (\zeta_H(s, 1-\Phi) - \zeta_R(s)), \end{aligned} \tag{3.72}$$

where $\zeta_R(s) = \sum_{n=0}^{\infty} n^{-s}$ is the Riemann zeta function and $\zeta_H(s, \Phi) = \sum_{n=0}^{\infty} (n+\Phi)^{-s}$ is the Hurwitz zeta function. Utilizing the identities $\zeta_R(-1) = -\frac{1}{12}$ and $\zeta_H(-1, \Phi) = \frac{1}{2}\Phi(1-\Phi) - \frac{1}{12}$, in the large outer length limit, we arrive at the shift in ground state energy:

$$\Delta E(\Phi) = -v_E \pi \Phi (1-\Phi) \frac{1}{L}, \tag{3.73}$$

identical to the energy calculated from the other regularization approach.

3.9 Ground State Flux Configuration With and Without Vacancies in the Yao-Kivelson-Kitaev Model

The Yao-Kivelson-Kitaev (YKK) model is a modified Kitaev honeycomb model that realizes a true chiral spin liquid phase because its ground state spontaneously breaks time-reversal symmetry [174]. In the YKK model, each spin on the honeycomb lattice is replaced with three spins forming a triangle (as seen in Fig. 3.7). Each bond of the original hexagon is assigned a spin component $\gamma in\{x, y, z\}$ depending on its orientation, as in the Kitaev model. Similarly, each bond orientation of the new triangles is assigned a spin component γ'. Then the Hamiltonian is given by:

$$H = -J \sum_{\langle j,k \rangle_\gamma} \sigma_j^\gamma \sigma_k^\gamma - J' \sum_{\langle j,k \rangle_{\gamma'}} \sigma_j^{\gamma'} \sigma_k^{\gamma'}. \tag{3.74}$$

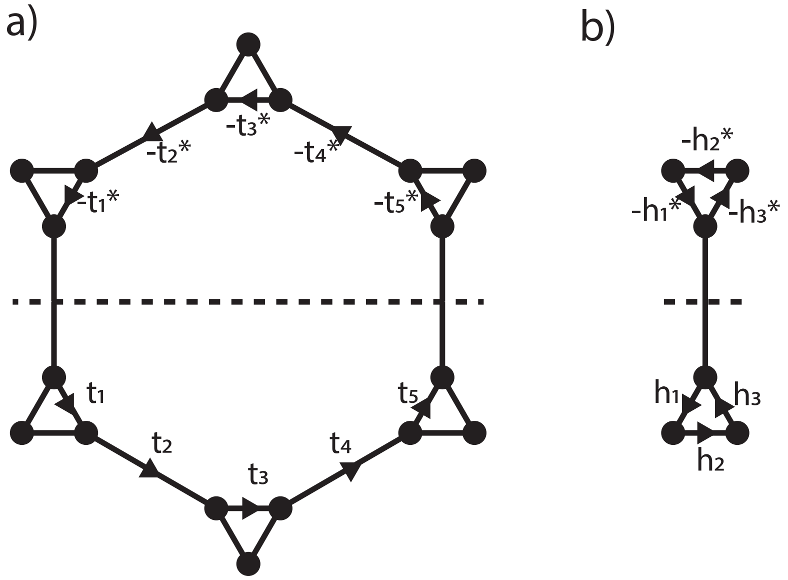

Figure 3.7: (a) The reflected flux configuration of an elementary dodecahedron. The phase acquired closing a loop is π (b) The reflected flux configuration of an elementary triangle. We can't specify what the flux is, however after reflection, both triangles have the same flux.

Here $\langle j,k\rangle_\gamma$ corresponds to nearest neighbors on the hexagonal bonds, and $\langle j,k\rangle_{\gamma'}$ corresponds to nearest neighbors on the triangular bonds. This model is solved using the same techniques as in the Kitaev honeycomb model, by introducing four Majorana and a Z_2 constraint. With this substitution the model reduces to a Hamiltonian of free Majorana fermions hopping in a frozen Z_2 gauge field. We seek to verify that in this spin liquid that vacancies also bind Z_2 fluxes. However, the ground state flux pattern of this model is not provided by Lieb's theorem [91, 90], and has only been suggested from numerical results. In this section, we will first prove what the optimal flux pattern is, and then check that introducing a lattice vacancy binds a Z_2 flux relative to this.

In the limit where the triangle bond strengths J' are much larger than the hexagon bond strengths J, this model coincides with the non-abelian Kitaev honeycomb model [174]. Lieb's theorem only guarantees the flux pattern in the Kitaev honeycomb model in the gapless and Toric code phases [91, 90]. Hence, a proof in the YKK model of the optimal flux immediately provides a proof of the optimal flux for the non-abelian Kitaev honeycomb model as well.

Lieb's theorem doesn't apply to the triangle-honeycomb lattice, however, we will be able to leverage one of his lemmas to demonstrate the optimal flux pattern. Our task is to find the minimal ground state energy, provided we are given a free fermionic hopping model with hopping strengths, but not hopping phases, which are fixed. Assuming that the hopping model is half-filled (ours must be as our model is built from Majorana fermions), and that the magnitude of the hopping coefficients are reflection symmetric with respect to some symmetry cut, then the conditions for his

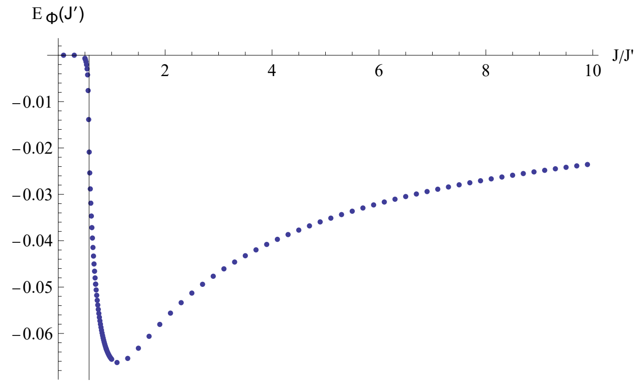

Figure 3.8: We compare the ground state energy through a vacancy with and without a flux as a function of the ratio of J/J'. Negative energies correspond to a preference for lattice vacancies to bind a flux. The phase transition from the abelian to non-abelian phase is indicated with vertical line at $J/J' = 1/\sqrt{3}$.

reflection positivity lemma are satisfied [91, 90]. This lemma states that if the ground state energy of some flux configuration is minimal, then the ground state energy of a flux configuration where the phases are unchanged on one side of the symmetry cut, and reflected with a π phase shift on each bond on the other side, also yields a minimal ground state energy (see Fig. 3.9). This holds also at finite temperature where the free energy replaces the ground state energy. It also continues to hold in the presence of interactions which respect the joint action of complex conjugation, particle-hole transformation and geometric reflection.

The structure of our argument than assumes that we start with some unknown optimal flux configuration and by a sequence of the combined reflection operations transform the flux configuration such that we completely fix it (up to a degeneracy related to spontaneous breaking of time-reversal symmetry). First, we apply the lemma to a horizontal cut through vertical honeycomb edges. Focusing on a single dodecagon we see that the flux encircled by traversing a dodecagon after applying the lemma is:

$$\mathrm{Arg}(t_1 t_2 t_3 t_4 t_5 (-t_5^*)(-t_4^*)(-t_3^*)(-t_2^*)(-t_1^*)) = \pi, \tag{3.75}$$

(see Fig. 3.7 (a)). Therefore, all the dodecagons have optimal flux π.

Demonstrating the optimal flux pattern of the triangles takes a sequence of applications of Lieb's lemma, and we will find that two equivalent configurations exist corresponding to a spontaneous breaking of time-reversal symmetry. Our underlying model is composed of Majorana fermions and therefore the flux through any triangle must be $\pm\pi/2$ as all hoppings can be taken complex. Assuming that the flux through a lower triangle along a horizontal symmetry cut is fixed to be Φ, we can show that after the cut the triangle above it must also have flux Φ as the hopping operator traversing the upper triangle is $(-h_3^*)(-h_2^*)(-h_1^*) = h_1 h_2 h_3$ as the hoppings can be taken complex. We show in Fig. 3.9 how via a sequence of symmetry cuts one can completely cover all triangles with the same flux Φ. The first sequence of steps are designed to ensure all triangles in a row of honeycombs agree. This is achieved by staggering horizontal and vertical cuts, where at each stage the vertical cut is moved to the right by one honeycomb. After a horizontal row of honeycombs have triangles all with the same flux this row can be repeatedly "folded" upwards by taking horizontal cuts directly above the boundary of the triangles whose flux have been already fixed. After this sequence of applications of Lieb's lemma all triangles agree and can either be set to $\pi/2$ and $-\pi/2$, the two must both be optimal as they are related by the time-reversal symmetry that the Hamiltonian is invariant under.

Therefore, we've established that the optimal ground state energy flux corresponds to a fixed choice of $\pm\pi/2$ uniformly in all triangles and π in each dodecagon.

We can now ask the question: do lattice vacancies trap Z_2 fluxes in this model relative to this background? By direct numerical evaluations of the ground state energy on finite lattices we find that they do. Flux binding occurs in both phases, however, the binding energy quickly decreases in the abelian phase. We display the results in Fig. 3.8.

It is worth noting that the maximal binding energy of a Z_2 flux to a lattice vacancy in the YKK model is nearly three times larger than the binding in the Kitaev honeycomb model with the same coupling strengths. This might be useful if trying to engineer a spin liquid for the purpose of topologically protected qubits as the errors are suppressed exponentially in this gap [78].

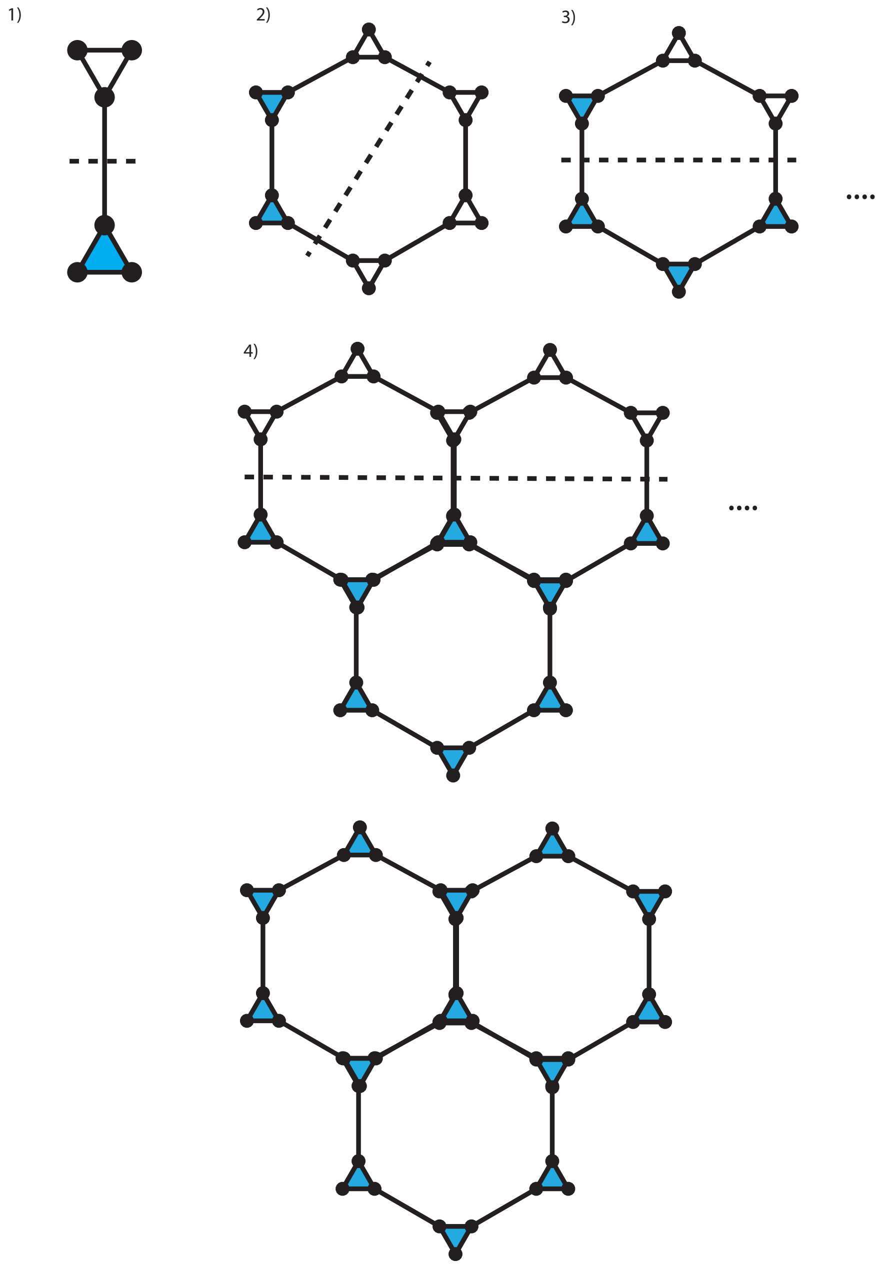

Figure 3.9: By repeatedly applying Lieb's lemma we can show that an optimal flux configuration can be taken to have flux which agrees in all triangles. Blue triangles represent a fixed flux $\pm\pi/2$ and the white triangles represent undetermined flux.

Chapter 4

Solvable Models of Strange Metals at the Fermi Liquid - Fermi Liquid* Transition

4.1 Introduction

In this chapter, based on the collaboration [4], we consider a phase transition under which a heavy fermion material breaks down and a fractionalized Fermi liquid emerges. Unlike the previous chapters in which we considered insulating spin liquid phases, these metallic phases can be probed with electrical transport measurements. We will introduce a family of solvable models describing this transition with which we can analyze the impact of spatially disordered interactions on transport phenomenon.

The properties of heavy fermion materials have been a continued source of fascination, calling fundamental concepts of solid state physics into question [144]. An important ingredient in the physics of the HFMs is the coexistence and interplay of conduction electrons with a half filled localized valence electron band behaving as local spin-1/2 moments [45]. Early on, a mechanism was proposed whereby the valence levels (VLs) effectively hybridize with the conduction electrons through Kondo-like screening of their spin [125, 36]. This mechanism explains the establishment of a heavy Fermi liquid (FL) with a large Fermi surface (FS) that includes both the conduction and valence electrons as required by Luttinger's theorem. However, many of these materials can be tuned through quantum critical points (QCPs) at which the large FS gives way to one with a small volume, equal to the filling of the conduction band alone [143, 109, 51, 98].

Reconstruction of the FS can occur through two distinct routes. The first is through symmetry breaking, such as an antiferromagnetic transition, as seen in CeRhIn$_5$ [143]. In this case the emergent small FS satisfies Luttinger's theorem within the new reduced Brillouin zone. However recent experiments with a related material, CeCoIn$_5$ [98] suggest a FS changing transition without symmetry breaking.

Such a transition has a simple description within a scheme [36, 139] in which the Kondo interaction is expressed as a coupling to a bosonic valence fluctuation, *i.e.* $c^\dagger_\sigma f_\sigma b$. Here, c_σ represents the conduction electron with spin index σ, and f_σ is a fermion operator carrying the spin of the singly occupied VLs. Hybridization between the conduction and valence bands emerges with condensation of the boson b, leading to the creation of a heavy FL phase.

As emphasized by Senthil et. al. [139], besides carrying a physical electron charge, this boson is also charged under an emergent $U(1)$ gauge field that fixes the local occupation of the VLs. Therefore, condensation of b in the heavy FL phase leads to confinement through the Higgs mechanism. In the gapped (uncondensed) phase of the boson, on the other hand, the VLs effectively decouple from the Fermi sea and form a $U(1)$ spin liquid. This phase is referred to as a fractionalized Fermi liquid (FL*), and it was argued that it supports a small FS [138], thereby obeying a generalized form of Luttinger's theorem [108].

This so-called "slave boson" theory [36, 139] describes a route for a transition involving change in the FS volume without symmetry breaking. However, the standard large N approach [36] used to approximate the theory fails to capture essential properties of QCPs seen in HFMs; it does not offer a robust explanation of the ubiquitous "strange metal", with its linear in temperature (T) resistivity ρ_{xx} at the QCP [146, 98]. The essential problem in the theory is that the feedback of the single critical boson on a large number of N fermion species is suppressed by $1/N$. The conduction electrons are therefore non-interacting at the large N saddle point. Thus, the same feature that makes this theory solvable also prevents it from describing a fully strongly coupled QCP.

In this paper, we introduce a valence fluctuation theory, which captures a strongly coupled QCP showing marginal Fermi liquid (MFL) phenomenology [155] and strange metal T-linear resistivity, in a solvable limit. We start from the same degrees of freedom as in the slave boson theory described above [36, 34]. However we introduce a different large N limit, which allows controlled calculation of transport properties nonperturbatively.

The new large N limit is inspired by recent work on "low rank" Sachdev-Ye-Kitaev (SYK) models, in which N fermion flavors interact via random Yukawa couplings with αN boson flavors [22, 111, 100, 157, 47, 75]. Recently, this approach has been used to compute quantum critical properties and quantum chaos in the 2+1-dimensional Gross-Neveu-Yukawa model, namely, massless Dirac fermions coupled to a critical boson field [74]. The critical exponents found at the saddle point level are in excellent agreement with those obtained from conformal bootstrap, even for moderate values of N. The key advantage compared to the standard large N limit is that, because both the fermion and boson numbers scale with N, the saddle point equations include self-consistent feedback between them, allowing us to capture a strongly coupled QCP.

We implement the large N scheme in the Kondo lattice problem by introducing N flavors of the spin-1/2 fermions c_σ and f_σ, and of the valence fluctuation (spin-0) boson b, while retaining the global $su(2)$ spin symmetry. We consider two distinct models of the fermion-boson couplings g^r_{ijk}. In Model I, the couplings are spatially disordered, and in Model II they are flavor random but translationally invariant. Thus, the randomness in Model II is just a theoretical tool. Integrating over it may be viewed as averaging over an ensemble of translationally invariant models that all yield identical long wavelength behavior.

In both models, we obtain a QCP showing linear in T resistivity up to logarithmic corrections, however these critical points describe transitions between slightly different phases. In Model I, we obtain the linear in T resistivity at the QCP only if the heavy FL transitions to a "layered FL*" phase, where the spinons f_σ and boson b are deconfined only within two-dimensional (2D) planes. In Model II, on the other hand, the MFL is obtained at a transition to a fully three-dimensional (3D) FL* phase. Moreover, not only is the resistivity linear in T at the QCP, the transport lifetime always takes the universal “Planckian” value $\tau_{tr} \approx \hbar/(k_B T)$. Model I by contrast can be tuned between a strongly damped ”Planckian” regime, and a weakly damped MFL charaterized by a sub-Planckian linear in T relaxation rate. Interestingly, in the weakly damped MFL regime, we find an enhancement of the Hall coefficient R_H in the critical regime, similar to recent experimental findings in CeCoIn$_5$ [98].

The rest of the paper is organized as follows: in Section II, we review the standard large N approach to Kondo lattice models and then introduce the new large N limit. In Sections III and IV we solve two models, with and without translation invariance, in this large N limit, and calculate transport quantities. We find strange metal behavior with T-linear resistivity at the QCP, and the evolution of the Hall resistivity across the QCP confirms a change of carrier density, with an additional enhancement of the Hall coefficent near criticality.

4.2 Large N Kondo Lattice Models

In HFMs, rare earth or actinide ions contribute a lattice of localized valence spins $\vec{S}$ coupled to the mobile conduction electrons c_σ. The essential low energy physics of HFMs are generally believed to be captured by the Kondo lattice model and variations of it [45]:

$$H = \sum_{k,\alpha} \epsilon_{c,k} c^\dagger_{k,\alpha} c_{k,\alpha} + J_K \sum_{r,\alpha,\beta} (\vec{S}_r \cdot c^\dagger_{r,\alpha} \vec{\sigma}_{\alpha\beta} c_{r,\beta}), \tag{4.1}$$

where $\epsilon_{c,k}$ is the momentum (k) space dispersion of the conduction electrons. The localized valence spin at lattice site r can be expressed in terms of Abrikosov fermions (spinons):

$$\vec{S}_r = \sum_{\alpha,\beta} f^\dagger_{r,\alpha} \frac{\vec{\sigma}_{\alpha\beta}}{2} f_{r,\beta}, \tag{4.2}$$

which are subject to a single occupancy constraint at each lattice site. The Kondo coupling is written as a quartic interaction between these fermions and the conduction electrons. A standard way to then describe the possible hybridization between the valence fermions and conduction electrons is through a Hubbard-Stratonovich decoupling of the quartic interaction [125, 14, 138, 139]

$$J_K \sum_{r,\alpha,\beta} (\vec{S}_r \cdot c^\dagger_{r,\alpha} \vec{\sigma}_{\alpha\beta} c_{r,\beta}) \to g \sum_{r,\alpha,\beta} (c^\dagger_{r,\alpha} f_{r,\alpha} b_r + \text{H.c.}), \tag{4.3}$$

At the mean-field level the “slave boson” b_r is equal to the hybridization $\langle \sum_\alpha c_{r,\alpha} f^\dagger_{r,\alpha} \rangle$. Note that in this convention the Abrikosov fermion $f^\dagger$ creates a hole in the valence band, while $b^\dagger$ creates a bound singlet consisting of a conduction electron and a valence spin. Thus, the constraint ensuring a single valence spin per site is

$$\sum_\alpha f^\dagger_{r,\alpha} f_{r,\alpha} - b^\dagger_r b_r = 1. \tag{4.4}$$

The constraint can be implemented by a Lagrange multiplier acting as the time component of a $U(1)$ gauge field. Upon renormalization, the gauge field is expected to become dynamical. The matter fields, *i.e.* the b bosons and f fermions carry charges 1 and -1 respectively under this emergent gauge field. Note that under our gauge choice the boson $b^\dagger$ carries the same physical charge as the conduction electron, while the fermion has no physical charge. The low temperature states represent phases of the emergent $U(1)$ gauge theory coupled to matter fields [138, 139, 52].

The FL* phase, characterized by a small FS, the boson is gapped and the gauge theory is in the deconfined phase. The heavy FL phase with a large Fermi surface is established at a QCP at which the boson b condenses, thereby confining the gauge field through the Higgs mechanism.

Condensation of the valence fluctuations provides a simple understanding for the main features of the heavy FL phase [45, 82, 7]. As evident from (4.3), the condensed boson hybridizes the f fermions with the conduction electron. Thus, the Fermi surface must grow to encompass the full density of conduction and valence electrons. The coherent mixing between the mobile conduction electrons with the localized f spinons also explains the large effective mass, which is the hallmark of the heavy FL phase. However, an exact description of the aforementioned Higgs transition within this model is in general hard, as it involves fluctuating gauge fields coupled to multiple matter particles. The standard approach to make analytic progress in the valence fluctuation theory has been to artificially enlarge the $su(2)$ spin symmetry to $su(N)$, and take the large N limit. The large number N of c and f fermion species, controls an exact saddle point solution equivalent to a static mean-field theory, where $b_r = \langle \sum_\alpha c_{r,\alpha} f^\dagger_{r,\alpha} \rangle$ is obtained self-consistently [10, 36, 14]. Because the critical fluctuations of the boson and the gauge field are suppressed, the conduction electrons remain non-interacting, or at least good quasiparticles. Hence, this large N limit is not a good starting point for obtaining non-trivial critical transport properties, and in particular, the strange metal phenomenology that we want to describe. The main point of this paper is to introduce a new large N limit that retains solubility of the problem yet describes non-quasiparticle physics already at the saddle point level. The most important difference between our approach and the previous large N theories is that we keep the fermion spin indices σ $su(2)$ instead of promoting them to $su(N)$, and instead endow all three species c, f, b with a flavor index $i = 1, \ldots, N$. The large N modification we make then is:

$$c_\sigma, f_\sigma, b \to c_{i,\sigma}, f_{i,\sigma}, b_i, \quad i \in 1, \ldots, N, \quad \sigma \in 1, 2. \tag{4.5}$$

One can also continuously vary the ratio of the numbers of flavors of each particle type, however here we fix the same N for all particles. Because all the species have a comparable number of flavors, their self-energies all remain $\mathcal{O}(1)$ within the large N limit.

The second new feature in our generalized large N limit is the introduction of a random ensemble of interaction constants, similar to recently studied “low-rank” SYK models, which involve fermions with random Yukawa coupling to bosons [22, 111, 100, 157, 47, 75, 74]. The random interactions should be viewed as a mathematical construct implementing a particular type of controlled large N

limit. We therefore consider the following family of model Hamiltonians;

$$\begin{aligned} H &= \sum_{\lambda\in\{c_\sigma, f_\sigma, b\}} H_\lambda + H_{\text{int}}, \\ H_\lambda &= \sum_{i=1}^{N}\sum_{k}(\epsilon_{\lambda,k}-\mu_\lambda)\lambda^\dagger_{k,i}\lambda_{k,i}, \\ H_{\text{int}} &= \frac{1}{N}\sum_{i,j,l=1}^{N}\sum_{r,\sigma}(g^r_{ijl}c^\dagger_{r,i,\sigma}f_{r,j,\sigma}b_{r,l}+\text{H.c.}), \\ \sum_{i=1}^{N}&\left(b^\dagger_{r,i}b_{r,i}-\sum_\sigma f^\dagger_{r,i,\sigma}f_{r,i,\sigma}\right) = N\kappa. \end{aligned} \tag{4.6}$$

Here g^r_{ijl} are complex Gaussian random variables. We have included emergent dispersions $\epsilon_{\lambda,k}$ for $\lambda = f_\sigma, b$, which are expected to be generated when integrating out higher energy modes. The last line of (4.6) is the large N generalization of the occupancy constraint in (4.4) (κ is a free parameter).

We consider two models for the coupling tensors g^r_{ijl}. In Model I these are taken to be uncorrelated between different sites r, whereas they are identical on all sites in Model II:

$$\begin{aligned} \text{Model I:}\quad & \overline{g^r_{ijl}\,g^{r'}_{i'j'l'}} = g^2\delta_{rr'}\delta_{ii'}\delta_{jj'}\delta_{ll'}, \\ \text{Model II:}\quad & \overline{g^r_{ijl}\,g^{r'}_{i'j'l'}} = g^2\delta_{ii'}\delta_{jj'}\delta_{ll'}. \end{aligned} \tag{4.7}$$

Thus, Model I is spatially disordered, and should be viewed as a depiction of HFMs with spatially disordered Kondo couplings. Model II, on the other hand, is translationally invariant and should be viewed as a model for clean systems. The averaging over flavors in both models eliminates various intractable Feynman diagrams [99, 47, 74], thus allowing controlled access to the QCP at strong coupling.

While the f and b are also additionally coupled to the emergent $U(1)$ gauge field a, the coupling constant scales as $1/\sqrt{N}$: $H_{\lambda a} \sim (a/\sqrt{N})\sum_{i=1}^{N}\lambda^\dagger_i\lambda_i$, for $\lambda = f, b$. This ensures that the gauge field fluctuations do not contribute to the f, b self-energies in the large N limit. Nonetheless, integrating out the emergent gauge field propagator leads to exact Ioffe-Larkin constraints on the current correlators [64, 87], tantamount to imposing series addition of the conductivities of f, b (Appendix 4.9).

In both models we assume simple quadratic dispersions $\epsilon_\lambda = k^2/(2m_\lambda)$ for all three species $\lambda = c, f, b$. We choose the masses m_λ to be appropriate for the creation of a heavy FL phase upon condensing the bosons, which implies that the mass of f should be much larger than that of c. Furthermore, since b is a composite particle of c and f, its motion requires the combined motion of c and f that can only occur at higher orders in perturbation theory, and it will therefore have a mass even larger than that of f. We thus take the hierarchy $m_b > m_f \gg m_c$. This choice of masses implies the bandwidths of c and f are large relative to that of b. The c, f chemical potentials are chosen such that the respective densities are close to equal, motivated by stoichiometric considerations, and by an observed near doubling in Hall coefficient across the transition from the heavy FL to FL* in CeCoIn$_5$ [98].

The transition between the FL* and heavy FL phases occurs, as in previous theories, through condensation of the boson b. A natural parameter that can control the transition across the QCP in

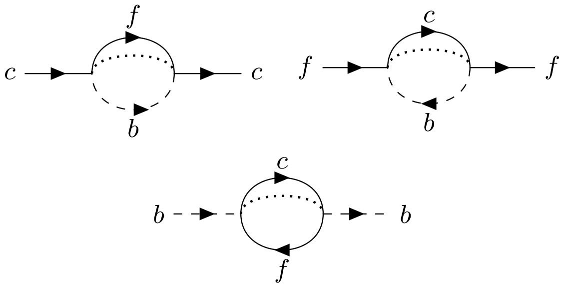

Figure 4.1: The only contributing diagrams to the self-energies of the three particle species. All others are suppressed by the large N limit or averaging over g^r_{ijl}. The averaging over the coupling tensors is indicated by the dotted lines, with its correlator given by (4.7). The dotted lines carry momentum for Model I but do not for Model II.

experiments is the total physical charge density, $n_{el} = \langle n_b \rangle + \langle n_c \rangle$, while the VL occupation and hence $\kappa = \langle n_b \rangle - \langle n_f \rangle$ is held fixed. However, for convenience of calculation we tune κ instead. The two approaches are approximately equivalent in the regime we consider, where the bandwidths of c and f are much larger than that of b, with the difference between the approaches amounting only to small relative changes in the c, f occupations, which only make small changes in the physical properties of c, f, and therefore will not significantly alter our results.

As in the case of previous work on SYK-like models [99, 47, 74], the averaging over the coupling tensors in the large N limit yields exact coupled Schwinger-Dyson (SD) equations for the Green's functions of the three species c, f, b, which we solve self-consistently throughout the phase diagram. The self-energies for these SD equations are shown in Fig. 4.1. Using these, we compute non-perturbatively the T-dependent conductivity tensors in the two models, focusing in particular, on the critical regime.

In the analysis of Model I, we assume a special FL* phase, in which the emergent gauge field, and thus also the f and b particles that are charged under it, are all deconfined only within individual 2D planes. The physical 3D system is a stack of these 2D layers. The behavior of the resistivity across the transition between the layered FL* and the heavy FL phase is shown in Fig. 4.2(a). In the quantum critical regime ρ_{xx} shows a quasi-linear T dependence (linear with a logarithmic correction).

The nature of the critical MFL depends on a dimensionless coupling strength γ between the bosons and fermions. For sufficiently strong coupling, the bosons are overdamped, and the QCP displays a near-universal "Planckian" transport lifetime $\tau \sim \hbar/(k_B T)$, which is independent of all microscopic details of the model (up to logarithmic factors). In the opposite regime of weak damping ($\gamma \ll 1$), the critical behavior provides an example of a skewed MFL [53], in which the scattering rates of particle and hole excitations about the electron FS are different. The resistivity is linear in T but sub-Planckian, and the fermion self-energies are asymmetric about $\omega = 0$. On tuning across the QCP, the in-plane Hall coefficient R_H computed for weak out-of-plane magnetic fields transitions between two plateau values that correspond to the different effective carrier densities of the FL* and FL phase. In the weakly damped regime this change of R_H is non-monotonic, developing a peak in the quantum critical region as a function of the tuning parameter κ (Fig. 4.2(b)). This enhancement of R_H near criticality is reminiscent, yet much more modest than that observed in experiments on CeCoIn$_5$ [98].

For Model II, we consider a fully 3D deconfined FL* phase. We show that ρ_{xx} is quasi-linear in T in the critical region if the f FS at the QCP matches that of the conduction electrons, and if the f fermions and b bosons additionally rapidly relax momentum via impurity scattering and/or self-interactions on the lattice. This is closely related to the work of Paul et. al. [115], who find a MFL for matching FS's coupled to a complex bosonic field under certain phenomenological assumptions. Within Model II however, this result is exact in the large N limit. We further show that the two FS's may be naturally self-tuned to matching at the QCP, in order to maximize the free energy released when the bosons condense. Unlike in Model I, we find that the bosons in Model II are always overdamped, leading to Planckian transport lifetime at low temperatures independent of the coupling strength. Because of the overdamped nature of the bosons there is no enhancement of R_H in Model II.

4.3 Model I: Spatially Disordered Couplings

In this section we solve for the Green's functions in Model I and calculate transport temperature dependence of transport quantities across the transition. We identify two regimes of the critical behavior, depending on the boson-fermion coupling strength. The calculation is exact in the large N limit.

4.3.1 Self-Energies and Phase Diagram

The starting point for obtaining the phase diagram and calculating the transport properties in this model at large N are the coupled Schwinger Dyson equations for the Green's functions of the three species:

$$\begin{aligned} G_c(i\omega) &= \frac{1}{V}\sum_k \frac{1}{i\omega - \epsilon_{c,k} + \mu_c - \Sigma_c(i\omega)}, \\ G_f(i\omega) &= \frac{1}{V}\sum_k \frac{1}{i\omega - \epsilon_{f,k} + \mu_f - \Sigma_f(i\omega)}, \\ G_b(i\omega) &= \frac{1}{V}\sum_k \frac{1}{-i\omega + \epsilon_{b,k} + \Delta_b - \Sigma_b(i\omega)}, \end{aligned} \tag{4.8}$$

where V is the system volume. The self-energies $\Sigma_{c,f,b}$ in the large N limit are given exactly by the diagrams in Fig. 4.1, which read

$$\begin{aligned} \Sigma_c(i\omega) &= g^2 T \sum_{i\omega'} G_f(i\omega') G_b(i\omega - i\omega'), \\ \Sigma_f(i\omega) &= g^2 T \sum_{i\omega'} G_c(i\omega') G_b(i\omega' - i\omega), \\ \Sigma_b(i\omega) &= -2g^2 T \sum_{i\omega'} G_c(i\omega') G_f(i\omega' - i\omega). \end{aligned} \tag{4.9}$$

Here V is the system volume, and the factor of 2 in the equation for Σ_b arises from the $su(2)$ spin degeneracy of c and f. The self-energies only involve momentum-averaged Green's functions $G_\lambda(i\omega) = (1/V)\sum_k G_\lambda(i\omega, k)$ because the random interactions in Model I are uncorrelated between different sites. In the relevant regime where the fermion bandwidths are the largest scales, their momentum-averaged Green's functions take the simple form $G_{c,f}(i\omega) = -(i/2)\nu_{c,f}\,\mathrm{sgn}(\omega)$ [114], where $\nu_{c,f}$ are the respective spinless densities of states at the Fermi energies. This allows to calculate the boson self-energy Σ_b

$$\begin{gathered}\Sigma_b(i\omega) = -2g^2T\sum_{i\omega'} G_c(i\omega')G_f(i\omega' - i\omega) = -\gamma|\omega| + C_b,\\ \gamma = g^2\nu_c\nu_f/(2\pi) = g^2(3n_c)^{1/3}m_c m_f/(2\pi^{4/3}).\end{gathered} \tag{4.10}$$

Here γ is a dimensionless coupling constant characterizing the strength of the boson damping. We will explain the effects of its magnitude on the physics of the system in the subsequent paragraphs. The T-independent constant C_b can be absorbed by the $T = 0$ chemical potential of the bosons.

With the Green's functions in hand, the phase diagram is obtained by solving for the boson gap $\Delta_b(T)$ and the fermion chemical potential $\mu_f(T)$ that would satisfy the constraint $\langle n_b\rangle - \langle n_f\rangle = \kappa$. In the relevant regime of large fermion bandwidth (or Fermi energy) compared to the temperature, the change in the fermion occupation with temperature is negligible. Therefore fixing κ is essentially equivalent to fixing the boson occupation

$$\langle n_b\rangle = T\sum_{\omega} G_b(i\omega) = \kappa + \langle n_f\rangle, \tag{4.11}$$

where $\langle n_f\rangle$ is treated as a constant. The phase transition, associated with condensation of the boson, is then tuned by the parameter κ, analogous to the fixed length constraint in the $O(N)$ rotor model at large N [131]. Similar to the rotor model, the boson occupation is fixed by solving for the variation of the "soft gap" $\Delta_b(T)$ in the boson Green's function (4.9) with temperature.

The defining features of the zero temperature phases tuned by κ are shown in Fig. 4.2(c). In the FL* phase, obtained for $\kappa < \kappa_c$, the zero temperature gap $\Delta_b(0)$ is positive and vanishes continuously as κ approaches the critical value κ_c. For $\kappa > \kappa_c$, on the other hand, one of the boson flavors is condensed at $T = 0$ and acquires a condensate amplitude $|\langle b_{r,1}\rangle| = r_0\sqrt{N}$. This leads to the hybridization of the f and c fermion bands, which characterizes the heavy FL phase. Details of the calculation are given in Appendix 4.7.

The temperature dependence of the soft gap $\Delta_b(T)$ is crucial for determining the thermodynamic and transport properties. Solving the constraint equation at criticality we find that soft gap grows quasi-linearly with temperature as $\Delta_b(T) \sim Tw_1(\gamma, T)$, where w_1 varies quasi-logarithmically with T [1]. Details of the calculation are given in Appendix 4.8. In the $FL^\star$ phase ($\kappa < \kappa_c$) $\Delta_b(T)$ exhibits the critical behavior for $T \gg \Delta_b(0)$, while its temperature dependence is exponentially suppressed for $T \ll \Delta_b(0)$.

In the heavy FL phase ($\kappa > \kappa_c$) the temperature dependence of Δ_b is more subtle because the b and f fermions are no longer confined to hop within planes in this phase. Once a condensate is established, the inter-layer interactions generate inter-layer hopping terms of the b and f partons of

---

[1] The function $w_1(\gamma, T)$ vanishes quasilogarithmically as $T \to 0$, diverges logarithmically as $\gamma \to 0$, and is quasi-linear in γ for $\gamma \gg 1$

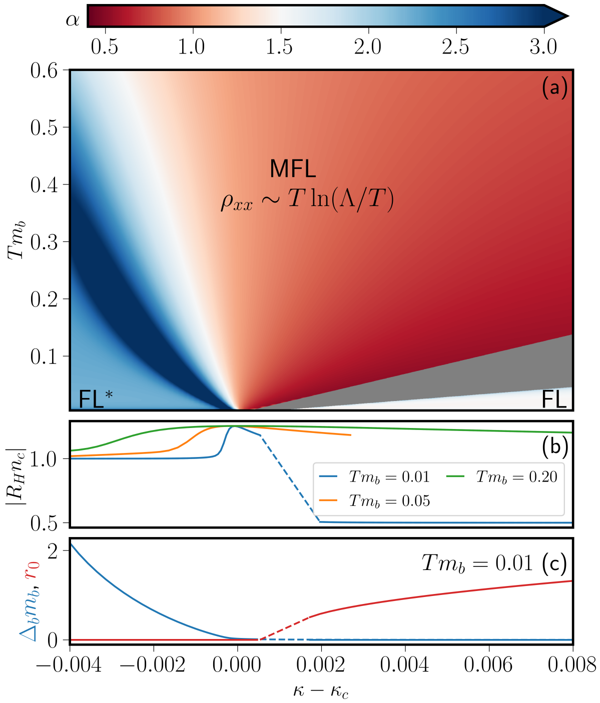

Figure 4.2: (a) The phase diagram for Model I. We have $\rho_{xx} - \rho_{xx}(T=0) \sim T^\alpha \ln(\Lambda/T)$, and the color indicates the value of $\alpha = d\ln(\rho_{xx}/\ln(\Lambda/T))/d\ln(T)$. We exclude the (gray) crossover region where our approximate treatment of the 3D condensed phase breaks down. (b) The plot of R_H at weak out-of-plane magnetic field vs. $\kappa - \kappa_c$. R_H transitions non-monotonically between two plateau values controlled by the effective carrier densities in the FL* and heavy FL phases respectively. The value of R_H is enhanced in the quantum critical region. The dashed lines indicate points within the gray region that are omitted. Due to the different dimensionality of f and c, the plateau value on the right is only roughly $1/(n_c + n_f)$. (c) The boson "soft gap", $\Delta_b m_b$, and the strength of the boson condensate, $\langle b_{r,1}\rangle = r_0\sqrt{N}$, are plotted vs. $\kappa - \kappa_c$ at low temperature. Δ_b is finite when $\kappa < \kappa_c$ and is exponentially suppressed when $\kappa > \kappa_c$, at which point inter-layer instabilities allow for a 3D boson condensate to form, forcing $\Delta_b = 0$. Again, we omit the crossover between these two regimes (gray region). Here $\gamma = 0.02 \ll 1$, $n_c = n_f = 1$, $\Lambda m_b = \pi^2/2$, $m_b = 5m_f = 50m_c$ (we set $\hbar = k_B = a_l = 1$ everyhwere, where a_l is the lattice constant).

strength proportional to r_0^2, thus establishing a fully 3D Higgs phase (for full details see Appendix 4.11). The approximate description of the Higgs phase in terms of a self-consistent 3D condensate remains valid in the heavy FL phase below a crossover temperature scale T^* that vanishes at the QCP. Above the crossover scale T^* the b sector is dominated by 2D critical fluctuations [2]. In

---

[2] As is well known there is no phase transition between the low T Higgs phase and high T confined phase.

computing the transport properties for $\kappa > \kappa_c$ we will treat these two regimes separately, leaving out the more complicated crossover regime (gray region in Fig. 4.2(a)).

We now turn to the fermion Green's functions, showing first that they accquire a MFL self-energy at the QCP. To calculate the fermionic self-energies $\Sigma_{c,f}$ we need the momentum-averaged b Green's function:

$$\begin{aligned} G_b(i\omega) &= \int \frac{d^dk}{(2\pi)^d} \frac{1}{-i\omega + k^2/2m_b + \gamma|\omega| + \Delta_b} \\ &\approx \frac{m_b}{2\pi} \ln\left(\frac{\Lambda}{-i\omega + \gamma|\omega| + \Delta_b}\right), \quad d = 2, \end{aligned} \tag{4.12}$$

where $\Lambda = \pi^2/(2m_b)$ is the boson bandwidth. We always consider sufficiently low frequency and temperature such that $\max(|\omega|, \gamma|\omega|, \Delta_b) \ll \Lambda$. This ensures that self-energies remain smaller than the bandwidths of their respective species and thereby will keep our computations self-consistent. The logarithmic form in (4.12) is only obtained for 2D bosons. The QCP is defined by $\Delta_b = 0$; when inserted into (4.12) and (4.9), we obtain MFL self-energies:

$$\begin{aligned} \Sigma_c(i\omega, T=0) &= g^2 \int \frac{d\omega'}{2\pi} G_f(i\omega') G_b(i\omega - i\omega') \\ = \frac{\gamma m_b}{2\pi\nu_c} &\left[i\omega \ln\left(\frac{\sqrt{1+\gamma^2}}{e\Lambda/|\omega|}\right) + \cot^{-1}(\gamma)|\omega| \right] + C_c. \\ \Sigma_f(i\omega, T=0) &= g^2 \int \frac{d\omega'}{2\pi} G_c(i\omega') G_b(i\omega' - i\omega) \\ = \frac{\gamma m_b}{2\pi\nu_f} &\left[i\omega \ln\left(\frac{\sqrt{1+\gamma^2}}{e\Lambda/|\omega|}\right) - \cot^{-1}(\gamma)|\omega| \right] + C_f. \end{aligned} \tag{4.13}$$

The constants $C_{c,f}$ can be absorbed into $\mu_{c,f}$.

The parameter γ, related to the strength of damping of the b bosons, allows us to tune between different physical regimes. In general we expect γ to increase with the strength of the Kondo coupling g. In the limit of $\gamma \gg 1$, the analytic continuation of (4.13) to real frequency gives

$$\mathrm{Im}[\Sigma_{c,f,R}](\omega, T=0) = -\frac{\gamma m_b}{4\nu_{c,f}} |\omega|, \tag{4.14}$$

which is the traditional MFL form [155]. On the other hand, when $\gamma \ll 1$, the fermion self-energies (4.13) are *asymmetric* about $\omega = 0$:

$$\begin{aligned} \mathrm{Im}[\Sigma_{c,R}](\omega, T=0) &= \frac{\gamma m_b}{2\pi\nu_{c,f}} |\omega| \left(-\frac{\pi}{2} - \cot^{-1}(\gamma)\mathrm{sgn}(\omega)\right), \\ \mathrm{Im}[\Sigma_{f,R}](\omega, T=0) &= \frac{\gamma m_b}{2\pi\nu_{c,f}} |\omega| \left(-\frac{\pi}{2} + \cot^{-1}(\gamma)\mathrm{sgn}(\omega)\right). \end{aligned} \tag{4.15}$$

Thus, in this regime, our model provides a concrete example of a "skewed" MFL [53]. This skewed MFL is expected to have a nonvanishing Seebeck coefficient in the $T \to 0$ limit due to the asymmetric inelastic scattering rate in (4.15) [53, 55]. The nonvanishing Seebeck coefficient as $T \to 0$, and

---

Accordingly, there is no true finite T Bose condensation transition, only a crossover the asymmetric frequency dependence of the electron spectral function, provide experimentally detectable signatures of the small γ regime [3].

In the FL* phase, where $\Delta_b(T=0) > 0$, we obtain, in a similar fashion to (4.13),

$$\begin{aligned}\Sigma_{c,f}(i\omega, T=0) = &-\frac{\gamma m_b \ln(\Lambda/\Delta_b(T=0))}{\pi\nu_{c,f}} i\omega \\ &+ i\frac{\gamma^2 m_b}{2\pi\nu_{c,f}\Delta_b(T=0)}\omega^2. \end{aligned} \tag{4.16}$$

The $\mathcal{O}(\omega^2)$ term leads to a Fermi liquid ω^2 scattering rate on the real frequency axis, and hence a scattering rate $\propto \omega^2 + \pi^2 T^2$ upon analytic continuation to the thermal circle for $T > 0$. The $\mathcal{O}(\omega)$ term leads to a renormalization of the Fermi liquid quasiparticle weights, and hence an enhancement of the conduction electron effective mass, given by

$$m_c^* = m_c\left(1 + \frac{\gamma m_b}{\pi\nu_c}\ln\left(\frac{\Lambda}{\Delta_b(T)}\right)\right). \tag{4.17}$$

Here, we extended the result to small nonvanishing temperatures by replacing $\Delta_b(0) \to \Delta_b(T)$. Since $\Delta_b(T=0) \sim \kappa_c - \kappa$ vanishes on approach to the QCP, the zero temperature effective mass diverges, consistent with experimental findings in HFMs [146, 43]. In the critical region $\Delta_b \propto T$ up to logarithmic corrections. Thus, the divergence of m_c^* is cut-off logarithmically by the temperature at criticality.

We now calculate the imaginary part of the fermion self-energies at finite T, necessary for computing conductivities. The c fermion self-energy in the Lehmann representation is given by:

$$\Sigma_c(i\omega, T) = -g^2 \int \frac{d\epsilon d\epsilon'}{(2\pi)^2} A_f(\epsilon) A_b(\epsilon') \frac{n_B(\epsilon') + n_F(-\epsilon)}{\epsilon' + \epsilon - i\omega}, \tag{4.18}$$

where n_B, n_F are the Bose and Fermi functions at temperature T, $A_f(\epsilon) = -2\text{Im}[G_f^R(\epsilon)] = \nu_f$ is the fermion spectral function, and $A_b(\epsilon)$ the boson spectral function. We analytically continue $i\omega \to \omega + i\delta$ to obtain

$$\text{Im}[\Sigma_{c,R}(\omega, T)] = -g^2\nu_f \int \frac{d\epsilon}{4\pi} A_b(\epsilon)(n_B(\epsilon) + n_F(\epsilon - \omega)). \tag{4.19}$$

This expression also holds for $\text{Im}[\Sigma_{f,R}]$ with the change $\nu_f \to \nu_c$ and $\omega \to -\omega$. The boson spectral function is derived in Appendix 4.7 and is given by:

$$A_b(\omega) = \frac{m_b}{\pi}\left[\pi\Theta(\omega - \Delta_b) + \tan^{-1}\left(\frac{\gamma\omega}{\Delta_b - \omega}\right)\right], \tag{4.20}$$

where $\Theta(x)$ is the Heaviside step function. Note that the temperature dependence of A_b comes entirely from its dependence on $\Delta(T)$. We have shown that in the critical region $\Delta_b \propto T$ up to logarithmic corrections. Therefore, up to these corrections, the spectral function can be expressed as $A_b(\omega/T, z)$, with $z = \Delta_b/T$ a temperature independent constant. Using this expression in (4.19) and

---

[3] The magnitude of the low-temperature Seebeck coefficient is $\sim k_B/e$ when $\gamma \ll 1$, declining to zero as γ is increased to $\gamma \gg 1$.

scaling the integration variable immediately gives a T-linear result up to the logarithmic corrections. We will show that this property implies near T-linearity of the resistivity.

In the two limits $\gamma \gg \max(1, \Delta_b/T)$ and $\gamma \ll 1$ we obtain explicit expressions for the imaginary parts of the self-energy in the critical region (Appendix 4.8). For large γ we have

$$\begin{aligned}\mathrm{Im}[\Sigma_{c,R}(\omega,T)] \approx -\frac{\gamma m_b}{2\pi\nu_c}T\Bigg[&\frac{\Delta_b}{\gamma T}\ln\left(\frac{\Lambda e}{\Delta_b}\right)\\ &+\pi\ln\left(2\cosh\left(\frac{\omega}{2T}\right)\right)\Bigg];\ \Delta_b/(\gamma T)<1,\end{aligned}$$

$$\Delta_b \approx \frac{\pi\gamma T}{\ln\left(\frac{\Lambda}{T\gamma e}\right)}W_0\left(\frac{2\sqrt{e}}{\pi^2}\ln\left(\frac{\Lambda}{T\gamma e}\right)\right), \tag{4.21}$$

where $W_0(z)$ is the Lambert W function. For $\gamma \ll 1$, (4.13) is well approximated by:

$$\mathrm{Im}[\Sigma_{c,R}(\omega,T)] \approx -\frac{\gamma^2 m_b}{2\pi\nu_c}T\left(1+e^{\omega/T}\right),\ |\omega| \lesssim T. \tag{4.22}$$

Like at $T = 0$ (4.15), this self-energy is asymmetric between positive and negative frequencies, and is therefore skewed.

4.3.2 Conditions for Planckian Dissipation

It has been proposed that inelastic relaxation times, in most if not all situations, cannot be much smaller than the quantum mechanical "Planckian" time scale $\tau_P = \hbar/(k_B T)$ (see [60] and references therein). There is a growing list of materials, showing strange metal behavior at low temperatures, which seem to be close to this limit, namely they relax on the Planckian time scale up to a constant of order one [27, 89, 104, 28, 113]. Since the self-energies calculated above imply relaxation times proportional to $1/T$, it is interesting to ask how systems described by Model I line up with the proposed Planckian bound.

Note however, that the correct quasiparticle relaxation time cannot be extracted directly as the inverse $\mathrm{Im}\Sigma_R$. Rather it is renormalized by the same factor as the mass. To see this, we eliminate the prefactor of the ω term to obtain the standard Fermi liquid form of the Green's function

$$G_{c,R}(\omega,k) = \frac{Z}{\omega - Z\xi_k - iZ\mathrm{Im}\left[\Sigma_{c,R}(\omega)\right]} \tag{4.23}$$

with $Z = m/m_c^*$. From this we can immediately obtain $1/\tau_c = Z\,\mathrm{Im}\left(\Sigma_{c,R}(\omega=0)\right)$. This is the same timescale extracted from analysis of transport data pertaining to strange metal QCPs [27, 89, 104, 28, 113] using the Drude formula for quasi particle transport $\tau = m^*\sigma_{xx}/(ne^2)$. In the experiments the effective quasiparticle mass is measured slightly away from the critical point. Note that we focus here on the relaxation rates of the conduction electrons because, as shown in Sec. 4.3.3 below, they dominate the transport.

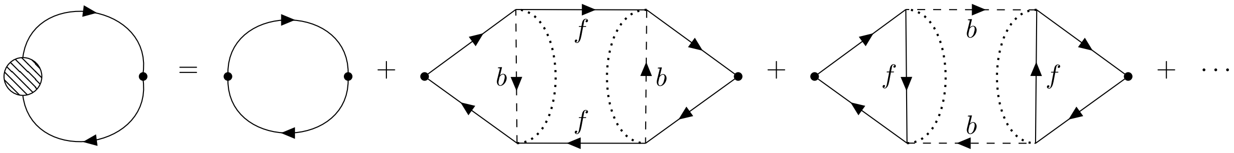

Figure 4.3: The diagrams that contribute to the c conductivity. These diagrams are not suppressed by the large N limit, but only the first (bubble) diagram is nonzero in Model I; in Model II, the corrections to the bubble do not identically vanish, but their effects are nevertheless suppressed (see main text). As in Fig. 4.1, dotted lines indicate the averaging over the flavor random couplings g^r_{ijl}, which carry momentum in Model I (but not in Model II). Consequentially, the momentum integrals in the left and right loops of the correction diagrams are decoupled only in Model I. The diagrams that contribute to the f and b conductivities are analogous to the ones above. The diagrams that contribute to the cross-correlations of currents of different species are analogous to the vertex diagrams correcting the bubble diagram above, and also vanish in Model I (but not in Model II).

In the strongly damped regime, where $\gamma \gg 1, \Delta_b/T$, equations (4.17) and (4.21) give

$$\begin{aligned}\tau_c &= \left(\frac{\pi\nu_c}{\gamma m_b} + \ln\left(\frac{\Lambda}{\gamma T}\right)\right)\frac{\hbar}{k_B T} \\ &\approx \ln\left(\frac{\Lambda}{\gamma T}\right)\frac{\hbar}{k_B T},\end{aligned} \tag{4.24}$$

At realistic temperatures τ_c can be viewed as Planckian relaxation modified only by a slowly varying logarithmic function of temperature and nearly independent of the microscopic couplings. The result provides an appealing potential explanation for observation of near Planckian relaxation across different materials, with $\mathcal{O}(1)$ proportionality constants that vary only slightly between materials [27].

In the weakly damped regime $\gamma \ll 1$ equations (4.17) and (4.22) give

$$\tau_c = \frac{1}{\gamma}\left(\frac{\pi\nu_c}{\gamma m_b} + \ln\left(\frac{\Lambda}{T\ln(\pi/\gamma)}\right)\right)\frac{\hbar}{k_B T}, \tag{4.25}$$

which is manifestly nonuniversal. The proposed Planckian lower bound is still obeyed, but exceeded by a large factor of at least $1/\gamma$. Thus we do not expect Planckian transport in the weak damping regime. Such “sub-Planckian” behavior has in fact recently been reported in experiments on HFMs [152].

4.3.3 Transport

The computation of transport properties is greatly simplified in Model I due to the spatially disordered coupling g^r_{ijl}. To clarify this point, let us first ignore the effects of the emergent $U(1)$

gauge field. In this case the Kubo formula for Model I takes a particularly simple form involving only the bare bubble diagram for each of the three species (the first diagram in the series shown in Fig. 4.3). To see this, first note that only vertex corrections with non-crossing boson lines can potentially contribute in the large N limit. However, in such diagrams, the momentum integral on the loop containing the bare current vertex is decoupled from the rest of the diagram due to averaging over the site-uncorrelated couplings g^r_{ijl}. Once decoupled, these loop integrals vanish because the current vertices and the propagators on the loop have opposite parities under spatial inversion. Note that all cross species current correlations must involve vertex corrections, which vanish by the same mechanism. Thus, the conductivities associated with the different species can be separately calculated from their respective bubble diagrams. Physically, these diagrams describe current decay due to scattering of fermions on critical bosons, which is not momentum conserving due to the spatially disordered couplings.

The effects of the emergent $U(1)$ gauge field on transport can now be included by integrating it out exactly in the large N limit. This leads to a Ioffe-Larkin composition rule for the in-plane conductivities of the three species, described by the respective bubble diagrams (see Appendix 4.9) [64, 87]:

$$\boldsymbol{\sigma} = \begin{pmatrix} \sigma_{xx} & \sigma_{xy} \\ -\sigma_{xy} & \sigma_{yy} \end{pmatrix} = \boldsymbol{\sigma}_c + (\boldsymbol{\sigma}_b^{-1} + \boldsymbol{\sigma}_f^{-1})^{-1} \equiv \boldsymbol{\sigma}_c + \boldsymbol{\sigma}_{bf}. \tag{4.26}$$

In other words, the conductivities of the f fermions and the bosons, which carry a $U(1)$ gauge charge, are added in series and their combined current is added in parallel to that of the conduction electrons.

The transport properties of the two phases can be easily understood from this composition rule. In the heavy fermi liquid phase, obtained for $\kappa > \kappa_c$, the boson is condensed and therefore contributes zero resistance to the in-series addition. The total conductivity is then a result of adding the f and c fermions currents in parallel, consistent with the expected increase of the carrier number associated with the large Fermi surface. In the FL* phase, obtained for $\kappa < \kappa_c$, the boson conductivity vanishes at zero temperature due to the soft gap. The combined conductivity of the bosons with the f fermions also vanishes due to the series addition. Therefore the total conductivity is equal to just that of the conduction electrons $\boldsymbol{\sigma} = \boldsymbol{\sigma}_c$, compatible with a small fermi surface consisting of only those electrons.

We now argue that in the quantum critical region at finite temperatures the transport is also dominated by the conduction electrons. To obtain the boson contribution σ_b, note that in the critical regime we have $\Delta_b(T) \sim T$ (up to logarithms), which retains the scaling of the Green's function as $1/\omega$. A simple scaling analysis of the bubble diagram then shows that $\boldsymbol{\sigma}_b \sim T^0$, much smaller than $\sigma_f \sim 1/T$. Thus, the small boson conductivity bottlenecks the series addition with the spinons. Then the total conductivity is dominated by the much larger $\sigma_c \sim 1/T$ added in parallel. We confirm by exact numerical evaluation that indeed the total conductivity in the critical region is dominated by the conduction electrons (Fig. 4.4 inset).

The longitudinal resistivity of the conduction electrons, derived from the bubble diagram in Fig. 4.3, takes the form [114] (see also Appendix 4.6):

$$\rho_{c,xx} = T \left(\frac{n_c}{8m_c} \int_{-\infty}^{\infty} d\omega \frac{\mathrm{sech}^2(\omega/(2T))}{|\mathrm{Im}[\Sigma_{c,R}(\omega, T)]|} \right)^{-1}. \tag{4.27}$$

In the critical region $\mathrm{Im}[\Sigma_{c,R}(\omega,T)] \sim T$ for $|\omega| \lesssim T$, so that the integral in (4.27) is independent of T at leading order. Thus we get nearly T-linear resistivity in the critical strange metal.

In the FL* phase we found in (4.16) that $|\mathrm{Im}[\Sigma_{c,R}(\omega,T)]| \propto \omega^2 + \pi^2 T^2$. Plugging this into (4.16) gives $\rho_{xx} \propto T^2$ as in a normal Fermi liquid (Fig. 4.2(a)).

In the heavy FL phase, the boson conductivity diverges due to the condensation of $\langle b_{r,1}\rangle \sim r_0\sqrt{N}$ and the Ioffe-Larkin composition rule therefore implies the parallel addition of the c and f conductivities. The condensate also generates inter-layer hopping of the bosons and spinons, which in return stabilize the condensate, within this mean-field treatment, at nonvanishing low temperatures. Details of this self-consistent model are described in Appendix 4.11.

Note that the c and f fermions continue to couple to the $N-1$ uncondensed gapless boson flavors $b_{2,\dots,N}$. The 3D boson dispersion for $b_{2,\dots,N}$ implies that we must compute the equivaluent of (4.12) with an additional integral over the out-of-plane momentum, which leads to it having a $\omega^{1/2}$ frequency dependence (instead of $\ln(\omega)$), and subsequently to $\mathrm{Im}[\Sigma_{c,f,R}] \sim \mathrm{const.} + \max(T^{3/2}, \omega^{3/2})$. This results in a resistivity that behaves as $\rho_{xx} \sim \mathrm{const.} + T^{3/2}$ at low T as seen in Fig. 4.2(a), where the constant contribution to $\mathrm{Im}[\Sigma_{c,f,R}]$ (and therefore ρ_{xx}) is generated by scattering off of the condensed b_1 mode. The $N-1$ uncondensed boson modes leading to the $T^{3/2}$ correction exist only as an artifact of the large N limit, and they will not be present in the physical $N=1$ limit. Therefore, in the physical system we expect the finite T corrections to the resistivity in the heavy FL phase to be weaker than $T^{3/2}$.

At nonzero out-of-plane magnetic fields, $B \neq 0$, $\boldsymbol{\sigma}$ may be computed by expressing the Kubo formula in the basis of Landau levels, since the local self-energies are spatially independent. Vertex corrections to the current correlation functions continue to vanish even when $B \neq 0$ (Appendix 4.6). As a result of integrating out the emergent $U(1)$ gauge field, the in-plane $\boldsymbol{\sigma}_{b,f}$ are computed in presence of renormalized magnetic fields produced by the response of the emergent $U(1)$ gauge field to the (weak) external magnetic field B (Appendix 4.9):

$$B_f = B\frac{\chi_b}{\chi_f + \chi_b},\ \ B_b = B\frac{\chi_f}{\chi_f + \chi_b}. \tag{4.28}$$

Here χ_y is the diamagnetic susceptibility for species y. We set $\chi_f = 1/(24\pi m_f)$, *i.e.* the free fermion Landau diamagnetic susceptibility, corrections to which are suppressed by the large f bandwidth (see Appendix 4.10), and χ_b to its zero field value as we are only concerned with small B.

In the FL* phase and the quantum critical region, since the transport is dominated by the conduction electrons as discussed above, we can express the weak-field Hall coefficient as

$$\begin{aligned} R_H \approx R_H^c &= \frac{\sigma_{c,xy}}{(\sigma_{c,xx})^2} \\ &= -\frac{4T}{n_c}\frac{\int_{-\infty}^{\infty} d\omega\,\mathrm{sech}^2\left(\omega/(2T)\right)\mathrm{Im}[\Sigma_{c,R}(\omega,T)]^{-2}}{\left(\int_{-\infty}^{\infty} d\omega\,\mathrm{sech}^2\left(\omega/(2T)\right)\mathrm{Im}[\Sigma_{c,R}(\omega,T)]^{-1}\right)^2}. \end{aligned} \tag{4.29}$$

When $\mathrm{Im}[\Sigma_{c,R}(\omega,T)]$ is independent of ω, we get $R_H \approx -1/n_c$. Thus an enhancement of R_H beyond this value requires a strong frequency dependence of $\mathrm{Im}[\Sigma_{c,R}(\omega,T)]$ at $|\omega| \lesssim T$, as otherwise R_H would be independent of the self-energy. In the FL* phase, $\mathrm{Im}[\Sigma_{c,R}(\omega,T)] \propto \omega^2 + \pi^2T^2$, and $R_H \approx -1.05/n_c$. We find that in the quantum critical region, for weak damping $\gamma \ll 1$, $R_H \approx -4/(3n_c)$, which can be obtained by inserting (4.22) into (4.29). Therefore, there is an

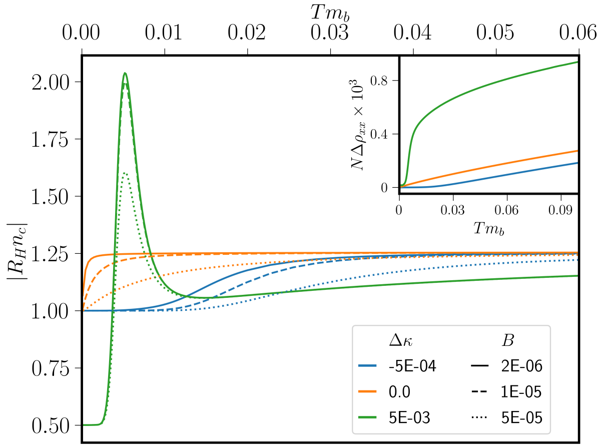

Figure 4.4: R_H vs. T in Model I for various B and $\Delta\kappa = \kappa - \kappa_c$, computed numerically without any approximations. R_H is roughly constant within the critical region and is higher than the expected $R_H \approx -1/n_c$ seen in the FL* region (blue and orange curves). A larger B suppresses R_H slightly. There is a large enhancement in the crossover region between the condensed bosons and the quantum critical region, when we ignore inter-layer instabilities for $\kappa > \kappa_c$ (green curve). (Inset) $\Delta\rho_{xx} \equiv \rho_{xx} - \rho_{xx}(T = 0)$ vs. T for different values of $\Delta\kappa$. The other parameters are the same as in Fig. 4.2.

enhancement of R_H upon entering the quantum critical region from the FL* phase. In the strongly damped $\gamma \gg 1$ regime, the frequency dependence of $\mathrm{Im}[\Sigma_{c,R}(\omega, T)]$ in the quantum critical region (4.21) is weaker than that in (4.22), and consequently $R_H \approx -1.07/n_c$ in the quantum critical region, which is a negligible enhancement over the FL* phase. In Fig. 4.4 we demonstrate the enhancement of R_H for $\gamma \ll 1$, seen when crossing from the FL* phase to the quantum critical region as a function of T, by computing the total conductivity numerically without any approximations. The enhancement of R_H is suppressed by magnetic field and sharpened (as a function of κ) with decreasing temperature. 4.2(b) shows the enhancement of R_H in the crossover between the two regimes as a function of the tuning the parameter κ at constant temperature. This enhancement is more modest than that observed in experiments on CeCoIn$_5$ [98].

We have noted already that upon tuning κ into the heavy FL phase ($\kappa > \kappa_c$), the total conductivity tensor is simply $\sigma_c + \sigma_f$, because the boson is superconducting and connected in series to the f. Moreover, in the presence of an external magnetic field, the Meissner effect generated by the superconducting boson leads to a divergent susceptibility χ_b that screens the magnetic field seen by the boson, while the f fermions see the full magnetic field up to the small Landau diamagnetism. Consequently the Hall effect is just as it would be for a Fermi liquid composed of both the c and f fermions, $|R_H|n_c = n_c/(n_c + n_f) = 1/2$. Thus, as seen in Fig. 4.2(b), $|R_H|n_c$ changes from ≈ 1 in the FL* phase to $\approx 1/2$ in the heavy FL phase.

Note, however that the calculation performed to obtain these plots is interrupted in the grayed out crossover region of Fig. 4.2(a) between the critical and heavy FL regime. We can attempt to capture R_H in this region by continuing the calculation from the critical regime, with the boson fluctuations decoupled between 2D layers, down to low temperatures. In this case we find a strong enhancement of the Hall coefficient over an intermediate temperature window (Fig. 4.4) in the weakly damped $\gamma \ll 1$ regime. The enhancement is dominated by the contribution of the boson conductivity $\boldsymbol{\sigma}_b$ to the total conductivity $\boldsymbol{\sigma}$. The strong non-monotonic behavior stems from a competition between two effects. On the one hand the boson gap decreases rapidly with decreasing temperature and becomes exponentially suppressed below the grayed out crossover regime, $\Delta_b \sim T \exp\left[-\frac{2\pi(\kappa-\kappa_c)}{Tm_b}\right]$. This leads to a large $\sigma_{b,xy}$ due to bosons excited above the small gap. On the other hand, the susceptibility χ_b diverges rapidly ultimately leading to vanishing of B_b and hence also of $\boldsymbol{\sigma}_b$ at zero temperature. The interplay between these two effects leads to the sharp peak in $|R_H|$ versus temperature seen in Fig. 4.4. This strong enhancement is more reminiscent of the experimental results on CeCoIn$_5$ [98].

We note that when the boson is strongly damped, with $\gamma \gg 1$, this mechanism for enhancement of R_H is not effective because the boson becomes nearly particle-hole symmetric with $G_b(i\omega) \approx G_b(-i\omega)$.

4.4 Model II: Translationally Invariant Couplings

In this section we consider the model (4.6) with random tensor couplings that are the *same* on all lattice sites, satisfying $\overline{g^r_{ijl}\, g^{r'}_{i'j'l'}} = g^2 \delta_{ii'}\delta_{jj'}\delta_{ll'}$. We also assume that, in the FL* phase, the $U(1)$ gauge field is fully deconfined in three dimensions. Due to the momentum conservation, the SD equations (with self-energies given by Fig. 4.1) now involve momentum *dependent* (rather than momentum-averaged) Green's functions. We further specialize to the case where the c and f FS match [115], which we will demonstrate is a natural condition. We will then continue to compute the transport quantities in parallel to the analysis of Model I.

4.4.1 Matched Fermi surfaces

We argue that the matching of the FS's of c and f fermions is not as fine tuned a condition as it might appear. First, an equal site occupation $n \approx 1/2$ in both bands is in many cases a natural result of stoichiometry [98]. But though having equal Fermi surface volumes is a necessary condition, it does not necessarily imply matching. A key point is that the f fermions are emergent degrees of freedom (partons), whose dispersion is generated dynamically, unlike the dispersion of the c which is fixed by microscopic material parameters. Below we argue that the dynamical variable that controls the dispersion of the f fermions self tunes to match the FS of the c fermions at the critical point as such matching maximizes the free energy relieved by condensation of the b.

To demonstrate the energetic mechanism behind the matching of the FS's, we assume that the c and f FS's are ellipsoidal, with the dispersions

$$\begin{aligned} \epsilon_{c,k} &= \frac{k_x^2}{2m_{c,x}} + \frac{k_y^2}{2m_{c,y}} + \frac{k_z^2}{2m_{c,z}}, \\ \epsilon_{f,k} &= \frac{k_x^2}{2m_{f,x}} + \frac{k_y^2}{2m_{f,y}} + \frac{k_z^2}{2m_{f,z}}, \end{aligned} \tag{4.30}$$

and that they have the same volume

$$\begin{aligned} V_{\mathrm{FS}} &= \mu_c^{3/2}\sqrt{2m_{c,x}m_{c,y}m_{c,z}}/(3\pi^2) \\ &= \mu_f^{3/2}\sqrt{2m_{f,x}m_{f,y}m_{f,z}}/(3\pi^2). \end{aligned} \tag{4.31}$$

The ratios $r_{\alpha=\{c,f\};\beta=\{y,z\}} = m_{\alpha,\beta}/m_{\alpha,x}$ control the shape of the Fermi surfaces. We will treat the parameters of the f dispersion as variational parameters that minimize the ground state energy of the system upon boson condensation. When the boson is uncondensed, the grand free energy of the non-interacting fermion system at $T = 0$ is $F_0 = -(2/5)V_{\mathrm{FS}}(\mu_c+\mu_f)$, not taking into account the fluctuations of the bosons. Upon condensing $b \to b_0$, and ignoring the remaining boson fluctuations, the mean-field Hamiltionian is

$$\begin{aligned} H_0 = \sum_{k,\sigma} &\Big[(\epsilon_{c,k} - \mu_c)\, c^\dagger_{k,\sigma}c_{k,\sigma} + (\epsilon_{f,k} - \mu_f)\, f^\dagger_{k,\sigma}f_{k,\sigma}\Big] \\ &+ b_0 \sum_{k,\sigma}\Big[c^\dagger_{k,\sigma}f_{k,\sigma} + \mathrm{H.c}\Big] + E(b_0), \end{aligned} \tag{4.32}$$

where $E(b_0) \sim -b_0^2 + b_0^4 < 0$ is the grand free energy arising from the purely bosonic part of the Hamiltonian. We then determine the change in grand free energy at $T = 0$ of the two fermion bands produced by diagonalizing the 2×2 c, f Hamiltonian;

$$\begin{aligned} F - F_0 = \sum_{\pm}\int \frac{d^3k}{2\pi^3}\bigg(&(\epsilon_{c,k} - \mu_c) + (\epsilon_{f,k} - \mu_f) \\ &\pm \sqrt{(\epsilon_{c,k} - \epsilon_{f,k} + \mu_f - \mu_c)^2 + 4b_0^2}\bigg) \\ &\times \theta\bigg(\mu_c + \mu_f - \epsilon_{c,k} - \epsilon_{f,k} \\ &\mp \sqrt{(\epsilon_{c,k} - \epsilon_{f,k} + \mu_f - \mu_c)^2 + 4b_0^2}\bigg) \\ &+ \frac{2}{5}V_{\mathrm{FS}}(\mu_c + \mu_f) + E(b_0). \end{aligned} \tag{4.33}$$

We can now consider the set of parameters for f that maximize $\delta_{F;c,f} = F_0 - F + E(b_0)$, which is the fermion contribution to the grand free energy relieved by boson condensation. The total grand free energy relieved, $F_0 - F$, then is also maximized for fixed b_0. We know that, physically, the f bandwidth is much smaller than the conduction electron bandwidth, so we fix μ_f at some value $\mu_f \ll \mu_c$. Eliminating $m_{f,x}$ through this and the constraint on V, we then vary the remaining parameters $r_{f;y}$ and $r_{f;z}$. We indeed find that $\delta_{F;c,f}$ is maximized when $r_{f;y,z} = r_{c;y,z}$ respectively (Fig. 4.5), implying the matching of the c and f Fermi surfaces in our toy mean-field calculation. We will study the renormalization of the f dispersion at strong coupling beyond the mean-field level (which can be obtained by exact numerical solution of the SD equations and by minimizing the total interacting grand free energy at the large N saddle point) in future work.

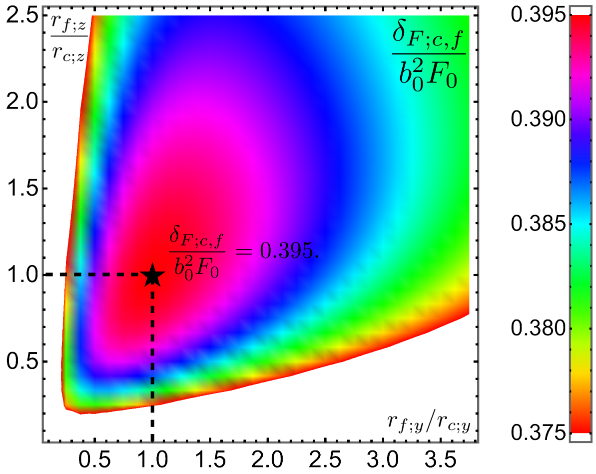

Figure 4.5: The relative grand free energy relieved, $\delta_{F;c,f}/(b_0^2 F_0)$, vs the eccentricity ratios controlling the shape of the ellipsoidal f Fermi surface relative to that of the c Fermi surface, for $\mu_f = \mu_c/10$. We use $V = 20\sqrt{2}/(3\pi^2)$, $m_{c,x} = 1.0$, $r_{c;y} = 0.8$, $r_{c;z} = 1.2$. It is maximized when the f and c Fermi surfaces are of the same shape, *i.e.* $r_{f;y} = r_{c;y}$ and $r_{f;z} = r_{c;z}$, which is denoted with a star on the plot.

4.4.2 Self-Energies and Phase Diagram

The SD equations for Model II with the matched FS that we have motivated are given by:

$$\begin{aligned} G_c(i\omega, k) &= \frac{1}{i\omega - \epsilon_{c,k} + \mu_c - \Sigma_c(i\omega, k)}, \\ G_f(i\omega, k) &= \frac{1}{i\omega - \epsilon_{f,k} + \mu_f - \Sigma_f(i\omega, k)}, \\ G_b(i\omega, k) &= \frac{1}{-i\omega + \epsilon_{b,k} + \Delta_b - \Sigma_b(i\omega, k)}. \end{aligned} \tag{4.34}$$

These equations are complemented by the expressions for the self-energies (diagrams in Fig. 4.1)

$$\begin{aligned} \Sigma_c(i\omega, k) = g^2 T \sum_{i\nu} \int \frac{d^3q}{(2\pi)^3} G_f((i\omega + i\nu), k + q) \\ \times G_b(-i\nu, q), \end{aligned}$$

$$\begin{aligned}\Sigma_f(i\omega,k) &= g^2 T \sum_{i\nu} \int \frac{d^3q}{(2\pi)^3} G_c(-(i\omega+i\nu),k+q) \\ &\quad \times G_b(-i\nu,q), \\ \Sigma_b(i\omega,k) &= -2g^2 T \sum_{i\nu} \int \frac{d^3q}{(2\pi)^3} G_c(i\omega+i\nu,k+q) \\ &\quad \times G_f(i\nu,q).\end{aligned} \tag{4.35}$$

Here again, the factor of 2 in the equation for Σ_b arises from the $su(2)$ spin degeneracy of c and f. Although the self-energies here can have momentum dependence due to the translational invariance of Model II, let us assume to begin with that the fermionic ones are independent of momentum for k near the FS, that is $\Sigma_{c,f}(i\omega,k) = \Sigma_{c,f}(i\omega)$. We will see below that this is a self-consistent assumption.

With the assumption of momentum independent fermionic self-energies, we can average the contributions to the bosonic self-energy coming from small patches of the FS [101]. The contribution from a given patch is

$$\begin{aligned}&\Sigma_b^p(i\omega,k) = \\ &-2g^2 T \sum_{i\nu} \int \frac{dq_\perp}{2\pi} \frac{d^2q_\parallel}{(2\pi)^2} \Bigg(i\nu - v_{f,F} q_\perp - q_\parallel^2/(2m_f) \\ &- \Sigma_f(i\omega) \Bigg)^{-1} \times \Bigg(i\nu + i\omega - v_{c,F}(q_\perp + k_\perp) \\ &- (q_\parallel + k_\parallel)^2/(2m_c) - \Sigma_c(i\omega+i\nu) \Bigg)^{-1},\end{aligned} \tag{4.36}$$

where $\perp, \parallel$ define the directions relative to the patch of the matched FS, $v_{c,f,F}$ are the Fermi velocities, and $m_{c,f}$ are the fermion masses. After integrating over q and averaging over patches (see Appendix 4.12), we obtain

$$\Sigma_b(i\omega,k) \approx -2g^2 m_c m_f \frac{|\omega|}{k} \equiv -\gamma_2 \frac{|\omega|}{k}. \tag{4.37}$$

Here $\gamma_2 = 2g^2 m_c m_f$ is the natural dimensionless coupling for the boson damping, akin to γ in Model I. The FS matching allows a small momentum boson ($k \to 0$) to decay into c-f particle-hole pairs, resulting in a low k singularity of the boson self-energy. This self-energy is identical to the "Landau damping" form [101] of low momentum bosons coupled to low energy particle-hole excitations about the FS of an ordinary metal. The Landau damping we obtain implies a dynamical exponent $z = 3$ for the critical bosonic fluctuations which has been shown to lead to MFL phenomenology in $d = 3$ [116, 117], as we will also explain in the following paragraphs.

Having calculated the boson self-energy, we may now determine the boson gap $\Delta_b(T)$ using the occupancy constraint as done above for Model I. Similarly to Model I, we get a QCP separating the FL* phase for $\kappa < \kappa_c$, where the boson is soft gapped at zero temperature and the heavy FL phase for $\kappa > \kappa_c$, where the boson is condensed $\langle b_1 \rangle \sim r_0\sqrt{N}$. At the critical point we find $\Delta_b(T) \sim T^{5/4}$

at low temperatures (and $B = 0$). The phase diagram of Model II is therefore qualitatively similar to Fig. 4.2: the critical fan is flanked by a FL* phase with a T^2 resistivity on the left, and a heavy FL phase with a large carrier density on the right.

With the boson Green's function determined we can compute the c self-energy (the calculation for f is almost identical):

$$\begin{aligned}
&\Sigma_c(i\omega, k) = \\
&g^2 T \sum_{i\nu} \int \frac{dq_\perp}{2\pi} \frac{d^2 q_\parallel}{(2\pi)^2} \frac{1}{i\nu + \gamma_2 \frac{|\nu|}{q} + \frac{q^2}{2m_b} + \Delta_b} \\
&\times \Bigg(i\nu + i\omega - v_{f,F}(q_\perp + k_\perp) \\
&- (q_\parallel + k_\parallel)^2/(2m_f) - \Sigma_f(i\omega + i\nu) \Bigg)^{-1}.
\end{aligned} \tag{4.38}$$

Since the fermion propagator (which depends on $q_\perp \sim q_\parallel^2$) is much more sensitive to $q_\perp$ at small frequencies and momenta than the boson propagator (which depends on $q_\perp^2 + q_\parallel^2 \sim q_\parallel^4 + q_\parallel^2$), we can set $q_\perp = 0$ in the boson propagator. As a result of this the self-energy takes a form similar to Model I, coupling momentum-averaged Green's functions ($q_\perp$ averaged for fermions and $q_\parallel$ for the bosons). Moreover, the self-energy we obtain resembles the behavior in Model I in that the momentum-averaged fermions couple to an effectively 2D boson;

$$\begin{aligned}
\Sigma_c(i\omega, k) &\approx g^2 T \sum_{i\nu} \left(\int \frac{dq_\perp}{2\pi} G_f(i(\nu + \omega, q + k) \right) \\
&\quad \times \left(\int \frac{d^2 q_\parallel}{(2\pi)^2} G_b(-i\nu, q_\parallel) \right) \\
&= -\frac{ig^2}{2v_{f,F}} T \sum_{i\nu} \int \frac{d^2 q_\parallel}{(2\pi)^2} \frac{\mathrm{sgn}(\nu + \omega)}{i\nu + \gamma_2 \frac{|\nu|}{q_\parallel} + \frac{q_\parallel^2}{2m_b} + \Delta_b}.
\end{aligned} \tag{4.39}$$

This self-energy is indeed independent of momentum k, as promised earlier. We continue by noting that we can ignore the $i\nu$ term compared to the boson self-energy $\gamma_2|\nu|/q_\parallel$, which is much larger at low frequencies. Hence we obtain the self-energy in the low frequency limit and $T = 0$:

$$\begin{aligned}
\Sigma_{c,f}(i\omega, T = 0) &= -\frac{\gamma_2 m_b}{12\pi^2 m_{c,f} k_F} \\
&\quad \times i\omega \ln\left(\frac{e\sqrt{2m_b \Lambda^3}}{\gamma_2 |\omega|} \right) \quad \text{(QCP)}, \\
\Sigma_{c,f}(i\omega, T = 0) &= -\frac{\gamma_2 m_b \ln(\Lambda/\Delta_b(T = 0))}{8\pi^2 m_{c,f} k_F} i\omega \\
&\quad + i \frac{\gamma_2^2 \sqrt{m_b/2}}{32\pi m_{c,f} k_F \Delta_b^{3/2}(T = 0)} \omega^2 \quad (\text{FL}^\star),
\end{aligned} \tag{4.40}$$

where Λ is the boson bandwidth and k_F is the Fermi momentum of the matched FS's. Due to the strong Landau damping we obtain a non-skewed MFL for all values of the damping parameter γ_2. This should be contrasted with Model I, which leads to a skewed MFL for small damping parameter γ. However the renormalization of the effective fermion masses upon approaching the QCP from the FL* phase are the same as in Model I.

At low but non-zero temperatures above the critical point, the Matsubara frequency sum in (4.40) may be computed analytically upon ignoring the $i\nu$ term as before. Then, we can compute the $q_{\|}$ integral numerically with a UV cutoff $\sim \sqrt{2m_b\Lambda}$ to obtain

$$\Sigma_{c,f}(i\omega, T) = -\frac{i\gamma_2 m_b}{m_{c,f}k_F} T\mathrm{sgn}(\omega)\varphi\left(\frac{|\omega|}{T}, \frac{\Lambda}{T}, \frac{\Lambda}{\Delta_b(T)}\right). \tag{4.41}$$

The dependencies on Λ/T and $\Lambda/\Delta_b(T)$ are logarithmic, as in Model I. As we have seen in the calculations for Model I, this form of the self-energy leads to a universal Planckian scattering rate $\tau^{-1} = (m_c/m_c^\star(T))\mathrm{Im}[\Sigma_{c,R}(\omega = 0, T)]$, up to slowly-varying logarithmic factors. Note that we obtain this Planckian scattering rate independent of the damping parameter γ_2 unlike in Model I, which resulted in Planckian scattering only in the strong damping regime $\gamma \gg 1$.

4.4.3 Transport

An exact calculation of the transport properties in Model II is more complicated than in Model I, because the vertex correction diagrams in Fig. 4.3 do not vanish. Due to momentum conservation, the momentum integrals in the left and right loops of these diagrams do not decouple as they do in Model I. Similarly, the cross-species current correlations do not vanish in Model II as they do in Model I and complicate the Ioffe-Larkin rule. Nonetheless, we will argue below that the effects of all of these corrections may be neglected, leading to transport properties that are dominated, as in Model I, by the self-energies obtained from the bubble diagram in the previous section (4.41) [4]. We show that this results in strange metal phenomenology (nearly T-linear resistivity) in the critical fan for sufficiently low temperatures. In the subsequent paragraphs, we will explain explicitly how this comes about.

First, we note that the conductivity in the quantum critical and FL* regimes is dominated by the conduction electrons c. The much heavier damped bosons, added in parallel, form an insulator in the FL* phase, and a poor conductor at the QCP, and therefore contribute negligibly to the conductivity. In the heavy FL phase, condensation of b leads to effective hybridization of the c and f bands, and the electrical transport is determined by the large hybridized Fermi surface.

Let us now turn to the question of vertex corrections. In conventional quantum critical systems, a single scattering of an electron off a low momentum critical boson ($\mathbf{q} \to 0$), included in the electron self-energy, leads to vanishing current relaxation. The transport time is therefore not set by the quasiparticle relaxation time, and is instead obtained from the Kubo formula only by summing over multiple scatterings, which are included in the current vertex corrections. In Model II, the situation is different because the decay process included in the electron self-energy $c_{\mathbf{k}} \to f_{\mathbf{k}-\mathbf{q}} + b_{\mathbf{q}}$ leads to

---

[4] While the transport vertex corrections can still be resummed exactly as a ladder series owing to our controlled large N limit, unlike in previous work on fermions coupled to critical bosons [76], this calculation is tedious, and we therefore defer it for future work

significant current relaxation even at small momentum transfers $\mathbf{q} \to 0$. The final state current carried by the boson $\sim eq/m_b$, is much smaller than the initial state current $\sim ev_F$ carried by the conduction electron. Note that the f fermion does not contribute any additional current to the final state: due to the local occupancy constraint enforced by the Ioffe-Larkin rules, the boson and f fermion must carry the same current, which is also equal to the total current carried by them, as the f fermion is uncharged.

Although single scattering events lead to current relaxation over short timescales, whose rate is set by the electron self-energy, as argued above (see also [115]), we also need momentum relaxation in order to obtain a finite DC conductivity. The nonzero overlap of the total current and the conserved total momentum operators will prevent the current from fully relaxing over the long timescales relevant to DC transport, leading to an infinite DC conductivity [59]. However, this problem is resolved in practice by the existence of an adequate amount of impurities that can scatter the heavy f fermions and thus dissipate the momentum received from the c fermions faster than the equilibration rate between the three species. This eliminates the above "momentum drag" phenomenon, and allows the self-energy to also set the current relaxation rate of the conduction electrons c over long time scales.

Our identification of the current relaxation rate with the rate set by the c electron self-energy (4.41), just like in Model I, therefore allows for an identification of Planckian strange metal phenomenology in the critical regime of Model II at sufficiently low T. As in Model I, we can obtain the resistivity from Eq. (4.27), which results in $\rho_{xx} \sim T\ln(\Lambda/T)$.

Important differences from Model I, however, arise from the boson damping $\Sigma_b(i\omega, k) \sim |\omega|/k$, which is parametrically much larger at small k than $\Sigma_b(i\omega, k) \sim \gamma|\omega|$ in Model I regardless of the value of γ. Because the momentum of occupied bosons is effectively cut off at $k \sim \sqrt{m_b T}$. We can identify an effective damping constant $\gamma(T) = \gamma_2/\sqrt{m_b T}$, which is always large at sufficiently low temperatures (see Appendix 4.12). Hence there is never any significant enhancement of R_H in the critical regime at low T in Model II, as there is no weak b damping regime like the small γ regime for Model I, that was required there to obtain an enhanced R_H. Furthermore, the strong damping ensures that Model II is always in the Planckian regime at low enough T, as opposed to Model I, which was Planckian only when $\gamma \gg 1$.

In Appendix 4.12, we consider a higher temperature regime, occuring for $T \gg \gamma_2^2/m_b$, in which the boson damping is weaker and an enhancement of R_H is consequently obtained. However, the resistivity in this regime is no longer T-linear and instead scales as $\sim \sqrt{T}$.

4.5 Discussion

The new large N approach formulated in this paper captures a strongly coupled QCP, showing linear in T resistivity at a Kondo breakdown transition involving a change of the Fermi surface volume. Such MFL phenomenology, seen ubiquitously in experiments with heavy fermion materials, could not be obtained in a controlled way within previous large N theories [125, 36, 14, 139]. The essential new element in our formulation is that the number of fermions and critical boson species are both scaled with N.

The MFL with linear in T resistivity is obtained within two distinct models of the Kondo lattice. It is worth emphasizing the differences in the physical situations they describe, and in the predicted phenomena. Model I is disordered, and leads to a MFL only if the QCP and adjacent FL* phase are deconfined in layers, that is deconfined inside 2D planes, yet confined between planes. This model can be tuned between two regimes by a coupling constant γ. In the strong damping limit $\gamma \gg 1$ the system exhibits Planckian dissipation, with a universal electron relaxation time $\tau_{tr} \approx \hbar/(k_B T)$. The strong damping also prevents any significant enhancement of the Hall coefficient R_H in the critical regime. In the weak damping regime, $\gamma \ll 1$, the transport relaxation time is much larger than the Planckian time (by a factor $1/\gamma$), and the Hall coefficient R_H is enhanced in the critical regime. Furthermore, the electron self-energy in this regime is "skewed", with an asymmetry in the damping of particle vs. hole excitations (4.22). We note that strange metallic behavior with a transport relaxation time much larger than the Planckian time has been observed experimentally in HFMs [152].

Model II, on the other hand, is translationally invariant, and describes a transition from a fully 3D FL* with a small Fermi surface to a heavy Fermi liquid with a large Fermi surface. The critical boson is always strongly damped at low temperatures due to Landau damping, leading to Planckian dissipation with a universal electron transport lifetime $\tau_{\text{tr}} \sim \hbar/(k_B T)$. The strong damping prevents enhancement of R_H in the critical regime.

A testable prediction, which follows from the analysis of the two models, is that Planckian dissipation at the QCP cannot be accompanied by enhancement of the Hall coefficient R_H. Enhancement of R_H at the QCP, as has been observed in recent experiments with CeCoIn$_5$ [98], can occur only in the weakly damped regime of Model I, where a set of additional features are predicted: first, the QCP and the nearby FL* phase are deconfined only within 2D planes, which would have observable implications on transport. For example, the thermal conductivity is expected to be strongly anisotropic, because in this phase spinons contribute to the in-plane, but not to the out-of-plane thermal transport. The charge conductivity, on the other hand, is dominated by the conduction electrons, which can hop between planes, and would therefore be much more isotropic. Consequently, only the in-plane Lorenz ratio is expected to be significantly enhanced. Another unique property of the weakly damped ($\gamma \ll 1$) MFL, is a skewed fermion spectral function, which is expected to generate a low temperature Seebeck coefficient in the critical regime [53, 114]. Sizeable $T \to 0$ Seebeck coefficients have recently been reported experimentally in 2D strange metals [55, 37], and it would be interesting to investigate whether these arise due to skewed electron self-energies.

The new large N approach we have introduced to study the Kondo breakdown transition in HFM can also be useful in formulating a controlled theory of other quantum critical states. The high T_c cuprate superconductors, for example, exhibit similar signatures of FS reconstruction near optimal doping [122], accompanied by T-linear resistivity [149]. While there are no local moments to be subsumed in the Fermi sea, a parton model describing a change in FS volume has recently been proposed [177]. Investigating this QCP using the new large N scheme is an interesting problem for future work. Our approach can also be used to address the interplay of these critical fluctuations with superconductivity and magnetism, which appear to be crucial to cuprate phenomenology.

Another interesting extension of this work would be to formulate a controlled treatment of gapless gauge field fluctuations coupled to matter fields. This is important, for example, for describing gapless $U(1)$ spin liquids or the Halperin-Lee-Read state in a half-filled Landau level [58, 76]. The standard large N theory captures the gauge field fluctuations within a $1/N$ expansion, which is known to be uncontrolled [88]. In the large N models we introduced here, gauge field fluctuations are still suppressed by $1/N$, but the $1/N$ expansion could possibly be better controlled. Furthermore, it is interesting to explore generalizations of the scheme to include N flavors of $U(1)$ gauge fields with flavor-random gauge couplings, and thereby capture the feedback of the gauge field fluctuations self-consistently at the saddle point level itself.

Supplemental Material

4.6 Kubo formula in Landau Level Basis for Model I

In this Appendix, we obtain expressions for the conductivities of the different species in Model I via the Kubo formula, which are given by their respective bubble diagrams of Fig. 4.3, as described in the main text. We compute these generally at nonzero values of the out-of-plane magnetic field B by working in the Landau Level basis in the $x-y$ plane with wavefunctions

$$\begin{aligned}\psi_{n,k}(x,y) &= \frac{1}{\sqrt{L_x\ell}}e^{ikx}\phi_{n,k}(y/\ell);\\ \phi_{n,k}(z) &= \frac{\pi^{-1/4}}{\sqrt{2^n n!}}H_n(z+k\ell)\exp\left(-\frac{(z+k\ell)^2}{2}\right),\end{aligned} \tag{4.42}$$

where $\ell = 1/\sqrt{eB}$ and $H_n(x)$ are the (physicist's) Hermite polynomials satisfying the recursion relation $H_{n+1}(x) = 2xH_n(x) - H_n'(x)$. The energy of the states is $\omega_{c\lambda}(n+1/2)$ where $\omega_{c\lambda} = |e|B/m_\lambda$, where $\lambda \in \{c, f, b\}$. The use of the Landau level basis is possible because the self-energies of all three species are independent of momentum and therefore proportional to the identity matrix in real space, which implies that they are also proportional to the identity matrix in the Landau level basis, greatly simplifying the computation. Results such as (4.27) and (4.29) in the weak magnetic field limit can be obtained by taking the $B \to 0$ limit of our expressions here.

It is important to recall the following identities:

$$\begin{aligned}\int dz\phi_{n,k}(z)\partial_z\phi_{m,k}(z) &= \sqrt{\frac{m}{2}}\delta_{n,m-1} - \sqrt{\frac{m+1}{2}}\delta_{n,m+1},\\ \int dz\phi_{n,k}(z)\partial_z(z+k\ell)\phi_{m,k}(z) &= \sqrt{\frac{m}{2}}\delta_{n,m-1} + \sqrt{\frac{m+1}{2}}\delta_{n,m+1}.\end{aligned} \tag{4.43}$$

Now, our starting point is the Kubo formula in momentum space, which we will transform to the Landau Level basis. Recall that [97] $\sigma_{\lambda,\alpha\beta}(\omega,q) = -\mathrm{Im}\Pi^R_{\lambda,\alpha\beta}(\omega,q)/\omega$ where

$$\Pi_{\lambda,\alpha\beta} = -\frac{1}{V}\int dxdx'dydy'e^{iq_x(x-x')}e^{iq_y(y-y')}\int_0^{1/T}d\tau e^{i\omega\tau}\langle T_\tau J^\dagger_{\lambda,\alpha}(r,\tau)J_{\lambda,\beta}(r',0)\rangle, \tag{4.44}$$

where τ is imaginary time. With the above identities, a straightforward calculation will yield the spatially-integrated current as

$$\begin{aligned}\frac{2m_\lambda i}{e}\int dxdyJ_\lambda(r,\tau) &\equiv \int dxdy\left(\lambda_r^\dagger(\tau)(\nabla - ieA)\lambda_r(\tau) - (\nabla + ieA)\lambda_r^\dagger(\tau)\lambda_r(\tau)\right)\\ &= \frac{2}{\ell}\sum_{k,n}\left(\begin{pmatrix} i\\ 1\end{pmatrix}\sqrt{\frac{n+1}{2}}\lambda^\dagger_{nk}(\tau)\lambda_{n+1,k}(\tau) + \begin{pmatrix} i\\ -1\end{pmatrix}\sqrt{\frac{n}{2}}\lambda^\dagger_{nk}(\tau)\lambda_{n-1,k}(\tau)\right).\end{aligned} \tag{4.45}$$

We now evaluate $\Pi_{\lambda,xx}$ and $\Pi_{\lambda,xy}$ at $q = 0$ using this expression. Using $G_{\lambda nk}(\tau) = \langle \lambda_{nk}(\tau)\lambda^{\dagger}_{nk}(0)\rangle$, we get

$$\begin{pmatrix}\Pi_{\lambda,xx}\\ \Pi_{\lambda,xy}\end{pmatrix} = -\eta\frac{e^2}{V\ell^2 m_\lambda^2}\int_0^{1/T} d\tau e^{i\omega\tau}\sum_{nk}\begin{pmatrix}\frac{n+1}{2}G_{\lambda nk}(\tau)G_{\lambda,n+1,k}(-\tau) + \frac{n}{2}G_{\lambda nk}(\tau)G_{\lambda,n-1,k}(-\tau)\\ -i\frac{n+1}{2}G_{\lambda nk}(\tau)G_{\lambda,n+1,k}(-\tau) + i\frac{n}{2}G_{\lambda nk}(\tau)G_{\lambda,n-1,k}(-\tau)\end{pmatrix} \tag{4.46}$$

$$= -\eta\frac{e^2\omega_{c\lambda}^2}{2\pi}T\times \tag{4.47}$$

$$\sum_{i\nu_n}\left(\sum_n \frac{n+1}{2}\begin{pmatrix}1\\ -i\end{pmatrix} G_{\lambda n}(i\nu_n)G_{\lambda,n+1}(i\nu_n - i\omega) + \frac{n}{2}\begin{pmatrix}1\\ i\end{pmatrix} G_{\lambda n}(i\nu_n)G_{\lambda,n-1}(i\nu_n - i\omega)\right).$$

where $\eta = \pm$ for bosons and fermions, respectively, because of time-ordering. In the second step, we switched to Matsubara frequencies, used the fact that $G_{nk}(\tau) \equiv G_n(\tau)$ is independent of k, and there are $L_x L_y/\ell^2/(2\pi)$ terms in the k sum.

We have neglected the vertex corrections to the conductivity in Fig. 4.3 here, which can be shown to vanish even at $B \neq 0$. Since the disordered interactions g^r_{ijk} are uncorrelated between different sites in Model I, such corrections can be written as

$$\begin{aligned}\delta\Pi_\lambda = &\int dxdydx'dy'dx_{1,2}dy_{1,2}\times\\ &\left\langle J_\lambda(r,\tau)\int d\tau_{1,2,3,4}\lambda^\dagger_{r_1}(\tau_1)\lambda_{r_1}(\tau_2)K(\tau_1,\tau_2,\tau_3,\tau_4)\lambda^\dagger_{r_2}(\tau_3)\lambda_{r_2}(\tau_4)J_\lambda(r',\tau')\right\rangle.\end{aligned} \tag{4.48}$$

Since $\lambda_r(\tau) = \sum_{n,k}\psi_{n,k}(r)\lambda_{nk}(\tau)$, and $G_{\lambda nk}(\tau)$ are independent of k, the identity

$$\int dk H_n(z+kl)H_{n\pm 1}(z+kl)\exp\left(-(z+kl)^2\right) = 0, \tag{4.49}$$

ensures that these corrections vanish.

Proceeding similarly as to [97], we next switch to the Lehmann representation, analytically continue, take the imaginary part, and expand for small ω. We find

$$\begin{aligned}\sigma_{\lambda,xx} &= -s_\lambda\lim_{\omega\to 0}\frac{\mathrm{Im}[\Pi_{\lambda,xx}(\omega)]}{\omega} = -\frac{s_\lambda e^2\omega_{c\lambda}^2}{4\pi}\sum_n (n+1)\int\frac{d\epsilon}{(2\pi)}A_{\lambda n}(\epsilon)A_{\lambda,n+1}(\epsilon)\left(\frac{\partial n_\eta(\epsilon)}{\partial\epsilon}\right)\\ &= -\frac{s_\lambda e^2}{4\pi}\int\frac{d\epsilon}{2\pi}\frac{4\Sigma''_\lambda(\epsilon)\frac{\partial n_\eta(\epsilon)}{\partial\epsilon}}{4[\Sigma''_\lambda(\epsilon)]^2 + \omega_{c\lambda}^2}\left(2\Sigma''_\lambda(\epsilon) + 2(\epsilon+\tilde{\mu}_\lambda)\mathrm{Im}\left[\psi_0\left(\frac{1}{2} + \frac{-\epsilon + i\Sigma''_\lambda(\epsilon) - \tilde{\mu}_\lambda}{\omega_{c\lambda}}\right)\right]\right),\end{aligned} \tag{4.50}$$

where s_λ is the spin degeneracy of the species λ. We performed the Landau level sum in terms of the digamma function, ψ_0, and we used $\psi_0(z) = \psi_0(1+z) - 1/z$ and

$$A_{\lambda n}(\epsilon) = \frac{2\eta\Sigma''_\lambda(\epsilon)}{(\epsilon + \tilde{\mu}_\lambda - (n+1/2)\omega_{c\lambda})^2 + [\Sigma''_\lambda(\epsilon)]^2}, \tag{4.51}$$

so that $\Sigma''_\lambda(\epsilon) = \mathrm{Im}[\Sigma_{\lambda,R}(\epsilon)]$ and $\tilde{\mu}_\lambda = \mu_\lambda - \mathrm{Re}[\Sigma_{\lambda,R}(\epsilon)]$.

For $\sigma_{\lambda,xy}$, we convert to relative and center of mass coordinates $\epsilon_c = (\epsilon + \epsilon')/2$ and $\epsilon_r = \epsilon - \epsilon'$. We then symmetrize with respect to ϵ_r in order to get an integral from 0 to ∞. We find

$$\begin{aligned}
\Pi_{\lambda,xy}(\omega \to 0) &= -i\frac{e^2\omega_{c\lambda}^2}{4\pi}\sum_n (n+1)\int \frac{d\epsilon d\epsilon'}{(2\pi)^2} A_{\lambda n}(\epsilon)A_{\lambda,n+1}(\epsilon')(n_\eta(\epsilon) - n_\eta(\epsilon'))\left[\frac{2(\omega + i\delta)}{(\epsilon - \epsilon')^2}\right], \\
\sigma_{\lambda,xy} &= -\frac{s_\lambda e^2 \omega_{c\lambda}^2}{2\pi}\sum_n (n+1)\int_0^\infty \frac{d\epsilon_r}{2\pi}\int_{-\infty}^{\infty}\frac{d\epsilon_c}{2\pi}\frac{\sinh\left(\frac{\epsilon_r}{2T}\right)}{\cosh\left(\frac{\epsilon_c}{T}\right) - \eta\cosh\left(\frac{\epsilon_r}{2T}\right)}\frac{1}{\epsilon_r^2} \\
&\times \left[A_{\lambda n}\left(\epsilon_c + \frac{\epsilon_r}{2}\right)A_{\lambda,n+1}\left(\epsilon_c - \frac{\epsilon_r}{2}\right) - A_{\lambda n}\left(\epsilon_c - \frac{\epsilon_r}{2}\right)A_{\lambda,n+1}\left(\epsilon_c + \frac{\epsilon_r}{2}\right)\right] \\
&= -\frac{s_\lambda e^2}{(2\pi)^3}\int_0^\infty d\epsilon_r \int_{-\infty}^{\infty} d\epsilon_c \left(F_\lambda(\epsilon_c, \epsilon_r) - F_\lambda(\epsilon_c, -\epsilon_r)\right)\frac{\sinh\left(\frac{\epsilon_r}{2T}\right)}{\cosh\left(\frac{\epsilon_c}{T}\right) - \eta\cosh\left(\frac{\epsilon_r}{2T}\right)}\frac{1}{\epsilon_r^2},
\end{aligned} \tag{4.52}$$

The sum can be done to give an explicit expression for $F_\lambda(\epsilon_c, \epsilon_r)$ as

$$\frac{F_\lambda\left(\frac{\epsilon+\epsilon'}{2}, \epsilon - \epsilon'\right)}{2\Sigma''_\lambda(\epsilon)\Sigma''_\lambda(\epsilon')} = \mathrm{Im}\left[\frac{\psi_0\left(\frac{2\epsilon - 2i\Sigma''_\lambda(\epsilon) - 2\tilde{\mu}_\lambda(\epsilon)}{2\omega_{c\lambda}} - \frac{1}{2}\right)(2\epsilon - \omega_{c\lambda} - 2i\Sigma''_\lambda(\epsilon) - 2\tilde{\mu}_\lambda(\epsilon))}{\Sigma''_\lambda(\epsilon)(\Sigma''_\lambda(\epsilon')^2 + (\epsilon' - \epsilon + \omega_{c\lambda} + i\Sigma''_\lambda(\epsilon) - \tilde{\mu}_\lambda(\epsilon') + \tilde{\mu}_\lambda(\epsilon))^2)}\right] \tag{4.53}$$

$$+ \mathrm{Im}\left[\frac{\psi_0\left(\frac{2\epsilon' + 2i\Sigma''_\lambda(\epsilon') - 2\tilde{\mu}_\lambda(\epsilon')}{2\omega_{c\lambda}} + \frac{1}{2}\right)(2\epsilon' + \omega_{c\lambda} + 2i\Sigma''_\lambda(\epsilon') - 2\tilde{\mu}_\lambda(\epsilon'))}{\Sigma''_\lambda(\epsilon')}\right. \tag{4.54}$$

$$\left.\times \frac{1}{(\Sigma''_\lambda(\epsilon')^2 - \Sigma''_\lambda(\epsilon)^2 + 2i\Sigma''_\lambda(\epsilon')(\epsilon - \epsilon' - \omega_{c\lambda} + \tilde{\mu}_\lambda(\epsilon') - \tilde{\mu}_\lambda(\epsilon)) - (\epsilon - \epsilon' - \omega_{c\lambda} + \mu_\lambda(\epsilon') - \mu_\lambda(\epsilon))^2)}\right].$$

For the fermions, for small magnetic fields, these expressions give the same result as the expressions derived from the Boltzmann equations in [114] with the identification $v_F^2\nu/(4\pi) \to n/m$ where v_F is the Fermi velocity, n is the density, and m is the mass. However, for large magnetic fields, our expressions will have quantum oscillations that are absent in the Boltzmann treatment.

4.7 Boson Spectral Function and Δ_b in Model I

In this appendix, we derive the boson spectral function and the soft gap Δ_b generally for a nonzero out-of-plane magnetic field. As in the derivation of the Kubo formula, we use the Landau level basis, which is made possible by the spatial locality and site-invariance of the occupancy constraint in the last line of (4.6). The values of Δ_b at small magnetic fields can be obtained by taking the $B \to 0$ limit in our expressions.

Because $\mu_c, \mu_f \gg \omega_{c,c/f}$, we still have the original result for the fermion Green's function that $G_{c,f}(i\omega) = -i(\nu_{c,f}/2)\mathrm{sgn}(\omega)$. That is, the fermions are less affected by the Landau level quantization than the bosons, and, consequently, the boson self-energy calculation in the main text is unaffected.

However, the boson spectral function must be calculated by summing over the spectral functions in each Landau level instead of integrating over momentum. The result is

$$\begin{aligned}
A_b(\omega) &= \frac{1}{\ell^2 2\pi}\sum_m \frac{2\gamma\omega}{(\omega-(m+1/2)\omega_{cb}-\Delta_b)^2+\gamma^2\omega^2} \\
&= -\frac{m_b}{\pi}\mathrm{Im}\left[\psi_0\left(\frac{1}{2}-\frac{-\Delta_b+\omega+i\gamma\omega}{\omega_{bc}}\right)\right] \qquad (4.55) \\
&\xrightarrow{B\to 0} \frac{m_b}{\pi}\left[\pi\Theta(\omega-\Delta_b)+\tan^{-1}\left(\frac{\gamma\omega}{\Delta_b-\omega}\right)\right],
\end{aligned}$$

where $\Theta(x)$ is the Heaviside step function, $\psi_0(z)$ is the digamma function, $\ell = 1/\sqrt{e_b B}$, and $\omega_{cb} = e_b B/m_b$ with e_b, m_b the charge and mass of the boson respectively.

Now, recall from the main text that the scaling of the fermion self-energy expressions above depends crucially on $\Delta_b(T)$. It can be easily checked that the change in the number of f fermions in response to a shifting chemical potential is suppressed by $\Delta\mu_f/\Lambda_f$ where Λ_f, the f fermion bandwidth, is assumed to be large. Therefore, the constraint can be written as

$$\kappa-\kappa_c = (G_b(\tau=0^-,\Delta_b(T)) - G_b(\tau=0^-,\Delta_{b,c}(0))), \qquad (4.56)$$

and Δ_b depends on both temperature and κ, but we suppress the κ dependence generally. When $\kappa=\kappa_c$, $\Delta_b=\Delta_{b,c}$ and $\Delta_{b,c}(T=0)=0$. This is reminiscent of the $O(N)$ rotor model [131] and the calculation of the thermal mass in [112].

Although we can do this calculation carefully in multiple ways, we will recall that $G_b(\tau = 0^-) = \sum_i \langle b_i^\dagger(\tau=0^-)b_i(\tau=0^-)\rangle \equiv n_b$, which is the number density of bosons. For this number to converge, we choose to regulate it in the usual way (see [97])

$$n_b = \frac{1}{V}\sum_{nk}\int_{-\infty}^{\infty}\frac{d\omega}{2\pi}n_B(\omega)A_{bn}(\omega,\Delta_b), \qquad (4.57)$$

where A_{bn} is the summand seen in (4.55).

Fig. 4.6 summarizes the behavior of $\Delta_b(T)$ in the three phases at zero and finite applied field. The important feature is the T-linear (up to logarithmic corrections) growth in the critical region. Low T transport is dictated by the limit of $z=\Delta_b/T$ which shifts from ∞ to zero across the transition.

Note that

$$\int_{-\infty}^{\infty} d\omega n_B(\omega)A_{bn}(\omega,\Delta_b) = \int_0^{\infty} d\omega n_B(\omega)(A_{bn}(\omega,\Delta_b)-A_{bn}(-\omega,\Delta_b)) - \int_0^{\infty} d\omega A_{bn}(-\omega,\Delta_b), \qquad (4.58)$$

and that the first integral on the right-hand side is 0 when $T=0$. Recalling the form of the boson's spectral function from (4.55), we will find

$$\begin{aligned}
&2\pi(\kappa-\kappa_c) \\
&= \frac{\omega_{cb}m_b}{2\pi}\left[\int_0^{\infty} n_B(\omega)\frac{(A_b(\omega,\Delta_b)-A_b(-\omega,\Delta_b))}{1/(\ell^2 2\pi)} + \frac{2\gamma}{\gamma^2+1}\ln\left(\frac{\Gamma(\mathcal{N}+3/2)\Gamma(1/2+\Delta_b/\omega_{cb})}{\Gamma(\mathcal{N}+3/2+\Delta_b/\omega_{cb})\Gamma(1/2)}\right)\right],
\end{aligned} \qquad (4.59)$$

where we have cut off the Landau level sum at $\mathcal{N}=\Lambda/\omega_{bc}$ and $\Gamma(n)$ is the Gamma function.

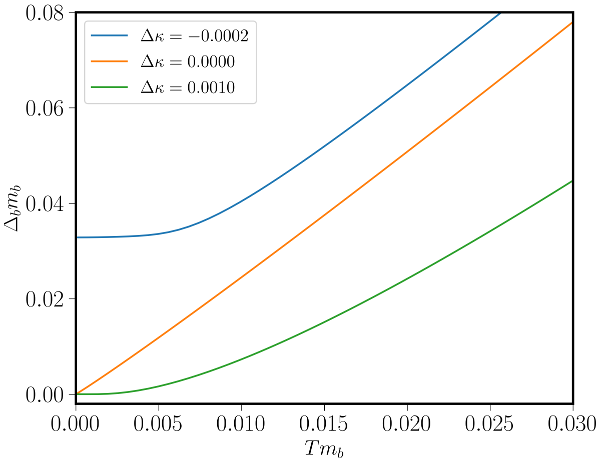

Figure 4.6: We plot Δ_b vs. T for various $\Delta\kappa = \kappa - \kappa_c$ with the color indicating $\Delta\kappa$. All curves become T-linear upon entering the critical region, but are either exponentially suppressed or approach a constant as $T \to 0$ if $\Delta_\kappa > 0$ or $\Delta_\kappa < 0$ respectively. All other parameters are the same as in Fig. 4.2 in the main text.

Taking the $B \to 0$ limit of (4.59), we can scale out $\Delta_b = zT$ and $x = \omega/T$ to find

$$\begin{aligned} &2\pi^2(\kappa-\kappa_c)\frac{1}{Tm_b} \\ &= \int_0^\infty \frac{dx}{e^x-1}\left[\tan^{-1}\left(\frac{\gamma x}{z-x}\right)+\tan^{-1}\left(\frac{\gamma x}{z+x}\right)\right] - \pi\ln\left(1-e^{-z}\right) - \frac{\gamma}{\gamma^2+1}z\ln\left(\frac{\Lambda e}{zT}\right). \end{aligned} \tag{4.60}$$

As $z \to 0$, the first two terms of the left-hand side dominate and as $z \to \infty$, the rightmost term dominates, so we see that there is a solution with z, whose value will change logarithmically, as $T \to \infty$. As expected, there is always a solution, so the bosons are not truly condensed as long as their dispersion is strictly 2D. Instead, for $\kappa > \kappa_c$ the gap becomes exponentially small in $(\kappa - \kappa_c)/T$, i.e. $\Delta_b \sim T\exp\left[-\frac{2\pi(\kappa-\kappa_c)}{Tm_b}\right]$. In reality, however, there is a stable condensate solution at low temperature, facilitated by the 3D boson dispersion self-consistently generated by the presence of the condensate. For this reason, we have treated this low-temperature regime of the large Fermi surface phase ($\kappa > \kappa_c$) separately (see Appendix 4.11).

4.8 Limiting Self-Energy Calculations in Model I

At low temperatures over the critical region, Δ_b/T is order one, so σ^b_{xx} and σ^b_{xy} are suppressed relative to the fermions, which are gapless. Therefore, by the Ioffe-Larkin composition rules (see Appendix 4.9), $\sigma^{bf}_{xx} \approx \sigma^b_{xx}$ and $R_H \approx R_{H,c}$ at low temperatures, which we confirm numerically. $R_{H,c}$, in turn, is determined by (4.29), and depends on the dimensionless parameters $(\kappa - \kappa_c)/(Tm_b)$, Λ/T, and γ. In Fig. 4.7 we plot the dependence of $R_{H,c}n_c$ at criticality ($\kappa = \kappa_c$) on the latter two parameters.

To understand this behavior, we now derive simple limiting forms for the low-temperature Δ_b and fermion self-energy at criticality at low B. We'll consider three limits $\gamma \to 0$ with T small but finite, $\gamma \to \infty$ with T small but finite, and $T \to 0$ with γ fixed. These expressions are used to obtain an estimate of the enhancement of the Hall coefficient given in the main text.

We first wish to solve (4.60) when $\kappa = \kappa_c$ and $\gamma \to 0$ at fixed T. The integral on the right-hand side (RHS) is smaller than the other two terms, in this limit. We make the guess that $e^{-z} \ll 1$, so we arrive at

$$\begin{aligned} z = \frac{\Delta_b}{T} &= \ln\left[\frac{\pi}{\gamma z \ln\left(\frac{\Lambda e}{zT}\right)}\right] = \ln\left(\frac{\pi}{\gamma}\right) - \ln\left[z \ln\left(\frac{\Lambda e}{zT}\right)\right] \\ &\approx \ln\left(\frac{\pi}{\gamma}\right) - \ln\left[\ln\left(\frac{\pi}{\gamma}\right) \ln\left(\frac{\Lambda e}{\ln(\pi/\gamma) T}\right)\right]; \qquad \gamma \to 0, \end{aligned} \tag{4.61}$$

which justifies our assumption. In the last step, we used the fact that the second term is smaller than the first as $\gamma \to 0$, so we obtained an approximate expression for z by simply substituting $z = \ln(\pi/\gamma)$ on the RHS. Better approximations are obtained by iteration, by substituting the improved expression for z.

By inserting (4.55) into (4.19), we can evaluate the self-energy at leading order in γ at criticality:

$$\begin{aligned} \Gamma_{\omega,T} &\equiv \mathrm{Im}[\Sigma_{c,R}(\omega, T)] \\ &= \lim_{\gamma \to 0} -\frac{\gamma m_b}{2\pi \nu_c} T \left[\ln\left(\frac{1 + e^{(\omega - \Delta_b)/T}}{1 - e^{-\Delta_b/T}}\right) \right. \\ &\quad \left. + \gamma \left(-\frac{\omega}{T} + \frac{\Delta_b}{T} \ln\left(\frac{\Delta_b}{|\Delta_b - \omega|}\right)\right)\right]. \end{aligned} \tag{4.62}$$

The $\mathcal{O}(1)$ term arises from approximating the spectral function as a step function. In the limit that T is fixed and $\gamma \to 0$, $\Delta_b/T \sim \ln(1/\gamma)$. Corrections to the spectral function, therefore, need only be integrated against $n_F(\epsilon' - \omega) - \Theta(-\epsilon')$, which we evaluate with the Sommerfeld approximation. The first term in (4.62) goes as $Te^{-\Delta_b/T} \sim \gamma \Delta_b$, but, in this limit, the second term goes as $\gamma \omega^2/\Delta_b$ and is therefore higher order. Computing $R_{H,c} n_c$ using (4.29), and using just the first term in (4.62), gives exactly $4/3$ when $\gamma \ll 1$.

Turning to the $\gamma \to \infty$ limit, we see that the integral in (4.60) is well approximated by taking the integrand as π from $z\pi/(2\gamma)$ to z, and as 0 everywhere else. The error from this approximation is roughly a constant close to $\pi/2$ as $\gamma \to \infty$, so we end up needing to solve

$$-\pi \ln\left(\frac{1 - e^{-z\pi/(2\gamma)}}{\sqrt{e}}\right) = \frac{z}{\gamma} \ln\left(\frac{\Lambda e}{zT}\right). \tag{4.63}$$

If T is small enough, z/γ will be small, which allows us to approximate the left-hand side as $-\pi \ln[(z\pi)/(2\sqrt{e}\gamma)]$. Finally, since z/γ is small, we neglect the term $(z/\gamma)\ln(z/\gamma)$ that appears on the right-hand side. These approximations altogether yield

$$z \approx \frac{\pi\gamma}{\ln\left(\frac{\Lambda}{T\gamma e}\right)} W_0\left(\frac{2\sqrt{e}}{\pi^2} \ln\left(\frac{\Lambda}{T\gamma e}\right)\right); \qquad \gamma \to \infty, \tag{4.64}$$

where $W_0(z)$ is the Lambert W function.

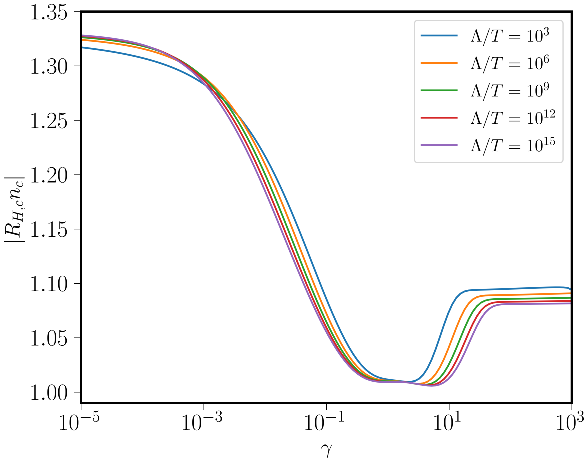

Figure 4.7: We plot $R_{H,c}n_c$, the Hall coefficient for the c electrons when $\kappa = \kappa_c$, which approximates the total R_H at low temperatures. In this regime, it depends on only two parameters: γ and Λ/T. We find in this supplement that the peak at low γ is exactly at 4/3.

The self-energy in the large γ limit is well approximated by the following:

$$\begin{aligned}\Gamma_{\omega,T} = -\frac{\gamma m_b}{2\pi\nu_c}T\Big[\frac{z}{\gamma}\ln\left(\frac{\Lambda e}{zT}\right) + \pi\ln\Big(1+e^{\omega/T}\Big)\\ -\tan^{-1}(\gamma)\ln\left(\frac{1+e^{\omega/T}}{1+e^{-\omega/T}}\right)\Big]; \qquad \gamma\to\infty,\ z/\gamma<1,\end{aligned} \tag{4.65}$$

where the integrals over the fermion occupation functions are done by setting $\Delta_b \to 0$ in the spectral function, which is accurate so long as $\Delta_b/(T\gamma) \ll 1$. When $z \to 0$ limit of that expression is plugged into (4.29), one finds $R_{H,c} \approx -1.07/n_c$ in good agreement with the numerics. Numerical studies confirm $R_{H,c}n_c$ increases near $\gamma = 0, \infty$ with a single minimum near $\gamma = 1$, the maximum being 4/3.

To understand the temperature dependence of the resistivity at criticality and small γ we use the formula [114].

$$\begin{aligned}\rho_{c,xx} &= \left(\frac{n_c}{8m_cT}\int_{-\infty}^{\infty} d\epsilon\frac{\text{sech}^2(\epsilon/2T)}{\Gamma_{\epsilon,T}}\right)^{-1}\\ &= T\left(\frac{n_c}{8m_c}\int_{-\infty}^{\infty} dx\frac{\text{sech}^2(x/2)}{(\Gamma_{xT,T})/T}\right)^{-1}.\end{aligned} \tag{4.66}$$

Plugging the value of Δ_b (4.61) into (4.62) or the exact result we get that $\Gamma_{xT,T}/T$ depends on T only through logarithmic corrections.

To calculate the self-energy in the low-temperature limit at fixed field–as we do in our numerical calculations–we must use the finite field expression (4.55). For temperatures sufficiently lower than B the self-energy takes the form $\Gamma_c \approx (T^2/B)g(\omega/T)$ and will be dominated by the cyclotron frequency. This will invalidate the small field approximation. In this case we must include the quadratic terms in B for the Hall coefficient [114]. The Hall coefficient then goes to one as $\Gamma/B \to 0$.

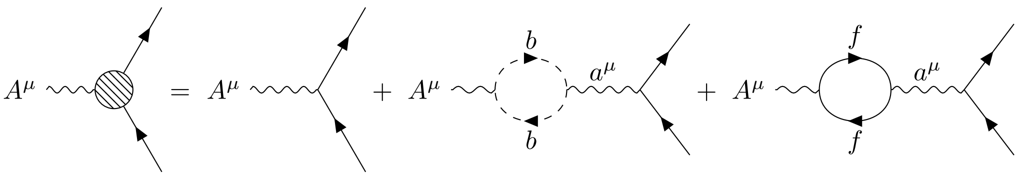

Figure 4.8: The diagrams that contribute to the renormalized charge. The propagators and polarization bubbles are all fully dressed. A^μ is the external gauge field, a^μ is the emergent gauge field, and the lines to the right of the diagrams are either b or f propagators depending on whether the renormalized b charge or renormalized f charge is being computed.

4.9 Derivation of the Ioffe-Larkin Condition for Model I

The Kubo formula allows us to evaluate the conductivity tensors for the three species. To find the total conductivity, however, we must combine the contribution from the three species. Although the c fermions are a separate species and will be added in parallel to the b and f contribution, the latter two species add together in series instead of in parallel due to the Ioffe-Larkin composition rule. In this section, we will derive the Ioffe-Larkin composition rule closely following Lee and Nagaosa [87]. Our derivation is exact in the large N limit.

Due to the emergent gauge field, the charge of the b bosons and f fermions is renormalized. The physical condition is that $e_b + e_f = -1$ as the $bfc^\dagger$ term in the Lagrangian must conserve charge. How the charge is distributed is a gauge choice, with the emergent gauge field ensuring the physical results are independent of this choice.

We see in Fig. 4.8 that there are three diagrams that contribute to the renormalization of the charge. In the diagrams, the polarization bubbles, $\mathbf{\Pi}$, [5] and propagators are fully renormalized (with the fermionic spin degeneracy included). Any other diagram is either zero because of the locality of the SYK-type interaction or suppressed by $1/N$. We note that the propagator for the emergent $U(1)$ gauge field is [87]

$$\boldsymbol{D}(\tau - \tau') = -\langle a(\tau)a(\tau')\rangle = -(\mathbf{\Pi}_f + \mathbf{\Pi}_b)^{-1}, \tag{4.67}$$

and the boldface is indicating tensors, which follows if the inverse bare propagator is taken to be infinitesimal.

Summing these diagrams for, e.g. the f fermions gives

$$\begin{aligned} \boldsymbol{e}_f^r &= e_f - e_f\mathbf{\Pi}_f(\mathbf{\Pi}_f + \mathbf{\Pi}_b)^{-1} + e_b\mathbf{\Pi}_b(\mathbf{\Pi}_f + \mathbf{\Pi}_b)^{-1} \\ &= (e_f + e_b)\mathbf{\Pi}_b(\mathbf{\Pi}_f + \mathbf{\Pi}_b)^{-1} = -\mathbf{\Pi}_b(\mathbf{\Pi}_f + \mathbf{\Pi}_b)^{-1}, \end{aligned} \tag{4.68}$$

where the extra minus sign for $\mathbf{\Pi}_b$ comes because f and b are oppositely charged under the emergent gauge field, and all polarization bubbles are evaluated at (ω, q). Switching $f \leftrightarrow b$ will give the boson result. Therefore, the charge renormalizes to become a tensor. It is worth noting that $\mathbf{\Pi}_b$, $\mathbf{\Pi}_f$, and

---

[5] The polarization bubbles $\mathbf{\Pi}_{f,b}$ involve the subtraction of diamagnetic terms not explicitly shown in Fig. 4.8, which render $\mathbf{\Pi}_{f,b}(\omega, q) = \mathbf{\Pi}_{f,b}(\omega, q) - \mathbf{\Pi}_{f,b}(\omega = 0, q = 0)$

$\mathbf{\Pi}_b + \mathbf{\Pi}_f$ are 2×2 antisymmetric matrices and therefore commute with each other. When we compute the total current-current correlator due to the f and b sub-systems after renormalizing the currents using the respective charge renormalizations. We find, since there are no current cross-correlations, as discussed in the main text,

$$\begin{aligned}\mathbf{\Pi}_{\text{tot}} &= \mathbf{\Pi}_b \mathbf{\Pi}_f^2[(\mathbf{\Pi}_b + \mathbf{\Pi}_f)^{-1}]^2 + \mathbf{\Pi}_f \mathbf{\Pi}_b^2[(\mathbf{\Pi}_b + \mathbf{\Pi}_f)^{-1}]^2 \\ &= (\mathbf{\Pi}_b^{-1} + \mathbf{\Pi}_f^{-1})^{-1},\end{aligned} \tag{4.69}$$

which implies that the f and b resistivity are added in series.

One important point that is glossed over in the above is that the electric and magnetic field are renormalized differently, and $\mathbf{\Pi}_b$ and $\mathbf{\Pi}_f$ are evaluated for different effective magnetic fields. In our notation, $\mathbf{\Pi}(\omega, q) \approx -i\boldsymbol{\sigma}\omega + \boldsymbol{\chi} q^2$, so the renormalization changes depending on whether the vertex is magnetic $A^\mu(\omega = 0, q \to 0)$, or electric, $A^\mu(\omega \to 0, q = 0)$. We find, for instance for the f fermions

$$E_{\text{eff}}^f = \boldsymbol{\sigma}_b(\boldsymbol{\sigma}_f + \boldsymbol{\sigma}_b)^{-1}E, \qquad B_{\text{eff}}^f = \frac{\chi_b}{\chi_b + \chi_f}B, \tag{4.70}$$

for a weak magnetic field B. In the magnetic field case, we additionally average over q, which replaces $\boldsymbol{\chi}$ with half its trace $\chi = (\chi_{xx} + \chi_{yy})/2$.

In our derivation, we have neglected contributions to $\boldsymbol{\sigma}$ and $\boldsymbol{\chi}$ from potential cross-correlations $_{fb} \sim \langle J_f J_b \rangle$. Doing so is valid, as Model I's site-uncorrelated g_{ijk}^r render them of the form

$$\begin{aligned}&{}_{fb}(i\omega, q) \sim \int d^2k d^2k' d\Omega d\Omega' v_{f,k} v_{b,k} G_{f,k+q/2}(i\Omega + i\omega/2) G_{f,k-q/2}(i\Omega - i\omega/2) K_{fb}(i\Omega, i\Omega', \omega, q) \\ &\times G_{b,k'+q/2}(i\Omega' + i\omega/2) G_{b,k'-q/2}(i\Omega' - i\omega/2),\end{aligned} \tag{4.71}$$

where $v_{x,k} = \nabla_k \epsilon_{x,k}$. Since $G_{x,k} = G_{x,-k}$, $G_{x,k+q/2}(i\Omega + i\omega/2) G_{x,k-q/2}(i\Omega - i\omega/2) = G_{x,k}(i\Omega + i\omega/2) G_{x,k}(i\Omega - i\omega/2) + \Xi_{x,k}(i\Omega, i\omega)|q|^2$, with $\Xi_{x,k} = \Xi_{x,-k}$, and $v_{x,k} = -v_{x,-k}$, the $\mathcal{O}(\omega)$ and $\mathcal{O}(q^2)$ terms in the expansion of $_{fb}(\omega, q)$ vanish and we can thus neglect these cross-correlations.

4.10 Diamagnetic Susceptibilities in Model I

Because of the renormalization of the magnetic field from the internal gauge field, we must find expressions for χ_f and χ_b. To find them, we evaluate $\chi_\lambda q^2 = \Pi_\lambda(\omega = 0, q \to 0) - \Pi_\lambda(\omega = 0, q = 0)$. We average the two possible directions. Then, we have the bubble contributions (vertex corrections vanish for the same reason as (4.71) does)

$$\begin{aligned}&\Pi_\lambda(q \to 0) = \frac{\Pi_{\lambda,xx} + \Pi_{\lambda,yy}}{2} = -\eta \frac{1}{V} \sum_k \frac{k^2}{2m_\lambda^2} T \sum_{i\nu} \left(G_\lambda(k - q/2, i\nu) G_\lambda(k + q/2, i\nu)\right) \\ &= -2\eta T \int_0^{\tilde{k}_{\max}} \frac{d\tilde{k}}{(2\pi)^2} \int_0^{2\pi} d\theta \tilde{k}^3 \left(\sum_{i\nu} \frac{1}{(i\nu/T - \tilde{k}^2 + \tilde{k}\tilde{q}\cos(\theta) - \tilde{q}^2/4 + \mu_\lambda/T - \Sigma_\lambda/T)} \frac{1}{(\tilde{q} \to -\tilde{q})} \right) \\ &\chi_\lambda = -\eta \frac{1}{2m_\lambda} \int_0^{k_{\max}} k^3 \frac{dk}{2\pi} \left(\sum_{i\nu} \frac{(i\nu_\lambda/T + \mu/T - \Sigma_\lambda/T)}{(i\nu/T - k^2 + \mu_\lambda/T - \Sigma_\lambda/T)^4} \right),\end{aligned} \tag{4.72}$$

where in the second line of the above, we re-scaled the momenta by a factor of $\tilde{k} = k/\sqrt{2m_\lambda T}$, and we relabeled $\tilde{k} \to k$ in line 3.

We can do the Matsubara sums exactly in the bosonic case since $\Sigma_b(i\omega) = -\gamma|\omega|$. We carry them out to find ($z = -\mu/T = \Delta_b/T$):

$$\chi_b = -\frac{1}{2m_b}\int_0^{\sqrt{\Lambda/T}} \frac{dk}{2\pi} k^3 \left(\frac{z}{(k^2+z)^4} + \mathrm{Re}\left[\frac{\psi_2\left(\frac{k^2+z}{2\pi\gamma - 2\pi i}\right)}{(2\pi\gamma - 2\pi i)^3} + \frac{k^2}{3}\frac{\psi_3\left(\frac{k^2+z}{2\pi\gamma - 2\pi i}\right)}{(2\pi\gamma - 2\pi i)^4} \right] \right), \tag{4.73}$$

with $\psi_n(z)$ the polygamma function and Λ is the boson bandwidth. This expression diverges as $\chi_b \sim (1/m_b)\ln(\Lambda/\Delta_b)$ when $\Delta_b \to 0$.

For the f fermions, we can transform (4.72) to

$$\begin{aligned} \chi_f &= \frac{1}{2m_f}\int_{-\mu_f}^{\Lambda_f} \frac{d\epsilon}{2\pi}(\epsilon + \mu_f) T \sum_{i\nu} \left(\frac{(i\nu + \mu_f - \Sigma_f(i\nu))}{(i\nu - \epsilon - \Sigma_f(i\nu))^4} \right) \\ &= T\sum_{i\nu} \frac{(\Lambda_f + \mu_f)^2(\Lambda_f - 2\mu_f + 3\Sigma_f(i\nu) - 3i\nu)}{24\pi m_f(\Lambda_f + \Sigma_f(i\nu) - i\nu)^3(\mu_f - \Sigma_f(i\nu) + i\nu)}. \end{aligned} \tag{4.74}$$

We note that T and $|\Sigma_f(i\nu)|$ are always much smaller than the f bandwidth Λ_f and Fermi energy μ_f, for any value of ν, since $|\Sigma_f(i\nu)|$ is bounded by a scale controlled by the boson bandwidth $\Lambda \ll \Lambda_f, \mu_f$. Therefore we can expand the summand of (4.74) in powers of Σ_f and take the $T \to 0$ limit. It may then be seen that the sum of the absolute values of the contributions from all these terms in the expansion is bounded by a quantity that vanishes in the limit of $\Lambda_f, \mu_f \to \infty$, leaving χ_f to take its free fermion value of $1/(24\pi m_f)$, which can be easily verified by inserting the result for $\Sigma_f(i\nu)$ and then numerically integrating over ν in this limit.

4.11 Inter-Layer Instabilities in Model I

Using the expressions from the previous sections, we can find ρ_{xx} and R_H exactly for a 2D version of Model I without inter-layer couplings, for all values of parameters at small B. For the same parameters used in the main text, we plot R_H and ρ_{xx} in Fig. 4.9 while ignoring inter-layer couplings, which should be compared with Fig. 4.2 in the main text that takes inter-layer couplings into account. Note the large enhancement of R_H seen at low temperatures when $\kappa > \kappa_c$, as also seen in Fig. 4.4 in the main text.

Despite the exact solvability of Model I in its 2D version described here, to make physical predictions we must analyze possible instabilities that will take us away from our solution. In the 2D version of Model I, the only possible instabilities at large N are BCS-like fermion pairing instabilities, induced by adding weak attractive interactions, which occur at exponentially small energy scales and which we hence ignore. However, the physical version of Model I includes a third spatial dimension, and we should therefore ask what relevant inter-layer interactions are allowed and what their impact on the physics will be.

An important feature of the physical version of Model I is that the b and f partons are deconfined in a stack of independent 2D layers. We can therefore write down the following large N, instability inducing [110], local, gauge-invariant, quartic interactions between adjacent layers l and l', where r denotes the 2D coordinate of a site within a layer:

$$\begin{aligned} H_{bb} &= -\frac{J_b}{N}\sum_{i,j=1}^{N}\sum_{r} b^\dagger_{r(l),i}b_{r(l'),i}b^\dagger_{r(l'),j}b_{r(l),j}, \\ H'_{bb} &= -\frac{J'_b}{N}\sum_{i,j=1}^{N}\sum_{r} b^\dagger_{r(l),i}b^\dagger_{r(l'),i}b_{r(l'),j}b_{r(l),j}, \end{aligned} \tag{4.75}$$

$$\begin{aligned} H_{ff} &= -\frac{J_f}{N}\sum_{i,j=1}^{N}\sum_{\substack{r,\sigma,\sigma',\\ \tau,\tau'}} f^\dagger_{r(l),i,\sigma}f^\dagger_{r(l'),i,\sigma'}f_{r(l'),j,\tau}f_{r(l),j,\tau'}, \\ H_{bf} &= -\frac{J_{bf}}{N}\sum_{i,j=1}^{N}\sum_{r,\sigma}\left[b^\dagger_{r(l),i}b_{r(l'),i}f^\dagger_{r(l),j,\sigma}f_{r(l'),j,\sigma} + \text{H.c}\right]. \end{aligned}$$

None of these terms contribute directly to the parton self-energies or transport at large N. H_{ff} induces BCS-like inter-layer f fermion pairing instabilities, which occur at exponentially small energy scales, and are therefore not of concern to us. The terms in H_{bb} create inter-layer boson instabilities driven by susceptibilities that scale as $\sim m_b J'_b \ln(\Lambda/\Delta_b)$. In the gapped phase of the boson, and in the quantum critical region, these susceptibilities are thus small at the temperature scales of interest, hence we ignore them. However, for $\kappa > \kappa_c$, $\Delta_b(T)$ starts decreasing rapidly below some temperature scale (Fig. 4.6), which makes these susceptibilities large, causing the onset of instabilities that lead to the condensation of inter-layer boson bilinears in the gray region of Fig. 4.2 in the main text. The resulting 3D boson phase will then further have single-boson condensation as temperature is lowered [131], entering the region below the gray wedge. Once this happens, both the partons will have 3D dispersions as these boson interaction terms will appear like inter-layer hoppings, $b^\dagger_l b^\dagger_{l'} b_l b_{l'} \sim c_b b^\dagger_l b_{l'}$, and H_{bf} will similarly generate inter-layer hopping for the f fermions [6]. This leads to two important changes to the model; first the partons develop an anisotropic dispersion with hopping proportional to the single-boson condensate strength at temperatures well below the gray wedge, second the fermions now scatter off both the $N-1$ critical bosons $b_{2,..,N}$ as well as the condensed mode $\langle b_1\rangle$.

To model these effects, the dispersion of the partons is changed to be

$$\epsilon_{b/f,k} = \frac{1}{2m_{b/f}}(k_x^2 + k_y^2 + Y_{b/f}k_z^2), \quad Y_{b/f} = 4\pi^2 J_{b/bf} r_0^2, \tag{4.76}$$

where r_0 is the size of the condensate. For Fig. 4.2 in the main text we take $J_b = 1$. Rewriting the SD equations within the condensed phase, the only changes are to the fermion self-energy and the constraint. The constraint equation becomes

$$\kappa - \kappa_c = r_0^2 + (n_b - n_b^c), \tag{4.77}$$

---

[6] H'_{bb} will also generate inter-layer boson pairing terms $\sim c'_b b^\dagger_l b^\dagger_{l'}$, but the Hugenholtz-Pines theorem [63] nevertheless ensures a 3D gapless boson phase, with the same effects on the fermions.

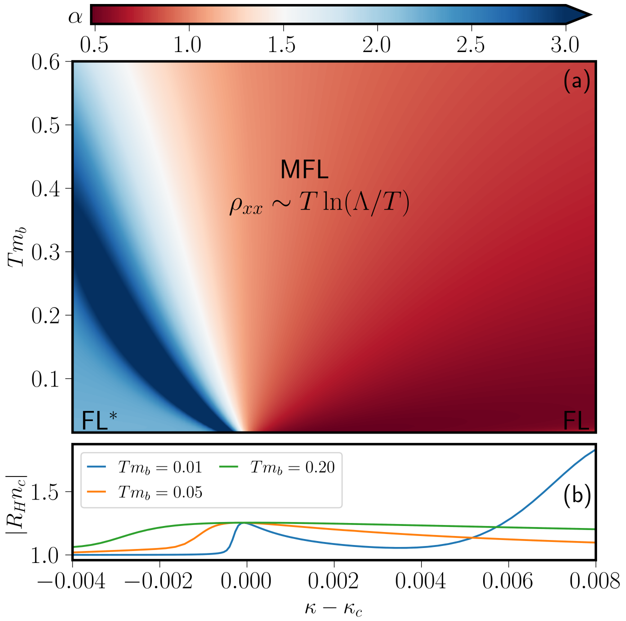

Figure 4.9: (a) The phase diagram for Model I in 2D with no inter-layer instabilities. The resistivity is given by $\rho_{xx} - \rho_{xx}(T = 0) \sim T^\alpha \ln(\Lambda/T)$, and the color indicates the value of $\alpha = d\ln(\rho_{xx}/\ln(\Lambda/T))/d\ln(T)$. (b) The plot of the weak-field R_H vs. $\kappa - \kappa_c$. R_H has a peak near the crossover from Fermi-liquid behavior to T-linear resistivity and approaches a constant to either side signaling the change in carrier density. The large peak of R_H seen at low temperatures is occurring as the boson is condensing, as discussed in the main text. The same parameters are used as in Fig. 4.2 in the main text.

where, in this equation, n_b is the number of bosons not participating in the condensate with $\Delta_b = 0$, and using the self-consistently determined dispersion. The self-energy expression is changed to be

$$\begin{aligned}\mathrm{Im}[\Sigma_{c,R}] = {} & -r_0^2 g^2 \frac{\nu_f}{2} \\ & - g^2 \frac{\nu_f}{4\pi} \int_{-\infty}^{\infty} d\epsilon \bar{A}_b(\epsilon)(n_B(\epsilon) + n_F(\epsilon - \omega)),\end{aligned} \tag{4.78}$$

with $\tilde{A}_b$ the spectral function of the uncondensed modes.

To keep the number of f fermions fixed, as the dispersion changes, the Fermi energy shifts which in turn modifies the density of states. In order to connect with the 2D model, we introduce a maximum momentum in the z direction, K. The spinless density of states is then given by

$$\nu_f = \begin{cases} \frac{K m_f}{\pi} & \epsilon_F^0 > \frac{Y_f K^2}{3 m_f} \\ \frac{m_f}{\pi} \left(\frac{3\epsilon_F^0 K m_f}{c_f} \right)^{1/3} & \epsilon_F^0 < \frac{Y_f K^2}{3 m_f} \end{cases}, \tag{4.79}$$

where $\epsilon_{F,0}$ is the Fermi energy with $Y_f = 0$. Note that we take $K = \pi$ so the density of states in the small condensate regime is $\nu_f = m_f$, the same as in the purely 2D case. We will work in the regime where the second condition of (4.79) is never reached, this is achieved by taking J_{bf} sufficiently small. If the second condition was achieved, $\gamma = g^2\nu_c\nu_f/(2\pi)$ would change.

The spectral function for the uncondensed modes can be evaluated utilizing the 2D results by replacing $\Delta_b \to \Delta_b + Y_b k_z^2/(2m_b)$ in (4.55) to find

$$\frac{2\pi}{m_b}\tilde{A}_b(\omega,0) = K\mathrm{sgn}(\omega) - \frac{2K}{\pi}\tan^{-1}\left(\frac{Y_bK^2}{4\gamma m_b\omega} - \frac{1}{\gamma}\right) \tag{4.80}$$
$$- \frac{4}{\pi Y_b}\mathrm{Im}\left[\sqrt{2(1+i\gamma)\omega m_b}\tanh^{-1}\left(\frac{Y_bK}{\sqrt{2m_b(1+i\gamma)\omega}}\right)\right].$$

Unlike the $O(N)$ rotor model, the dispersion is also modified as the condensate grows. This changing dispersion results in a different temperature dependence when $Tm_b \gg \kappa - \kappa_c$ and also results in multiple self-consistent values of the condensate size r_0 at fixed κ and T. If we assume interactions which generate a 3D instability at $T = 0$, the physical solution for r_0 is the one that approaches a non-zero constant at low temperatures, which is the one we use in our numerical calculations.

Deep in the condensed phase at low temperatures, r_0 will be roughly constant and large. In this regime, the frequency dependence of the spectral function for the uncondensed boson modes then goes as as $\sqrt{\omega}$, leading directly to $\mathrm{Im}[\Sigma_{c,R}(\omega=0,T)] \sim T^{3/2} + \mathrm{const.}$ behavior.

4.12 Self-Energies and Critical Transport in Model II

To evaluate the boson self-energy we start with the individual patch contribution (4.36). Integration over $q_\perp$ yields (using $v_{c,f,F} = k_F/m_{c,f}$, where k_F is the Fermi momentum)

$$\Sigma_b^p(i\omega,k) = -ig^2T\sum_{i\nu}\int\frac{d^2q_\parallel}{(2\pi)^2}\left(\mathrm{sgn}(\nu+\omega) - \mathrm{sgn}(\nu)\right)$$
$$\times\left[v_{f,F}\left(i(\nu+\omega) - \Sigma_c(i\nu+i\omega) - v_{c,F}k_\perp - \frac{k_\parallel q_\parallel\cos(\theta)}{2m_c} - \frac{k_\parallel^2}{2m_c}\right) - v_{c,F}\left(i\nu - \Sigma_f(i\nu)\right)\right]^{-1}, \tag{4.81}$$

where θ is the angle between $q_\parallel$ and $k_\parallel$. This further reduces upon integration over θ to

$$\Sigma_b^p(i\omega,k) = -\frac{ig^2}{2\pi}T\times$$
$$\sum_{i\nu}\int_0^{q_{\max}}\frac{q_\parallel dq_\parallel\ \left(\mathrm{sgn}(\nu+\omega) - \mathrm{sgn}(\nu)\right)}{v_{f,F}(i(\nu+\omega) - \Sigma_c(i\nu+i\omega)) - v_{c,F}(i\nu - \Sigma_f(i\nu)) - \frac{v_{f,F}k_\parallel q_\parallel}{2m_c} - v_{c,F}v_{f,F}k_\perp - \frac{v_{f,F}k_\parallel^2}{2m_c}}$$
$$\times\frac{1}{\sqrt{1 + \frac{\frac{v_{f,F}k_\parallel q_\parallel}{m}}{v_{f,F}(i(\nu+\omega) - \Sigma_c(i\nu+i\omega)) - v_{c,F}(i\nu - \Sigma_f(i\nu)) - \frac{v_{f,F}k_\parallel q_\parallel}{2m} - v_{c,F}v_{f,F}k_\perp - \frac{v_Fk_\parallel^2}{2m}}}}$$
$$\approx\frac{g^2q_{\max}m_c}{\pi^2v_{f,F}}\frac{|\omega|}{k_\parallel} = \frac{g^2q_{\max}m_cm_f}{\pi^2k_F}\frac{|\omega|}{k_\parallel}.$$

Here the cutoff $q_{\max} \sim k_F \; d\Omega$, where $d\Omega$ is the solid angle subtended by the patch, is the cutoff on the patch size. If we now average over all patches, we obtain

$$\Sigma_b(i\omega, k) \approx -\int_0^{2\pi} d\phi \int_0^{\pi} \sin\theta d\theta \; \frac{g^2 m_c m_f}{\pi^2} \frac{|\omega|}{k\sin\theta} = -2g^2 m_c m_f \frac{|\omega|}{k} \equiv -\gamma_2 \frac{|\omega|}{k}. \tag{4.82}$$

We now discuss the fermion self-energies (4.40) at criticality. There, the c, f self-energies are expected to show MFL frequency dependence because of the log divergence of the momentum integral over $q_{\parallel}$. As mentioned at the end of Sec. 4.4.3 in the main text, in this Appendix, we are interested in the higher temperature regime where the boson is not that strongly damped, so we do *not* ignore the $i\nu$ term in the boson propagator in (4.40) while computing the fermion self-energies. The Matsubara frequency sum can then be separated into a UV divergent piece, that is a constant and which may be absorbed by a chemical potential shift, and a UV finite piece, which may be computed analytically. Then we can compute the momentum integral numerically with a UV cutoff $\sim \sqrt{2m_b\Lambda}$ to obtain

$$\Sigma_{c,f}(i\omega) \approx \text{const.} - \frac{i\gamma_2 m_b}{m_{c,f} k_F} T \tilde{\varphi}\left(\frac{\omega}{T}, \frac{\Lambda}{T}, \frac{\Lambda}{\Delta_b(T)}\right). \tag{4.83}$$

where the function $\tilde{\varphi}$ is no longer symmetric between $\pm\omega$ in the higher energy regime $\Lambda \gg \omega, T \gg \gamma_2^2/m_b$, where the $i\nu$ term in the boson propagator in (4.40) is dominant.

In this higher temperature (energy) regime, the small wavevectors in the boson propagator are cut off by temperature as $q_{\parallel}^2 \sim m_b T$ (by comparison of $q_{\parallel}^2/(2m_b)$ to the $i\nu$ term), and the boson self-energy $\gamma_2|\nu|/q_{\parallel}$ (which we now treat as a perturbation), may therefore be approximated to be $\sim \gamma_2|\nu|/\sqrt{m_b T}$ in (4.40). Model II then behaves similarly to Model I at small γ, with $\gamma \sim \gamma_2/\sqrt{m_b T}$, from the point of view of the fermions. Then, by virtue of (4.27, 4.29), we have $\rho_{xx}(T) \sim \sqrt{T}$ (up to log corrections), and $|R_H n_c| \to 4/3$.

In Fig. 4.10 we show the crossover between the strongly damped low-temperature regime and the weakly damped higher temperature regime over the QCP, by exact numerical calculation of the conduction electron bubble diagram contribution to the conductivity tensor. As we also argued for the case of Model I, this bubble diagram is still the dominant contribution at criticality. Indeed, the contribution of the f fermions and the bosons are still suppressed even in the higher energy regime of Model II (that is similar to the $\gamma \ll 1$ regime of Model I), due to the relatively low conductivity of the bosons.

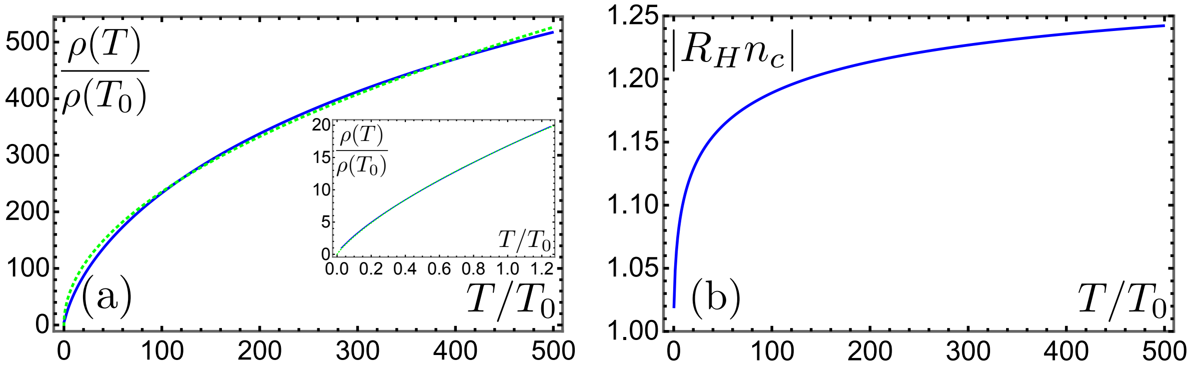

Figure 4.10: (a) Temperature dependence of ρ_{xx} over the QCP in Model II. The dashed green lines indicate fits to $\rho(T)/\rho(T_0) = a_1\sqrt{T/T_0}$ and $\rho(T)/\rho(T_0) = a_2(T/T_0)\ln(a_3T_0/T)$ in the main and inset plots respectively (b) Temperature dependence of R_H in Model II. We use $\gamma_2 = 0.02$, $m_b = 1.0$, the crossover scale $T_0 = \gamma_2^2/m_b = 4 \times 10^{-4}$, and the boson bandwidth $\Lambda = \pi^2/2 \approx 1.23 \times 10^4\ T_0$. The bandwidths of the conduction electrons and f fermions are assumed to be very large.

Bibliography

[1] A. A. Abrikosov. “Electron scattering on magnetic impurities in metals and anomalous resistivity effects”. In: *Physics Physique Fizika* 2 (1 Sept. 1965), pp. 5–20. DOI: 10.1103/PhysicsPhysiqueFizika.2.5. URL: https://link.aps.org/doi/10.1103/PhysicsPhysiqueFizika.2.5.

[2] Ian Affleck et al. “SU(2) gauge symmetry of the large-U limit of the Hubbard model”. In: *Phys. Rev. B* 38 (1 July 1988), pp. 745–747. DOI: 10.1103/PhysRevB.38.745. URL: https://link.aps.org/doi/10.1103/PhysRevB.38.745.

[3] Y. Aharonov and D. Bohm. “Significance of Electromagnetic Potentials in the Quantum Theory”. In: *Phys. Rev.* 115 (3 Aug. 1959), pp. 485–491. DOI: 10.1103/PhysRev.115.485. URL: https://link.aps.org/doi/10.1103/PhysRev.115.485.

[4] Erik E. Aldape et al. “Solvable theory of a strange metal at the breakdown of a heavy Fermi liquid”. In: *Phys. Rev. B* 105 (23 June 2022), p. 235111. DOI: 10.1103/PhysRevB.105.235111. URL: https://link.aps.org/doi/10.1103/PhysRevB.105.235111.

[5] P W Anderson. “A poor man’s derivation of scaling laws for the Kondo problem”. In: *Journal of Physics C: Solid State Physics* 3.12 (Dec. 1970), p. 2436. DOI: 10.1088/0022-3719/3/12/008. URL: https://dx.doi.org/10.1088/0022-3719/3/12/008.

[6] P. W. Anderson. “More Is Different”. In: *Science* 177.4047 (1972), pp. 393–396. DOI: 10.1126/science.177.4047.393. eprint: https://www.science.org/doi/pdf/10.1126/science.177.4047.393. URL: https://www.science.org/doi/abs/10.1126/science.177.4047.393.

[7] P. W. Anderson and G. Yuval. “Exact Results in the Kondo Problem: Equivalence to a Classical One-Dimensional Coulomb Gas”. In: *Phys. Rev. Lett.* 23 (2 July 1969), pp. 89–92. DOI: 10.1103/PhysRevLett.23.89. URL: https://link.aps.org/doi/10.1103/PhysRevLett.23.89.

[8] P. W. Anderson, G. Yuval, and D. R. Hamann. “Exact Results in the Kondo Problem. II. Scaling Theory, Qualitatively Correct Solution, and Some New Results on One-Dimensional Classical Statistical Models”. In: *Phys. Rev. B* 1 (11 June 1970), pp. 4464–4473. DOI: 10.1103/PhysRevB.1.4464. URL: https://link.aps.org/doi/10.1103/PhysRevB.1.4464.

[9] P.W. Anderson. “Resonating valence bonds: A new kind of insulator?” In: *Materials Research Bulletin* 8.2 (1973), pp. 153–160. ISSN: 0025-5408. DOI: `https://doi.org/10.1016/0025-5408(73)90167-0`. URL: `https://www.sciencedirect.com/science/article/pii/0025540873901670`.

[10] P.W. Anderson. *Valence fluctuations in solids : Santa Barbara Institute for Theoretical Physics Conferences, Santa Barbara, California, January 27-30, 1981 / edited by L.M. Falicov, W. Hanke, M.B. Maple.* North-Holland ; Sole distributors for the U.S.A. and Canada, Elsevier North-Holland Amsterdam ; New York : New York, 1981, p. 451. ISBN: 0444862048.

[11] K. Andres, J. E. Graebner, and H. R. Ott. “$4f$-Virtual-Bound-State Formation in $CeAl_3$ at Low Temperatures”. In: *Phys. Rev. Lett.* 35 (26 Dec. 1975), pp. 1779–1782. DOI: `10.1103/PhysRevLett.35.1779`. URL: `https://link.aps.org/doi/10.1103/PhysRevLett.35.1779`.

[12] Daniel Arovas, J. R. Schrieffer, and Frank Wilczek. “Fractional Statistics and the Quantum Hall Effect”. In: *Phys. Rev. Lett.* 53 (7 Aug. 1984), pp. 722–723. DOI: `10.1103/PhysRevLett.53.722`. URL: `https://link.aps.org/doi/10.1103/PhysRevLett.53.722`.

[13] Daniel P. Arovas and Assa Auerbach. “Functional integral theories of low-dimensional quantum Heisenberg models”. In: *Phys. Rev. B* 38 (1 July 1988), pp. 316–332. DOI: `10.1103/PhysRevB.38.316`. URL: `https://link.aps.org/doi/10.1103/PhysRevB.38.316`.

[14] Assa Auerbach and K Levin. “Kondo bosons and the Kondo lattice: Microscopic basis for the heavy Fermi liquid”. In: *Physical review letters* 57.7 (1986), p. 877. URL: `https://journals.aps.org/prl/abstract/10.1103/PhysRevLett.57.877`.

[15] S.-H. Baek et al. “Evidence for a Field-Induced Quantum Spin Liquid in α-$RuCl_3$”. In: *Phys. Rev. Lett.* 119 (3 July 2017), p. 037201. DOI: `10.1103/PhysRevLett.119.037201`. URL: `https://link.aps.org/doi/10.1103/PhysRevLett.119.037201`.

[16] F. A. Bais, B. J. Schroers, and J. K. Slingerland. “Broken Quantum Symmetry and Confinement Phases in Planar Physics”. In: *Phys. Rev. Lett.* 89 (18 Oct. 2002), p. 181601. DOI: `10.1103/PhysRevLett.89.181601`. URL: `https://link.aps.org/doi/10.1103/PhysRevLett.89.181601`.

[17] A Banerjee et al. “Proximate Kitaev quantum spin liquid behaviour in a honeycomb magnet”. In: *Nature Materials* (2016).

[18] Arnab Banerjee et al. “Excitations in the field-induced quantum spin liquid state of α-RuCl 3”. In: *npj Quantum Materials* 3.1 (2018), pp. 1–7.

[19] Arnab Banerjee et al. “Neutron scattering in the proximate quantum spin liquid α-RuCl3”. In: *Science* 356.6342 (2017), pp. 1055–1059.

[20] D. M. Basko. “Resonant low-energy electron scattering on short-range impurities in graphene”. In: *Phys. Rev. B* 78 (11 Sept. 2008), p. 115432. DOI: `10.1103/PhysRevB.78.115432`. URL: `https://link.aps.org/doi/10.1103/PhysRevB.78.115432`.

[21] Erez Berg et al. “Monte Carlo studies of quantum critical metals”. In: *Annual Review of Condensed Matter Physics* 10 (2019), pp. 63–84.

[22] Zhen Bi et al. “Instability of the non-Fermi-liquid state of the Sachdev-Ye-Kitaev model”. In: *Phys. Rev. B* 95 (20 May 2017), p. 205105. DOI: `10.1103/PhysRevB.95.205105`. URL: `https://link.aps.org/doi/10.1103/PhysRevB.95.205105`.

[23] A Biffin et al. “Noncoplanar and Counterrotating Incommensurate Magnetic Order Stabilized by Kitaev Interactions in γ- Li 2 IrO 3”. In: *Physical Review Letters* 113.19 (2014), p. 197201.

[24] Parsa Bonderson, Michael Freedman, and Chetan Nayak. “Measurement-Only Topological Quantum Computation”. In: *Phys. Rev. Lett.* 101 (1 June 2008), p. 010501. DOI: `10.1103/PhysRevLett.101.010501`. URL: `https://link.aps.org/doi/10.1103/PhysRevLett.101.010501`.

[25] Parsa Bonderson, Michael Freedman, and Chetan Nayak. “Measurement-only topological quantum computation via anyonic interferometry”. In: *Annals of Physics* 324.4 (2009), pp. 787–826. ISSN: 0003-4916. DOI: `https://doi.org/10.1016/j.aop.2008.09.009`. URL: `https://www.sciencedirect.com/science/article/pii/S0003491608001577`.

[26] G. Breit and E. Wigner. “Capture of Slow Neutrons”. In: *Phys. Rev.* 49 (7 Apr. 1936), pp. 519–531. DOI: `10.1103/PhysRev.49.519`. URL: `https://link.aps.org/doi/10.1103/PhysRev.49.519`.

[27] J. A. N. Bruin et al. “Similarity of Scattering Rates in Metals Showing T-Linear Resistivity”. In: *Science* 339.6121 (2013), pp. 804–807. ISSN: 0036-8075. DOI: `10.1126/science.1227612`. eprint: `https://science.sciencemag.org/content/339/6121/804.full.pdf`. URL: `https://science.sciencemag.org/content/339/6121/804`.

[28] Yuan Cao et al. “Strange metal in magic-angle graphene with near Planckian dissipation”. In: *Phys. Rev. Lett.* 124 (7 Feb. 2020), p. 076801. DOI: `10.1103/PhysRevLett.124.076801`. URL: `https://link.aps.org/doi/10.1103/PhysRevLett.124.076801`.

[29] Andrea Cappelli, Marina Huerta, and Guillermo R. Zemba. “Thermal transport in chiral conformal theories and hierarchical quantum Hall states”. In: *Nuclear Physics B* 636.3 (2002), pp. 568–582. ISSN: 0550-3213. DOI: `https://doi.org/10.1016/S0550-3213(02)00340-1`. URL: `https://www.sciencedirect.com/science/article/pii/S0550321302003401`.

[30] Jiří Chaloupka, George Jackeli, and Giniyat Khaliullin. “Kitaev-Heisenberg model on a honeycomb lattice: possible exotic phases in iridium oxides A 2 IrO 3”. In: *Physical Review Letters* 105.2 (2010), p. 027204.

[31] SK Choi et al. "Spin waves and revised crystal structure of honeycomb iridate Na 2 IrO 3". In: *Physical review letters* 108.12 (2012), p. 127204.

[32] Debanjan Chowdhury et al. "Sachdev-Ye-Kitaev models and beyond: Window into non-Fermi liquids". In: *Rev. Mod. Phys.* 94 (3 Sept. 2022), p. 035004. DOI: 10.1103/RevModPhys.94.035004. URL: https://link.aps.org/doi/10.1103/RevModPhys.94.035004.

[33] Sae Hwan Chun et al. "Direct evidence for dominant bond-directional interactions in a honeycomb lattice iridate Na2IrO3". In: *Nature Physics* 11.6 (2015), pp. 462–466.

[34] P. Coleman, I. Paul, and J. Rech. "Sum rules and Ward identities in the Kondo lattice". In: *Phys. Rev. B* 72 (9 Sept. 2005), p. 094430. DOI: 10.1103/PhysRevB.72.094430. URL: https://link.aps.org/doi/10.1103/PhysRevB.72.094430.

[35] Piers Coleman. "Heavy fermions: electrons at the edge of magnetism". In: *Handbook of magnetism and advanced magnetic materials* (2007). URL: https://onlinelibrary.wiley.com/doi/abs/10.1002/9780470022184.hmm105.

[36] Piers Coleman. "New approach to the mixed-valence problem". In: *Physical Review B* 29.6 (1984), p. 3035. URL: https://journals.aps.org/prb/abstract/10.1103/PhysRevB.29.3035.

[37] C. Collignon et al. "Thermopower across the phase diagram of the cuprate LaNdSrCuO: Signatures of the pseudogap and charge density wave phases". In: *Phys. Rev. B* 103 (15 Apr. 2021), p. 155102. DOI: 10.1103/PhysRevB.103.155102. URL: https://link.aps.org/doi/10.1103/PhysRevB.103.155102.

[38] J.h.p. Colpa. "Diagonalization of the quadratic boson hamiltonian". In: *Physica A: Statistical Mechanics and its Applications* 93.3-4 (1978), pp. 327–353. DOI: 10.1016/0378-4371(78)90160-7.

[39] A Comtet, Y Georgelin, and S Ouvry. "Statistical aspects of the anyon model". In: *Journal of Physics A: Mathematical and General* 22.18 (Sept. 1989), p. 3917. DOI: 10.1088/0305-4470/22/18/026. URL: https://dx.doi.org/10.1088/0305-4470/22/18/026.

[40] R. A. Cooper et al. "Anomalous Criticality in the Electrical Resistivity of $La_{2-x}Sr_xCuO_4$". In: *Science* 323.5914 (Jan. 2009), p. 603. DOI: 10.1126/science.1165015.

[41] B. Coqblin and J. R. Schrieffer. "Exchange Interaction in Alloys with Cerium Impurities". In: *Phys. Rev.* 185 (2 Sept. 1969), pp. 847–853. DOI: 10.1103/PhysRev.185.847. URL: https://link.aps.org/doi/10.1103/PhysRev.185.847.

[42] B. Coqblin and G. Toulouse. "Effet des corrélations entre électrons sur les propriétes des alliages dilués: Un traitement variationnel". In: *Journal of Physics and Chemistry of Solids* 29.3 (1968), pp. 463–474. ISSN: 0022-3697. DOI: https://doi.org/10.1016/0022-3697(68)90123-6. URL: https://www.sciencedirect.com/science/article/pii/0022369768901236.

[43] J. Custers et al. “The break-up of heavy electrons at a quantum critical point”. In: *Nature* 424.6948 (July 2003), pp. 524–527. ISSN: 1476-4687. DOI: `10.1038/nature01774`. URL: `https://doi.org/10.1038/nature01774`.

[44] Peter Czajka et al. “Oscillations of the thermal conductivity in the spin-liquid state of α-RuCl 3”. In: *Nature Physics* (2021), pp. 1–5.

[45] S Doniach. “The Kondo lattice and weak antiferromagnetism”. In: *Physica B+C* 91 (1977), pp. 231–234. URL: `https://www.sciencedirect.com/science/article/abs/pii/0378436377901905`.

[46] F. Ducastelle. “Electronic structure of vacancy resonant states in graphene: A critical review of the single-vacancy case”. In: *Phys. Rev. B* 88 (7 Aug. 2013), p. 075413. DOI: `10.1103/PhysRevB.88.075413`. URL: `https://link.aps.org/doi/10.1103/PhysRevB.88.075413`.

[47] Ilya Esterlis and Jörg Schmalian. “Cooper pairing of incoherent electrons: An electron-phonon version of the Sachdev-Ye-Kitaev model”. In: *Phys. Rev. B* 100 (11 Sept. 2019), p. 115132. DOI: `10.1103/PhysRevB.100.115132`. URL: `https://link.aps.org/doi/10.1103/PhysRevB.100.115132`.

[48] Eduardo Fradkin and Stephen H. Shenker. “Phase diagrams of lattice gauge theories with Higgs fields”. In: *Phys. Rev. D* 19 (12 June 1979), pp. 3682–3697. DOI: `10.1103/PhysRevD.19.3682`. URL: `https://link.aps.org/doi/10.1103/PhysRevD.19.3682`.

[49] Klaus Fredenhagen and Mihail Marcu. “Charged states in Z2 gauge theories”. In: *Communications in Mathematical Physics* 92.1 (Mar. 1983), pp. 81–119. ISSN: 1432-0916. DOI: `10.1007/BF01206315`. URL: `https://doi.org/10.1007/BF01206315`.

[50] J. Friedel. “XIV. The distribution of electrons round impurities in monovalent metals”. In: *The London, Edinburgh, and Dublin Philosophical Magazine and Journal of Science* 43.337 (1952), pp. 153–189. DOI: `10.1080/14786440208561086`. eprint: `https://doi.org/10.1080/14786440208561086`. URL: `https://doi.org/10.1080/14786440208561086`.

[51] Sven Friedemann et al. “Fermi-surface collapse and dynamical scaling near a quantum-critical point”. In: *Proceedings of the National Academy of Sciences* 107.33 (2010), pp. 14547–14551. URL: `https://www.pnas.org/content/107/33/14547`.

[52] Wen Xiao Gang. *Quantum Field Theory of Many-Body Systems: From the Origin of Sound to an Origin of Light and Electrons*. Oxford University Press, 2007. DOI: `10.1093/acprof:oso/9780199227259.001.0001`. URL: `https://oxford.universitypressscholarship.com/view/10.1093/acprof:oso/9780199227259.001.0001/acprof-9780199227259`.

[53] Antoine Georges and Jernej Mravlje. “Skewed non-Fermi liquids and the Seebeck effect”. In: *Phys. Rev. Res.* 3 (4 Nov. 2021), p. 043132. DOI: `10.1103/PhysRevResearch.3.043132`. URL: `https://link.aps.org/doi/10.1103/PhysRevResearch.3.043132`.

[54] Ph. de Sousa Gerbert. “Fermions in an Aharonov-Bohm field and cosmic strings”. In: *Phys. Rev. D* 40 (4 Aug. 1989), pp. 1346–1349. DOI: `10.1103/PhysRevD.40.1346`. URL: `https://link.aps.org/doi/10.1103/PhysRevD.40.1346`.

[55] Bhaskar Ghawri et al. “Excess entropy and breakdown of semiclassical description of thermoelectricity in twisted bilayer graphene close to half filling”. In: *arXiv e-prints*, arXiv:2004.12356 (Apr. 2020), arXiv:2004.12356. arXiv: `2004.12356 [cond-mat.mes-hall]`.

[56] Gábor B. Halász, J. T. Chalker, and R. Moessner. “Doping a topological quantum spin liquid: Slow holes in the Kitaev honeycomb model”. In: *Phys. Rev. B* 90 (3 July 2014), p. 035145. DOI: `10.1103/PhysRevB.90.035145`. URL: `https://link.aps.org/doi/10.1103/PhysRevB.90.035145`.

[57] F. D. M. Haldane. “Model for a Quantum Hall Effect without Landau Levels: Condensed-Matter Realization of the ”Parity Anomaly””. In: *Phys. Rev. Lett.* 61 (18 Oct. 1988), pp. 2015–2018. DOI: `10.1103/PhysRevLett.61.2015`. URL: `https://link.aps.org/doi/10.1103/PhysRevLett.61.2015`.

[58] B. I. Halperin, Patrick A. Lee, and Nicholas Read. “Theory of the half-filled Landau level”. In: *Phys. Rev. B* 47 (12 Mar. 1993), pp. 7312–7343. DOI: `10.1103/PhysRevB.47.7312`. URL: `https://link.aps.org/doi/10.1103/PhysRevB.47.7312`.

[59] Sean A Hartnoll, Andrew Lucas, and Subir Sachdev. *Holographic quantum matter*. MIT press, 2018. URL: `https://mitpress.mit.edu/books/holographic-quantum-matter`.

[60] Sean A. Hartnoll and Andrew P. Mackenzie. “Colloquium: Planckian dissipation in metals”. In: *Rev. Mod. Phys.* 94 (4 Nov. 2022), p. 041002. DOI: `10.1103/RevModPhys.94.041002`. URL: `https://link.aps.org/doi/10.1103/RevModPhys.94.041002`.

[61] Alexander Cyril Hewson. “Models of Magnetic Impurities”. In: *The Kondo Problem to Heavy Fermions*. Cambridge Studies in Magnetism. Cambridge University Press, 1993, pp. 1–28. DOI: `10.1017/CBO9780511470752.004`.

[62] T. Holstein and H. Primakoff. “Field Dependence of the Intrinsic Domain Magnetization of a Ferromagnet”. In: *Physical Review* 58.12 (1940), pp. 1098–1113. DOI: `10.1103/physrev.58.1098`.

[63] N. M. Hugenholtz and D. Pines. “Ground-state energy and excitation spectrum of a system of interacting bosons”. In: *Phys. Rev.* 116 (3 Nov. 1959), pp. 489–506. DOI: `10.1103/PhysRev.116.489`. URL: `https://link.aps.org/doi/10.1103/PhysRev.116.489`.

[64] L. B. Ioffe and A. I. Larkin. “Gapless fermions and gauge fields in dielectrics”. In: *Phys. Rev. B* 39 (13 May 1989), pp. 8988–8999. DOI: `10.1103/PhysRevB.39.8988`. URL: `https://link.aps.org/doi/10.1103/PhysRevB.39.8988`.

[65] G. Jackeli and G. Khaliullin. “Mott Insulators in the Strong Spin-Orbit Coupling Limit: From Heisenberg to a Quantum Compass and Kitaev Models”. In: *Phys. Rev. Lett.* 102 (1 Jan. 2009), p. 017205. DOI: 10.1103/PhysRevLett.102.017205. URL: https://link.aps.org/doi/10.1103/PhysRevLett.102.017205.

[66] R. Jackiw and J.R. Schrieffer. “Solitons with fermion number 1/2 in condensed matter and relativistic field theories”. In: *Nuclear Physics B* 190.2 (1981), pp. 253–265. ISSN: 0550-3213. DOI: https://doi.org/10.1016/0550-3213(81)90557-5. URL: https://www.sciencedirect.com/science/article/pii/0550321381905575.

[67] Th. Jolicoeur and J. C. Le Guillou. “Spin-wave results for the triangular Heisenberg antiferromagnet”. In: *Phys. Rev. B* 40 (4 Aug. 1989), pp. 2727–2729. DOI: 10.1103/PhysRevB.40.2727. URL: https://link.aps.org/doi/10.1103/PhysRevB.40.2727.

[68] K. Kadowaki and S.B. Woods. “Universal relationship of the resistivity and specific heat in heavy-Fermion compounds”. In: *Solid State Communications* 58.8 (1986), pp. 507–509. ISSN: 0038-1098. DOI: https://doi.org/10.1016/0038-1098(86)90785-4. URL: https://www.sciencedirect.com/science/article/pii/0038109886907854.

[69] Marcin Kalinowski, Nishad Maskara, and Mikhail D. Lukin. “Non-Abelian Floquet Spin Liquids in a Digital Rydberg Simulator”. In: *Phys. Rev. X* 13 (3 July 2023), p. 031008. DOI: 10.1103/PhysRevX.13.031008. URL: https://link.aps.org/doi/10.1103/PhysRevX.13.031008.

[70] Wen-Han Kao et al. “Vacancy-Induced Low-Energy Density of States in the Kitaev Spin Liquid”. In: *Phys. Rev. X* 11 (1 Feb. 2021), p. 011034. DOI: 10.1103/PhysRevX.11.011034. URL: https://link.aps.org/doi/10.1103/PhysRevX.11.011034.

[71] Y. Kasahara et al. “Majorana quantization and half-integer thermal quantum Hall effect in a Kitaev spin liquid”. In: *Nature* 559.7713 (July 2018), pp. 227–231. ISSN: 1476-4687. DOI: 10.1038/s41586-018-0274-0. URL: https://doi.org/10.1038/s41586-018-0274-0.

[72] Y. Kasahara et al. “Unusual Thermal Hall Effect in a Kitaev Spin Liquid Candidate $\alpha-\mathrm{RuCl}_3$”. In: *Phys. Rev. Lett.* 120 (21 May 2018), p. 217205. DOI: 10.1103/PhysRevLett.120.217205. URL: https://link.aps.org/doi/10.1103/PhysRevLett.120.217205.

[73] Tadao Kasuya. “A Theory of Metallic Ferro- and Antiferromagnetism on Zener’s Model”. In: *Progress of Theoretical Physics* 16.1 (July 1956), pp. 45–57. ISSN: 0033-068X. DOI: 10.1143/PTP.16.45. eprint: https://academic.oup.com/ptp/article-pdf/16/1/45/5266722/16-1-45.pdf. URL: https://doi.org/10.1143/PTP.16.45.

[74] Jaewon Kim, Ehud Altman, and Xiangyu Cao. “Dirac fast scramblers”. In: *Phys. Rev. B* 103 (8 Feb. 2021), p. L081113. DOI: 10.1103/PhysRevB.103.L081113. URL: https://link.aps.org/doi/10.1103/PhysRevB.103.L081113.

[75] Jaewon Kim, Xiangyu Cao, and Ehud Altman. "Low-rank Sachdev-Ye-Kitaev models". In: *Phys. Rev. B* 101 (12 Mar. 2020), p. 125112. DOI: `10.1103/PhysRevB.101.125112`. URL: `https://link.aps.org/doi/10.1103/PhysRevB.101.125112`.

[76] Yong Baek Kim et al. "Gauge-invariant response functions of fermions coupled to a gauge field". In: *Phys. Rev. B* 50 (24 Dec. 1994), pp. 17917–17932. DOI: `10.1103/PhysRevB.50.17917`. URL: `https://link.aps.org/doi/10.1103/PhysRevB.50.17917`.

[77] A.Yu. Kitaev. "Fault-tolerant quantum computation by anyons". In: *Annals of Physics* 303.1 (2003), pp. 2–30. ISSN: 0003-4916. DOI: `https://doi.org/10.1016/S0003-4916(02)00018-0`. URL: `https://www.sciencedirect.com/science/article/pii/S0003491602000180`.

[78] Alexei Kitaev. "Anyons in an exactly solved model and beyond". In: *Annals of Physics* 321.1 (2006). January Special Issue, pp. 2–111. ISSN: 0003-4916. DOI: `https://doi.org/10.1016/j.aop.2005.10.005`. URL: `https://www.sciencedirect.com/science/article/pii/S0003491605002381`.

[79] Alexei Kitaev and John Preskill. "Topological Entanglement Entropy". In: *Phys. Rev. Lett.* 96 (11 Mar. 2006), p. 110404. DOI: `10.1103/PhysRevLett.96.110404`. URL: `https://link.aps.org/doi/10.1103/PhysRevLett.96.110404`.

[80] Steven A. Kivelson, Daniel S. Rokhsar, and James P. Sethna. "Topology of the resonating valence-bond state: Solitons and high-T_c superconductivity". In: *Phys. Rev. B* 35 (16 June 1987), pp. 8865–8868. DOI: `10.1103/PhysRevB.35.8865`. URL: `https://link.aps.org/doi/10.1103/PhysRevB.35.8865`.

[81] Johannes Knolle et al. "Dynamics of a two-dimensional quantum spin liquid: signatures of emergent Majorana fermions and fluxes". In: *Physical Review Letters* 112.20 (2014), p. 207203.

[82] Jun Kondo. "g-Shift and Anomalous Hall Effect in Gadolinium Metals". In: *Progress of Theoretical Physics* 28.5 (Nov. 1962), pp. 846–856. ISSN: 0033-068X. DOI: `10.1143/PTP.28.846`. eprint: `https://academic.oup.com/ptp/article-pdf/28/5/846/5258393/28-5-846.pdf`. URL: `https://doi.org/10.1143/PTP.28.846`.

[83] L. D. Landau. "The Theory of a Fermi Liquid". In: *Zh. Eksp. Teor. Fiz.* 30.6 (1956), p. 1058.

[84] R. B. Laughlin. "Anomalous Quantum Hall Effect: An Incompressible Quantum Fluid with Fractionally Charged Excitations". In: *Phys. Rev. Lett.* 50 (18 May 1983), pp. 1395–1398. DOI: `10.1103/PhysRevLett.50.1395`. URL: `https://link.aps.org/doi/10.1103/PhysRevLett.50.1395`.

[85] R. B. Laughlin. "Quantized Hall conductivity in two dimensions". In: *Phys. Rev. B* 23 (10 May 1981), pp. 5632–5633. DOI: `10.1103/PhysRevB.23.5632`. URL: `https://link.aps.org/doi/10.1103/PhysRevB.23.5632`.

[86] Ian A Leahy et al. "Anomalous Thermal Conductivity and Magnetic Torque Response in the Honeycomb Magnet α- RuCl 3". In: *Physical Review Letters* 118.18 (2017), p. 187203.

[87] Patrick A. Lee and Naoto Nagaosa. "Gauge theory of the normal state of high-T_c superconductors". In: *Phys. Rev. B* 46 (9 Sept. 1992), pp. 5621–5639. DOI: 10.1103/PhysRevB.46.5621. URL: https://link.aps.org/doi/10.1103/PhysRevB.46.5621.

[88] Sung-Sik Lee. "Low-energy effective theory of Fermi surface coupled with U(1) gauge field in $2 + 1$ dimensions". In: *Phys. Rev. B* 80 (16 Oct. 2009), p. 165102. DOI: 10.1103/PhysRevB.80.165102. URL: https://link.aps.org/doi/10.1103/PhysRevB.80.165102.

[89] A. Legros et al. "Universal T-linear resistivity and Planckian dissipation in overdoped cuprates". In: *Nature Physics* 15.2 (Nov. 2018), pp. 142–147. DOI: 10.1038/s41567-018-0334-2. arXiv: 1805.02512 [cond-mat.supr-con].

[90] Elliott H. Lieb. "Flux Phase of the Half-Filled Band". In: *Physical Review Letters* 73.16 (Oct. 1994), pp. 2158–2161. ISSN: 0031-9007. DOI: 10.1103/physrevlett.73.2158. URL: http://dx.doi.org/10.1103/PhysRevLett.73.2158.

[91] Elliott H. Lieb and Michael Loss. "Fluxes, Laplacians, and Kasteleyn's theorem". In: *Duke Mathematical Journal* 71.2 (1993), pp. 337–363. DOI: 10.1215/S0012-7094-93-07114-1. URL: https://doi.org/10.1215/S0012-7094-93-07114-1.

[92] I M Lifshitz. "Energy Spectrum Structure and Quantum States of Disordered Condensed Systems". In: *Soviet Physics Uspekhi* 7.4 (Apr. 1965), pp. 549–573. DOI: 10.1070/pu1965v007n04abeh003634. URL: https://doi.org/10.1070/pu1965v007n04abeh003634.

[93] De-Hone Lin. "Levinson theorem with the nonlocal Aharonov-Bohm effect". In: *Phys. Rev. A* 68 (5 Nov. 2003), p. 052705. DOI: 10.1103/PhysRevA.68.052705. URL: https://link.aps.org/doi/10.1103/PhysRevA.68.052705.

[94] A. Little et al. "Antiferromagnetic Resonance and Terahertz Continuum in $\alpha-\mathrm{RuCl}_3$". In: *Phys. Rev. Lett.* 119 (22 Nov. 2017), p. 227201. DOI: 10.1103/PhysRevLett.119.227201. URL: https://link.aps.org/doi/10.1103/PhysRevLett.119.227201.

[95] X Liu et al. "Long-range magnetic ordering in Na 2 IrO 3". In: *Physical Review B* 83.22 (2011), p. 220403.

[96] J. M. Luttinger. "Fermi Surface and Some Simple Equilibrium Properties of a System of Interacting Fermions". In: *Phys. Rev.* 119 (4 Aug. 1960), pp. 1153–1163. DOI: 10.1103/PhysRev.119.1153. URL: https://link.aps.org/doi/10.1103/PhysRev.119.1153.

[97] Gerald D Mahan. *Many-particle physics*. Springer Science & Business Media, 2013. URL: https://www.springer.com/gp/book/9780306434235.

[98] Nikola Maksimovic et al. "Evidence for a delocalization quantum phase transition without symmetry breaking in CeCoIn5". In: *Science* 375.6576 (2022), pp. 76–81.

[99] Juan Maldacena and Douglas Stanford. "Remarks on the Sachdev-Ye-Kitaev model". In: *Phys. Rev. D* 94 (10 Nov. 2016), p. 106002. DOI: `10.1103/PhysRevD.94.106002`. URL: `https://link.aps.org/doi/10.1103/PhysRevD.94.106002`.

[100] Eric Marcus and Stefan Vandoren. "A new class of SYK-like models with maximal chaos". In: *Journal of High Energy Physics* 2019.1 (Jan. 2019), p. 166. ISSN: 1029-8479. DOI: `10.1007/JHEP01(2019)166`. URL: `https://doi.org/10.1007/JHEP01(2019)166`.

[101] Max A. Metlitski and Subir Sachdev. "Quantum phase transitions of metals in two spatial dimensions. I. Ising-nematic order". In: *Phys. Rev. B* 82 (7 Aug. 2010), p. 075127. DOI: `10.1103/PhysRevB.82.075127`. URL: `https://link.aps.org/doi/10.1103/PhysRevB.82.075127`.

[102] R. Moessner and S. L. Sondhi. "Resonating Valence Bond Phase in the Triangular Lattice Quantum Dimer Model". In: *Phys. Rev. Lett.* 86 (9 Feb. 2001), pp. 1881–1884. DOI: `10.1103/PhysRevLett.86.1881`. URL: `https://link.aps.org/doi/10.1103/PhysRevLett.86.1881`.

[103] Alexander Moroz. "Single-particle density of states, bound states, phase-shift flip, and a resonance in the presence of an Aharonov-Bohm potential". In: *Phys. Rev. A* 53 (2 Feb. 1996), pp. 669–694. DOI: `10.1103/PhysRevA.53.669`. URL: `https://link.aps.org/doi/10.1103/PhysRevA.53.669`.

[104] Y. Nakajima et al. "Planckian dissipation and scale invariance in a quantum-critical disordered pnictide". In: *arXiv e-prints* (Feb. 2019). arXiv: `1902.01034 [cond-mat.str-el]`.

[105] J. Nakamura et al. "Direct observation of anyonic braiding statistics". In: *Nature Physics* 16.9 (Sept. 2020), pp. 931–936. ISSN: 1745-2481. DOI: `10.1038/s41567-020-1019-1`. URL: `https://doi.org/10.1038/s41567-020-1019-1`.

[106] Chetan Nayak et al. "Non-Abelian anyons and topological quantum computation". In: *Rev. Mod. Phys.* 80 (3 Sept. 2008), pp. 1083–1159. DOI: `10.1103/RevModPhys.80.1083`. URL: `https://link.aps.org/doi/10.1103/RevModPhys.80.1083`.

[107] P. Nozières. "A "fermi-liquid" description of the Kondo problem at low temperatures". In: *Journal of Low Temperature Physics* 17.1 (Oct. 1974), pp. 31–42. ISSN: 1573-7357. DOI: `10.1007/BF00654541`. URL: `https://doi.org/10.1007/BF00654541`.

[108] Masaki Oshikawa. "Topological approach to Luttingerś theorem and the Fermi surface of a Kondo lattice". In: *Physical Review Letters* 84.15 (2000), p. 3370. URL: `https://journals.aps.org/prl/abstract/10.1103/PhysRevLett.84.3370`.

[109] Silke Paschen et al. "Hall-effect evolution across a heavy-fermion quantum critical point". In: *Nature* 432.7019 (2004), pp. 881–885. URL: `https://www.nature.com/articles/nature03129`.

[110] Aavishkar A. Patel, Michael J. Lawler, and Eun-Ah Kim. "Coherent superconductivity with a large gap ratio from incoherent metals". In: *Phys. Rev. Lett.* 121 (18 Oct. 2018), p. 187001. DOI: `10.1103/PhysRevLett.121.187001`. URL: `https://link.aps.org/doi/10.1103/PhysRevLett.121.187001`.

[111] Aavishkar A. Patel and Subir Sachdev. "Critical strange metal from fluctuating gauge fields in a solvable random model". In: *Phys. Rev. B* 98 (12 Sept. 2018), p. 125134. DOI: `10.1103/PhysRevB.98.125134`. URL: `https://link.aps.org/doi/10.1103/PhysRevB.98.125134`.

[112] Aavishkar A. Patel and Subir Sachdev. "DC resistivity at the onset of spin density wave order in two-dimensional metals". In: *Phys. Rev. B* 90 (16 Oct. 2014), p. 165146. DOI: `10.1103/PhysRevB.90.165146`. URL: `https://link.aps.org/doi/10.1103/PhysRevB.90.165146`.

[113] Aavishkar A. Patel and Subir Sachdev. "Theory of a Planckian metal". In: *Phys. Rev. Lett.* 123 (6 Aug. 2019), p. 066601. DOI: `10.1103/PhysRevLett.123.066601`. URL: `https://link.aps.org/doi/10.1103/PhysRevLett.123.066601`.

[114] Aavishkar A. Patel et al. "Magnetotransport in a model of a disordered strange metal". In: *Phys. Rev. X* 8 (2 May 2018), p. 021049. DOI: `10.1103/PhysRevX.8.021049`. URL: `https://link.aps.org/doi/10.1103/PhysRevX.8.021049`.

[115] I. Paul, C. Pépin, and M. R. Norman. "Equivalence of single-particle and transport Lifetimes from hybridization fluctuations". In: *Phys. Rev. Lett.* 110 (6 Feb. 2013), p. 066402. DOI: `10.1103/PhysRevLett.110.066402`. URL: `https://link.aps.org/doi/10.1103/PhysRevLett.110.066402`.

[116] I. Paul, C. Pépin, and M. R. Norman. "Kondo Breakdown and Hybridization Fluctuations in the Kondo-Heisenberg Lattice". In: *Phys. Rev. Lett.* 98 (2 Jan. 2007), p. 026402. DOI: `10.1103/PhysRevLett.98.026402`. URL: `https://link.aps.org/doi/10.1103/PhysRevLett.98.026402`.

[117] I. Paul, C. Pépin, and M. R. Norman. "Multiscale fluctuations near a Kondo breakdown quantum critical point". In: *Phys. Rev. B* 78 (3 July 2008), p. 035109. DOI: `10.1103/PhysRevB.78.035109`. URL: `https://link.aps.org/doi/10.1103/PhysRevB.78.035109`.

[118] Linus Pauling. "A Theory of Ferromagnetism". In: *Proceedings of the National Academy of Sciences* 39.6 (1953), pp. 551–560. DOI: `10.1073/pnas.39.6.551`. eprint: `https://www.pnas.org/doi/pdf/10.1073/pnas.39.6.551`. URL: `https://www.pnas.org/doi/abs/10.1073/pnas.39.6.551`.

[119] Vitor M. Pereira et al. "Disorder Induced Localized States in Graphene". In: *Phys. Rev. Lett.* 96 (3 Jan. 2006), p. 036801. DOI: `10.1103/PhysRevLett.96.036801`. URL: `https://link.aps.org/doi/10.1103/PhysRevLett.96.036801`.

[120] R de-Picciotto et al. “Direct observation of a fractional charge”. In: *Physica B: Condensed Matter* 249-251 (1998), pp. 395–400. ISSN: 0921-4526. DOI: `https://doi.org/10.1016/S0921-4526(98)00139-2`. URL: `https://www.sciencedirect.com/science/article/pii/S0921452698001392`.

[121] AN Ponomaryov et al. “Unconventional spin dynamics in the honeycomb-lattice material α- RuCl 3: High-field electron spin resonance studies”. In: *Physical Review B* 96.24 (2017), p. 241107.

[122] Cyril Proust and Louis Taillefer. “The remarkable underlying ground states of cuprate superconductors”. In: *Annual Review of Condensed Matter Physics* 10.1 (2019), pp. 409–429. DOI: `10.1146/annurev-conmatphys-031218-013210`. eprint: `https://doi.org/10.1146/annurev-conmatphys-031218-013210`. URL: `https://doi.org/10.1146/annurev-conmatphys-031218-013210`.

[123] Kejing Ran et al. “Spin-Wave Excitations Evidencing the Kitaev Interaction in Single Crystalline α- RuCl 3”. In: *Physical Review Letters* 118.10 (2017), p. 107203.

[124] Jeffrey G. Rau, Eric Kin-Ho Lee, and Hae-Young Kee. “Generic Spin Model for the Honeycomb Iridates beyond the Kitaev Limit”. In: *Phys. Rev. Lett.* 112 (7 Feb. 2014), p. 077204. DOI: `10.1103/PhysRevLett.112.077204`. URL: `https://link.aps.org/doi/10.1103/PhysRevLett.112.077204`.

[125] Nicholas Read and DM Newns. “On the solution of the Coqblin-Schreiffer Hamiltonian by the large-N expansion technique”. In: *Journal of Physics C: Solid State Physics* 16.17 (1983), p. 3273. URL: `https://iopscience.iop.org/article/10.1088/0022-3719/16/17/014`.

[126] R. Rohm. PhD thesis. Princeton University, 1985.

[127] A Roy and M Stone. “Fullerenes, zero-modes and self-adjoint extensions”. In: *Journal of Physics A: Mathematical and Theoretical* 43.1 (Dec. 2009), p. 015203. DOI: `10.1088/1751-8113/43/1/015203`. URL: `https://doi.org/10.1088/1751-8113/43/1/015203`.

[128] M. A. Ruderman and C. Kittel. “Indirect Exchange Coupling of Nuclear Magnetic Moments by Conduction Electrons”. In: *Phys. Rev.* 96 (1 Oct. 1954), pp. 99–102. DOI: `10.1103/PhysRev.96.99`. URL: `https://link.aps.org/doi/10.1103/PhysRev.96.99`.

[129] S.N.M Ruijsenaars. “The Aharonov-Bohm effect and scattering theory”. In: *Annals of Physics* 146.1 (1983), pp. 1–34. ISSN: 0003-4916. DOI: `https://doi.org/10.1016/0003-4916(83)90051-9`. URL: `https://www.sciencedirect.com/science/article/pii/0003491683900519`.

[130] Subir Sachdev. *Quantum Phase Transitions*. 2nd ed. Cambridge University Press, 2011. DOI: `10.1017/CBO9780511973765`.

[131] Subir Sachdev. *Quantum phase transitions*. Cambridge University Press, 2011. URL: https://www.cambridge.org/core/books/quantum-phase-transitions/33C1C81500346005E54C1DE4223E5562.

[132] Subir Sachdev. *Quantum Phases of Matter*. Cambridge University Press, 2023. DOI: 10.1017/9781009212717.

[133] Luke J Sandilands et al. "Scattering Continuum and Possible Fractionalized Excitations in α- RuCl 3". In: *Physical review letters* 114.14 (2015), p. 147201.

[134] J. R. Schrieffer and P. A. Wolff. "Relation between the Anderson and Kondo Hamiltonians". In: *Phys. Rev.* 149 (2 Sept. 1966), pp. 491–492. DOI: 10.1103/PhysRev.149.491. URL: https://link.aps.org/doi/10.1103/PhysRev.149.491.

[135] JA Sears et al. "Magnetic order in α- RuCl 3: A honeycomb-lattice quantum magnet with strong spin-orbit coupling". In: *Physical Review B* 91.14 (2015), p. 144420.

[136] JA Sears et al. "Phase diagram of α- RuCl 3 in an in-plane magnetic field". In: *Physical Review B* 95.18 (2017), p. 180411.

[137] G. Semeghini et al. "Probing topological spin liquids on a programmable quantum simulator". In: *Science* 374.6572 (2021), pp. 1242–1247. DOI: 10.1126/science.abi8794. eprint: https://www.science.org/doi/pdf/10.1126/science.abi8794. URL: https://www.science.org/doi/abs/10.1126/science.abi8794.

[138] T Senthil, Subir Sachdev, and Matthias Vojta. "Fractionalized Fermi liquids". In: *Physical review letters* 90.21 (2003), p. 216403. URL: https://journals.aps.org/prl/abstract/10.1103/PhysRevLett.90.216403.

[139] T Senthil, Matthias Vojta, and Subir Sachdev. "Weak magnetism and non-Fermi liquids near heavy-fermion critical points". In: *Physical Review B* 69.3 (2004), p. 035111. URL: https://journals.aps.org/prb/abstract/10.1103/PhysRevB.69.035111.

[140] L. Y. Shi et al. "Field-induced magnon excitation and in-gap absorption in the Kitaev candidate RuCl_3". In: *Phys. Rev. B* 98 (9 Sept. 2018), p. 094414. DOI: 10.1103/PhysRevB.98.094414. URL: https://link.aps.org/doi/10.1103/PhysRevB.98.094414.

[141] Hideki Shirakawa, Takeo Ito, and Sakuji Ikeda. "Electrical properties of polyacetylene with various cis-trans compositions". In: *Die Makromolekulare Chemie* 179.6 (1978), pp. 1565–1573. DOI: https://doi.org/10.1002/macp.1978.021790615. eprint: https://onlinelibrary.wiley.com/doi/pdf/10.1002/macp.1978.021790615. URL: https://onlinelibrary.wiley.com/doi/abs/10.1002/macp.1978.021790615.

[142] Hideki Shirakawa et al. "Synthesis of electrically conducting organic polymers: halogen derivatives of polyacetylene, (CH)". In: *J. Chem. Soc., Chem. Commun.* (16 1977), pp. 578–580. DOI: 10.1039/C39770000578. URL: http://dx.doi.org/10.1039/C39770000578.

[143] Hiroaki Shishido et al. "A drastic change of the Fermi surface at a critical pressure in $CeRhIn_5$: dHvA study under pressure". In: *Journal of the Physical Society of Japan* 74.4 (2005), pp. 1103–1106. URL: https://journals.jps.jp/doi/10.1143/JPSJ.74.1103.

[144] Qimiao Si and Frank Steglich. "Heavy fermions and quantum phase transitions". In: *Science* 329.5996 (2010), pp. 1161–1166. URL: https://science.sciencemag.org/content/329/5996/1161.

[145] Ady Stern. "Anyons and the quantum Hall effect—A pedagogical review". In: *Annals of Physics* 323.1 (2008). January Special Issue 2008, pp. 204–249. ISSN: 0003-4916. DOI: https://doi.org/10.1016/j.aop.2007.10.008. URL: https://www.sciencedirect.com/science/article/pii/S0003491607001674.

[146] G. R. Stewart. "Non-Fermi-liquid behavior in d- and f-electron metals". In: *Rev. Mod. Phys.* 73 (4 Oct. 2001), pp. 797–855. DOI: 10.1103/RevModPhys.73.797. URL: https://link.aps.org/doi/10.1103/RevModPhys.73.797.

[147] W. P. Su, J. R. Schrieffer, and A. J. Heeger. "Soliton excitations in polyacetylene". In: *Phys. Rev. B* 22 (4 Aug. 1980), pp. 2099–2111. DOI: 10.1103/PhysRevB.22.2099. URL: https://link.aps.org/doi/10.1103/PhysRevB.22.2099.

[148] Takafumi Suzuki and Sei-ichiro Suga. "Effective model with strong Kitaev interactions for $\alpha{-}RuCl_3$". In: *Phys. Rev. B* 97 (13 Apr. 2018), p. 134424. DOI: 10.1103/PhysRevB.97.134424. URL: https://link.aps.org/doi/10.1103/PhysRevB.97.134424.

[149] Louis Taillefer. "Scattering and Pairing in cuprate Superconductors". In: *Annual Review of Condensed Matter Physics* 1.1 (2010), pp. 51–70. DOI: 10.1146/annurev-conmatphys-070909-104117. eprint: https://doi.org/10.1146/annurev-conmatphys-070909-104117. URL: https://doi.org/10.1146/annurev-conmatphys-070909-104117.

[150] H Takagi et al. "Systematic evolution of temperature-dependent resistivity in La 2- x Sr x CuO 4". In: *Physical review letters* 69.20 (1992), p. 2975.

[151] Tomohiro Takayama et al. "Hyperhoneycomb Iridate β- Li 2 IrO 3 as a Platform for Kitaev Magnetism". In: *Physical review letters* 114.7 (2015), p. 077202.

[152] Mathieu Taupin and Silke Paschen. "Are Heavy Fermion Strange Metals Planckian?" In: *Crystals* 12.2 (2022). ISSN: 2073-4352. DOI: 10.3390/cryst12020251. URL: https://www.mdpi.com/2073-4352/12/2/251.

[153] S Toth and B Lake. "Linear spin wave theory for single-Q incommensurate magnetic structures". In: *Journal of Physics: Condensed Matter* 27.16 (2015), p. 166002. DOI: 10.1088/0953-8984/27/16/166002.

[154] D. C. Tsui, H. L. Stormer, and A. C. Gossard. "Two-Dimensional Magnetotransport in the Extreme Quantum Limit". In: *Phys. Rev. Lett.* 48 (22 May 1982), pp. 1559–1562. DOI: 10.1103/PhysRevLett.48.1559. URL: https://link.aps.org/doi/10.1103/PhysRevLett.48.1559.

[155] C. M. Varma et al. “Phenomenology of the normal state of Cu-O high-temperature superconductors”. In: *Phys. Rev. Lett.* 63 (18 Oct. 1989), pp. 1996–1999. DOI: 10.1103/PhysRevLett.63.1996. URL: https://link.aps.org/doi/10.1103/PhysRevLett.63.1996.

[156] Wei Wang et al. “Theoretical investigation of magnetic dynamics in $\alpha - \mathrm{RuCl}_3$”. In: *Phys. Rev. B* 96 (11 Sept. 2017), p. 115103. DOI: 10.1103/PhysRevB.96.115103. URL: https://link.aps.org/doi/10.1103/PhysRevB.96.115103.

[157] Yuxuan Wang. “Solvable Strong-Coupling Quantum-Dot Model with a Non-Fermi-Liquid Pairing Transition”. In: *Phys. Rev. Lett.* 124 (1 Jan. 2020), p. 017002. DOI: 10.1103/PhysRevLett.124.017002. URL: https://link.aps.org/doi/10.1103/PhysRevLett.124.017002.

[158] Franz J. Wegner. “Duality in Generalized Ising Models and Phase Transitions without Local Order Parameters”. In: *Journal of Mathematical Physics* 12.10 (1971), pp. 2259–2272. DOI: 10.1063/1.1665530. eprint: https://doi.org/10.1063/1.1665530. URL: https://doi.org/10.1063/1.1665530.

[159] Zezhu Wei, V. F. Mitrovi ć, and D. E. Feldman. “Thermal Interferometry of Anyons in Spin Liquids”. In: *Phys. Rev. Lett.* 127 (16 Oct. 2021), p. 167204. DOI: 10.1103/PhysRevLett.127.167204. URL: https://link.aps.org/doi/10.1103/PhysRevLett.127.167204.

[160] X. G. Wen. “Mean-field theory of spin-liquid states with finite energy gap and topological orders”. In: *Phys. Rev. B* 44 (6 Aug. 1991), pp. 2664–2672. DOI: 10.1103/PhysRevB.44.2664. URL: https://link.aps.org/doi/10.1103/PhysRevB.44.2664.

[161] Xiao-Gang Wen. “Topological orders and Chern-Simons theory in strongly correlated quantum liquid”. In: *International Journal of Modern Physics B* 5.10 (1991), pp. 1641–1648.

[162] Frank Wilczek. “Quantum Mechanics of Fractional-Spin Particles”. In: *Phys. Rev. Lett.* 49 (14 Oct. 1982), pp. 957–959. DOI: 10.1103/PhysRevLett.49.957. URL: https://link.aps.org/doi/10.1103/PhysRevLett.49.957.

[163] A. J. Willans, J. T. Chalker, and R. Moessner. “Disorder in a Quantum Spin Liquid: Flux Binding and Local Moment Formation”. In: *Phys. Rev. Lett.* 104 (23 June 2010), p. 237203. DOI: 10.1103/PhysRevLett.104.237203. URL: https://link.aps.org/doi/10.1103/PhysRevLett.104.237203.

[164] A. J. Willans, J. T. Chalker, and R. Moessner. “Site dilution in the Kitaev honeycomb model”. In: *Phys. Rev. B* 84 (11 Sept. 2011), p. 115146. DOI: 10.1103/PhysRevB.84.115146. URL: https://link.aps.org/doi/10.1103/PhysRevB.84.115146.

[165] Kenneth G. Wilson. “The renormalization group: Critical phenomena and the Kondo problem”. In: *Rev. Mod. Phys.* 47 (4 Oct. 1975), pp. 773–840. DOI: 10.1103/RevModPhys.47.773. URL: https://link.aps.org/doi/10.1103/RevModPhys.47.773.

[166] Stephen M Winter et al. “Breakdown of magnons in a strongly spin-orbital coupled magnet”. In: *Nature Communications* 8.1 (2017), p. 1152.

[167] Stephen M Winter et al. “Challenges in design of Kitaev materials: Magnetic interactions from competing energy scales”. In: *Physical Review B* 93.21 (2016), p. 214431.

[168] Stephen M Winter et al. “Models and materials for generalized Kitaev magnetism”. In: *Journal of Physics: Condensed Matter* 29.49 (Nov. 2017), p. 493002. DOI: `10.1088/1361-648x/aa8cf5`. URL: `https://doi.org/10.1088/1361-648x/aa8cf5`.

[169] Stephen M Winter et al. “Probing α- RuCl 3 Beyond Magnetic Order: Effects of Temperature and Magnetic Field”. In: *Physical review letters* 120.7 (2018), p. 077203.

[170] Charles G Wohl. *How to be a Quantum Mechanic*. CRC Press, 2022.

[171] Liang Wu et al. “Field evolution of magnons in $\alpha-\mathrm{RuCl}_3$ by high-resolution polarized terahertz spectroscopy”. In: *Phys. Rev. B* 98 (9 Sept. 2018), p. 094425. DOI: `10.1103/PhysRevB.98.094425`. URL: `https://link.aps.org/doi/10.1103/PhysRevB.98.094425`.

[172] Liang Wu et al. “Field evolution of magnons in α- RuCl 3 by high-resolution polarized terahertz spectroscopy”. In: *Physical Review B* 98.9 (2018), p. 094425.

[173] Ravi Yadav et al. “Kitaev exchange and field-induced quantum spin-liquid states in honeycomb α-RuCl3”. In: *Scientific reports* 6 (2016), p. 37925.

[174] Hong Yao and Steven A. Kivelson. “Exact Chiral Spin Liquid with Non-Abelian Anyons”. In: *Phys. Rev. Lett.* 99 (24 Dec. 2007), p. 247203. DOI: `10.1103/PhysRevLett.99.247203`. URL: `https://link.aps.org/doi/10.1103/PhysRevLett.99.247203`.

[175] T Yokoi et al. “Half-integer quantized anomalous thermal Hall effect in the Kitaev material candidate α-RuCl3”. In: *Science* 373.6554 (2021), pp. 568–572.

[176] Kei Yosida. “Magnetic Properties of Cu-Mn Alloys”. In: *Phys. Rev.* 106 (5 June 1957), pp. 893–898. DOI: `10.1103/PhysRev.106.893`. URL: `https://link.aps.org/doi/10.1103/PhysRev.106.893`.

[177] Ya-Hui Zhang and Subir Sachdev. “From the pseudogap metal to the Fermi liquid using ancilla qubits”. In: *Phys. Rev. Research* 2 (2 May 2020), p. 023172. DOI: `10.1103/PhysRevResearch.2.023172`. URL: `https://link.aps.org/doi/10.1103/PhysRevResearch.2.023172`.

[178] Jiacheng Zheng et al. “Gapless Spin Excitations in the Field-Induced Quantum Spin Liquid Phase of alpha-RuCl3”. In: *arXiv preprint arXiv:1703.08474* (2017).

Appendix A

Toric Code Review

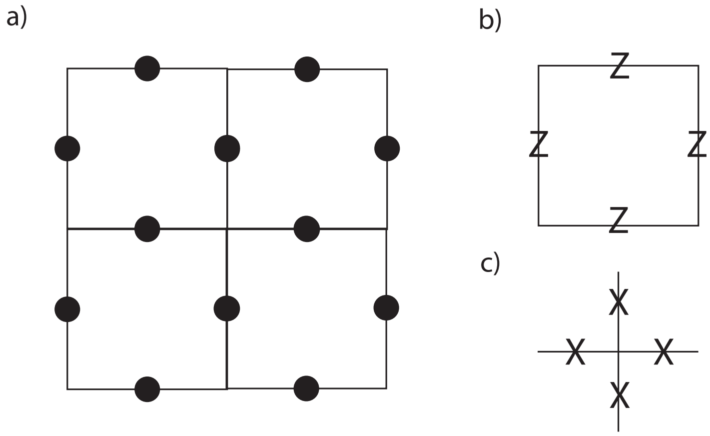

Figure A.1: (a) The square lattice with spins assigned to edges. (b) The plaquette operator B_p.(c) The vertex operator A_s.

The Toric code is an exactly soluble quantum spin liquid which exhibits topologically protected qubits [77]. In the Toric code spin operators fractionalize into two distinct bosons who anti-commute with each other under exchange. These bosons are the flux and charge excitations of an emergent Z_2 gauge field. The Toric code is defined by placing spin 1/2 moments on each of the square lattice as shown in Fig. A.1. The Hamiltonian is given by a sum over terms, one for each plaquette B_p and one for each vertex A_s also shown in Fig. A.1. The Hamiltonian is given by:

$$H = -K \sum_p B_p - K \sum_s A_s \quad B_p = \prod_{i \in p} Z_i \quad A_s = \prod_{i \in s} X_i. \tag{A.1}$$

All of the terms in this Hamiltonian commute because star and plaquette operators always overlap on zero or two spins. This implies that the ground state can be quickly found by maximizing the eigenvalues of all the operators. As $B_p^2 = A_s^2 = 1$ the only eigenvalues possible for both operators are ± 1, so the ground state is defined by $B_p|GS\rangle = A_s|GS\rangle = +|GS\rangle$. A direct approach to generating such a state is by projection:

$$|GS\rangle \propto \prod_s (\frac{1+A_s}{2})|+z\rangle^{\otimes N}. \tag{A.2}$$

As $[B_p, A_s] = 0$ and $B_p|+z\rangle^{\otimes N} = +|+z\rangle^{\otimes N}$ we see that this ansatz satisfies all plaquette conditions. The star operator in front serves to project out any component with eigenvalue (-1) with respect to the star operators. What is left therefore must be an unnormalized ground state.

In this ground state we find a local symmetry, $A_s|GS\rangle = B_p|GS\rangle = |GS\rangle$, for all plaquettes and stars. Amazingly, this spin model produces a ground state with an emergent Z_2 gauge symmetry.

Within this solvable model all excitations are easily described as violations of the plaquette or star terms which are called magnetic fluxes and electric charges respectively. Magnetic flux pairs are created by acting a string of X operators through the dual lattice and electric charges are created by acting a string of Z operators through the direct lattice. From this construction we can work out their mutual statistics by creating a well separated pair of electric charges and creating a pair of magnetic fluxes, propagating one around a single electric charge and then annihilating the magnetic flux. This process can be described by:

$$\prod_{i\in Cb} X_i \prod_{j\in L} Z_j|GS\rangle = \prod_{s\in C} A_s \prod_{j\in L} Z_j|GS\rangle = -\prod_{j\in L} Z_j|GS\rangle, \tag{A.3}$$

where here Cb refers to the boundary of the loop taken by the magnetic flux, L refers to the line that separates the electric charges and we have used the fact that for any closed loop Cb with interior C, $\prod_{i\in Cb} X_i = \prod_{s\in C} A_s$. What we have shown is that the electric charges and magnetic fluxes of the model acquire a phase of (-1) when one is braided around the other, a feature not shared with any higher dimensional model. A similar calculation will show that both are mutual bosons, in that they have trivial self-statistics. By similar considerations, we can consider the act of creating a pair of quasiparticles and propagating them around any non-trivial cycle of the surface on which the model is defined, before annihilating it on a partner. As these operators fail to commute we can choose an eigenbasis of only one for each cycle-for instance the charge transporting operator $\prod_{i\in\nu} Z_i$ for some cycle ν. By comparison with the plaquette flux operators we see that this operator measures the Z_2 magnetic flux through the cycle ν, it commutes with all terms in the Hamiltonian and therefore gives rise to a ground state degeneracy which depends on the surface it belongs to [77]. In the case of the torus, this topological order manifests as a degeneracy of four due to the two cycles each with two possible flux configurations.